

1 UNIVERSITY OF BRISTOL

2 DOCTORAL THESIS

3

4 **Investigating, implementing, and creating**
5 **methods for analysing large neuronal**
6 **ensembles**

7

8 *Author:*

Thomas J. DELANEY

Supervisors:

Dr. Cian O'DONNELL

Dr. Michael C. ASHBY

9 *A thesis submitted in fulfillment of the requirements*
10 *for the degree of Doctor of Philosophy*

11 *in the*

12 **Biological Intelligence & Machine Learning Unit**
13 **Department of Computer Science**

Declaration of Authorship

I, Thomas J. DELANEY, declare that this thesis titled, “Investigating, implementing, and creating methods for analysing large neuronal ensembles” and the work presented in it are my own. I confirm that:

- This work was done wholly or mainly while in candidature for a research degree at this University.
- Where any part of this thesis has previously been submitted for a degree or any other qualification at this University or any other institution, this has been clearly stated.
- Where I have consulted the published work of others, this is always clearly attributed.
- Where I have quoted from the work of others, the source is always given. With the exception of such quotations, this thesis is entirely my own work.
- I have acknowledged all main sources of help.
- Where the thesis is based on work done by myself jointly with others, I have made clear exactly what was done by others and what I have contributed myself.

Signed:

Date:

34

UNIVERSITY OF BRISTOL

35

Abstract

36

Engineering

37

Department of Computer Science

38

Doctor of Philosophy

39

Investigating, implementing, and creating methods for analysing large neuronal

40

ensembles

41

by Thomas J. DELANEY

42 The Thesis Abstract is written here (and usually kept to just this page). The page is kept

43 centered vertically so can expand into the blank space above the title too...

Acknowledgements

44

45 The acknowledgments and the people to thank go here, don't forget to include your project
46 advisor...

Contents

48	Declaration of Authorship	iii
49	Abstract	v
50	Acknowledgements	vii
51	1 Sensitivity of the spikes-to-fluorescence transform to calcium indicator and neu-	
52	ron properties	1
53	1.1 Introduction	4
54	1.2 Results	6
55	1.2.1 A biophysical computational model can generate accurate fluo-	
56	rescence traces from spike trains	6
57	1.2.2 Spike inference algorithms perform similarly on real data compared	
58	with time series simulated from the model	7
59	1.2.3 Relative effects of various buffers to the fluorescence signal	8
60	1.2.4 Spike inference accuracy is sensitive to indicator properties, and likely	
61	varies within and between cells	10
62	1.2.5 Single spike inference accuracy drops for high firing rates, but firing	
63	rate itself can be estimated from mean fluorescence amplitude	14
64	1.3 Discussion	16
65	1.4 Methods	18
66	1.4.1 Calcium dynamics model	18
67	Photon release & capture	21
68	1.4.2 Parameter optimisation	21
69	Fixed parameters	23
70	1.4.3 Julia	24
71	1.4.4 Spike inference	24
72	Comparing spike inference quality	26
73	1.4.5 Perturbation analysis	26

74	1.4.6	Signal-to-noise ratio	27
75	1.4.7	Data sources	27
76	2	Functional networks expand across anatomical boundaries as correlation time-	
77		scale increases	29
78	2.1	Introduction	32
79	2.2	Results	33
80	2.2.1	Average correlation size increases with increasing time bin width . .	33
81	2.2.2	Goodness-of-fit for Poisson and Gaussian distributions across increas-	
82		ing time bin widths	34
83	2.2.3	Differences between and inter- and intra- regional correlations de-	
84		crease with increasing bin width	36
85	2.2.4	Connected and divided structure in correlation based networks re-	
86		duces in dimension with increasing bin width	39
87	2.2.5	Detecting communities in correlation based networks	40
88	2.2.6	Functional communities resemble anatomical division at short timescales	40
89	2.2.7	Conditional correlations & signal correlations	44
90	2.2.8	Absolute correlations and negative rectified correlations	46
91	2.3	Discussion	48
92	2.4	Data	51
93	2.4.1	Brain regions	51
94	2.4.2	Video recordings	52
95	2.5	Methods	52
96	2.5.1	Binning data	52
97	2.5.2	Correlation coefficients	53
98		Total correlations, r_{SC}	53
99		Shuffled total correlations	53
100		Separating Correlations & Anti-correlations	54
101	2.5.3	Conditioning on behavioural data	54
102		Linear regression	54
103		Elastic net regularisation	55
104		Conditional covariance	55
105		Measures of conditional correlation	56
106	2.5.4	Information Theory	56

107	Entropy $H(X)$	56
108	Maximum entropy limit	57
109	Mutual Information $I(X; Y)$	58
110	Variation of Information $VI(X, Y)$	60
111	Measuring entropies & mutual information	60
112	2.5.5 Network analysis	60
113	Correlation networks	60
114	Rectified correlations	61
115	Sparsifying data networks	61
116	Communities	61
117	Weighted configuration model	62
118	Sparse weighted configuration model	62
119	Spectral rejection	62
120	Node rejection	63
121	Community detection	64
122	2.5.6 Clustering Comparison	64
123	Adjusted Rand Index	64
124	Clusterings as random variables	65
125	Information based similarity measures	66
126	Information based metrics	66
127	Comparing detected communities and anatomical divisions	67
128	3 A simple two parameter distribution for modelling neuronal activity and cap-	
129	turing neuronal association	69
130	3.1 Introduction	72
131	3.2 Data	73
132	3.2.1 Experimental protocol	73
133	3.3 Methods	74
134	3.3.1 Binning data	74
135	3.3.2 Number of <i>active</i> neurons	74
136	3.3.3 Moving windows for measurements	74
137	3.3.4 Fano factor	76
138	3.3.5 Probability Distributions suitable for modelling ensemble activity	76
139	Association	76

140	Binomial distribution	77
141	Beta-binomial distribution	77
142	Conway-Maxwell-binomial distribution	78
143	3.3.6 Fitting	80
144	3.3.7 Goodness-of-fit	82
145	3.4 Results	82
146	3.4.1 Increases in mean number of active neurons and variance in number	
147	of active neurons at stimulus onset in some regions	82
148	Primary visual cortex	83
149	Hippocampus	83
150	Thalamus	83
151	3.4.2 Conway-Maxwell-binomial distribution is usually a better fit than bi-	
152	nomial or beta-binomial	83
153	3.4.3 Conway-Maxwell-binomial distribution captures changes in associ-	
154	ation at stimulus onset	88
155	3.4.4 Replicating stimulus related quenching of neural variability	88
156	3.5 Discussion	90
157	4 Studies with practical limitations & negative results	93
158	4.1 Dynamic state space model of pairwise and higher order neuronal correlations	96
159	4.2 A multiscale model for hierarchical data applied to	
160	neuronal data	96
161	Bibliography	99

List of Figures

162			
163	1.1	A: Example spike train (blue) and the corresponding GCaMP6s fluorescence	
164		trace (green), data replotted from (Berens et al., 2018). Inset shows zoomed	
165		section of traces to highlight slow decay of GCaMP6s fluorescence relative	
166		to spike time intervals. B: Schematic diagram of the neuron calcium and	
167		GCaMP computational model. C: Good visual match of data fluorescence	
168		trace (green) and model simulated fluorescence (orange) in response to an	
169		identical spike train (blue).	5
170	1.2	A: Workflow to compare spike inference for real versus simulated fluores-	
171		cence data. B: True positive rates achieved by three different spike inference	
172		algorithms when applied to observed spike trains, and simulated spike trains.	
173		Data points overlaid as blue circles. The performance is similar from real	
174		and simulated data for each of the algorithms.	8
175	1.3	Calcium Buffering Dynamics (a) The proportions of bound and free cal-	
176		cium concentrations within a cell, with the associated spike train. (b)-(f) The	
177		dynamics of the concentration of (b) excited indicator bound calcium, (c) in-	
178		dicator bound calcium, (d) immobile endogenous buffer bound calcium, (e)	
179		mobile endogenous buffer bound calcium, and (f) free calcium in response to	
180		an action potential at ~ 23.2 s.	9
181	1.4	(a) An example trace for each of the five pairs of values used for the binding	
182		and unbinding rates of the fluorescent calcium indicator. (b) The signal-to-	
183		noise ratio of the modelled fluorescence traces using each of the four per-	
184		turbed values, and the experimental value. The SNRs for the two pairs with	
185		values lower than the experimental value are lower than the experimental pair	
186		or the higher value pairs. (c) The true-positive rates of the deconvolution al-	
187		gorithm's predictions when inferring from the observed data, and inferring	
188		from modelled traces using the perturbed and experimental values.	12

189	1.5	(a) An example trace for each of the five perturbed values for the concentration of fluorescent calcium indicator. The top two traces are produced by the lower perturbed values, the middle trace is produced by the experimental value, and the lowest two traces are produced when using the higher perturbed values. (b) The signal-to-noise ratio of the modelled fluorescence traces using each of the four perturbed values, and the experimental value. Extreme perturbations of the concentration either above or below the experimental level lowered the SNR. (c) The true-positive rates of the deconvolution algorithm's predictions when inferring from the observed data, and inferring from modelled traces using the perturbed and experimental values. We found that the algorithms performs equally badly on the two most extreme values, and performs equally well on the experimental value, and the next higher perturbed value.	13
202	1.6	(a) An example trace for each of the five perturbed values for the concentration of immobile endogenous buffer. (b) The signal-to-noise ratio of the modelled fluorescence traces using each of the four perturbed values, and the experimental value. The lower values for the immobile buffer produce the same SNR as the experimental value. But the higher perturbed values produce fluorescence traces with a lower SNR. (c) The true-positive rates of the deconvolution algorithm's predictions when inferring from the observed data, and inferring from modelled traces using the perturbed and experimental values.	15
211	1.7	Simulating fluorescence traces at different firing rates Example modelled traces created using simulated spike trains with a mean firing rate of 1Hz (left column), 5Hz (middle column), and 10Hz (right column). Note the difference in amplitude with different mean firing rates.	16
215	1.8	Inference quality and $\Delta F/F_0$ vs Firing rate (left) The spike inference accuracy when applied to 30 traces created using simulated spike trains with mean firing rates of 1, 5, and 10 Hz. (right) The mean $\Delta F/F_0$ across those 30 traces for each frequency.	16

219	2.1	(A) An example of the correlation coefficients between two different pairs	
220		of cells, one where both cells are in the same brain region (intra-regional	
221		pair), and one where both cells are in different brain regions (inter-regional	
222		pair). The correlation coefficients have been measured using different time	
223		bin widths, ranging from 5ms to 3s. Note the increasing amplitude of the	
224		correlations with increasing bin width. (B) A raster plot showing the spike	
225		times of each pair of cells.	34
226	2.2	Mean correlation coefficients measured from pairs of 50 randomly chosen	
227		neurons. (A) All possible pairs, (B) positively correlated pairs, and (C) neg-	
228		atively correlated pairs. (D) Mean and standard error of χ^2 test statistics for	
229		Poisson and Gaussian distributions fitted to neuron spike counts.	35
230	2.3	(Left)The mean intra-region and inter-region correlations using all possible	
231		pairs of ~ 500 neurons, spread across 9 different brain regions. (Right)	
232		Courtesy of Stringer et al. (2019), mean inter-regional (out-of-area) correla-	
233		tion coefficients vs mean intra-regional (within-area) correlation coefficients	
234		for a bin width of 1.2s. Note that the intra-regional coefficients are higher in	
235		each case.	37
236	2.4	The mean intra-regional correlations (coloured dots) and mean inter-regional	
237		correlations (black dots) for a given region, indicated on the x-axis, for dif-	
238		ferent time bin widths. Each black dot represents the mean inter-regional	
239		correlations between the region indicated on the x-axis and one other re-	
240		gion. (A) shows these measurements when we used a time bin width of 5ms.	
241		(B) shows these measurements when we used a time bin width of 1s. Note	
242		that the difference between the mean inter-regional correlations and mean	
243		intra-regional correlations is smaller for 1s bins.	38
244	2.5	Mean inter-regional (main diagonal) and intra-regional (off diagonal) corre-	
245		lation coefficients. (a) Shows these measurements when spike times were	
246		binned using 5ms time bins. (b) Shows the same, using 1s time bins. Note	
247		that the matrices are ordered according to the main diagonal values, therefore	
248		the ordering is different in each subfigure.	39

249	2.6	The number of dimensions in the k -partite and connected structure in the correlation based networks beyond the structure captured by a sparse weighted configuration null network model (see section 2.5.5), shown for different time	
250		bin widths. Note that the k -partite structure disappears for time bin width	
251		greater than 200ms for all three subjects. The dimension of the connected	
252		structure reduces with increasing bin width for 2 of the 3 subjects (top row).	41
253			
254	2.7	(A) and (C) Correlation matrices with detected communities indicated by	
255		white lines. Each off main diagonal entry in the matrix represents a pair of	
256		neurons. Those entries within a white square indicate that both of neurons are	
257		in the same community as detected by our community detection procedure.	
258		Matrices shown are for 5ms and 1s time bin widths respectively. (B) and	
259		(D) Matrices showing the anatomical distribution of pairs along with their	
260		community membership. Entries where both cells are in the same reigon are	
261		given a colour indicated on the colour bar. Entries where cells are in different	
262		regions are given the grey colour also indicated on the colour bar.	42
263			
264	2.8	(a) The variation of information is a measure of distance between clusterings.	
265		The distance between the anatomical ‘clustering’ and community detection	
266		‘clustering’ increases with increasing time bin width. (b) The adjusted Rand	
267		index is a normalised similarity measure between clusterings. The anatomi-	
268		cal and community detection clusterings become less similar as the time bin	
269		width increases.	43
270	2.9	Comparing the components of the spike count covariance across different	
271		values for the time bin width. We observed a consistent increase in $E[\text{cov}(X, Y Z)]$	
272		as the time bin width increased. But we saw different trends for $\text{cov}(E[X Z], E[Y Z])$	
273		for each mouse.	45
274	2.10	Comparing the components of the total spike count covariance across differ-	
275		ent values for the time bin width. We saw a consistent increase in $\rho_{X,Y Z}$ as	
276		the time bin width increased in all three subjects. But we saw different trends	
277		for in ρ_{signal} for each of the subjects.	46

278	2.11	Matrices showing the regional membership of pairs by colour, and the communities in which those pairs lie. (A-B) Detected communities and regional membership matrix for network based on rectified spike count correlation $\rho_{X,Y Z}$, using time bin widths of 0.005s and 1s respectively. (C-D) Detected communities and regional membership matrix for network based on rectified signal correlation ρ_{signal} , using time bin widths of 0.005s and 1s respectively.	47
279			
280			
281			
282			
283			
284	2.12	Distance and similarity measures between the anatomical division of the neurons, and the communities detected in the network based on the spike count correlations $\rho_{X,Y Z}$. (a) The variation of information is a ‘distance’ measure between clusterings. The distance between the anatomical ‘clustering’ and the community clustering increases as the time bin width increases. (b) The adjusted Rand index is a similarity measure between clusterings. The detected communities become less similar to the anatomical division of the cells as the time bin width increases.	48
285			
286			
287			
288			
289			
290			
291			
292	2.13	Distance and similarity measures between the anatomical division of the neurons, and the communities detected in the network based on the signal correlations ρ_{signal} . (a) The variation of information is a ‘distance’ measure between clusterings. The distance between the anatomical ‘clustering’ and the community clustering increases as the time bin width increases. (b) The adjusted Rand index is a similarity measure between clusterings. The detected communities become less similar to the anatomical division of the cells as the time bin width increases.	49
293			
294			
295			
296			
297			
298			
299			
300	2.14	Probe Locations: The locations of the probes in each of the three mouse brains (Stringer et al., 2019).	52
301			
302	2.15	Entropy Limit: The upper limit on entropy of binned spike count data as a function of the maximum observed spike count. The orange line is the analytical maximum. The blue line is the entropy of samples with $N = 1000$ data points taken from the discrete uniform distribution.	58
303			
304			
305			
306	3.1	Figures showing the over-dispersion possible for a beta-binomial distribution relative to a binomial distribution. Parameters are shown in the captions. . .	78
307			

308	3.2	Figures showing (A) the under-dispersion and (B) over-dispersion permitted	
309		by the COMb distribution relative to a binomial distribution. (C) illustrates	
310		that the p parameter of the COMb distribution does not correspond to the	
311		mean of the distribution, as it does for the binomial and beta-binomial dis-	
312		tributions. (D) shows a heatmap for the value of the Kullback-Liebler diver-	
313		gence between the COMb distribution and the standard binomial distribution	
314		with same value for n , as a function of p and ν . Parameters are shown in the	
315		captions.	81
316	3.3	(A) Raster plot showing the spikes fired by 33 randomly chosen neurons in	
317		the primary visual cortex. (B-C) (B) average and (C) variance of the number	
318		of active neurons, measured using a sliding window 100ms wide, split into	
319		100 bins. The midpoint of the time interval for each window is used as the	
320		timepoint (x-axis point) for the measurements using that window. The grey	
321		shaded area indicates the presence of a visual stimulus. The opaque line is	
322		an average across the 160 trials that included a visual stimulus of any kind.	
323		We can see a transient increase in the average number of active neurons and	
324		the variance of this number, followed by a fluctuation and another increase. .	84
325	3.4	(A) Raster plot showing the spikes fired by 33 randomly chosen neurons in	
326		the hippocampus. (B-C) (B) average and (C) variance of the number of active	
327		neurons, measured using a sliding window 100ms wide, split into 100 bins.	
328		The midpoint of the time interval for each window is used as the timepoint (x-	
329		axis point) for the measurements using that window. The grey shaded area	
330		indicates the presence of a visual stimulus. The opaque line is an average	
331		across the 160 trials that included a visual stimulus of any kind. We can see	
332		a transient increase in the average number of active neurons and the variance	
333		of this number at stimulus onset.	85

- 334 3.5 (A) Raster plot showing the spikes fired by 33 randomly chosen neurons in
 335 the thalamus. (B-C) (B) average and (C) variance of the number of active
 336 neurons, measured using a sliding window 100ms wide, split into 100 bins.
 337 The midpoint of the time interval for each window is used as the timepoint (x-
 338 axis point) for the measurements using that window. The grey shaded area
 339 indicates the presence of a visual stimulus. The opaque line is an average
 340 across the 160 trials that included a visual stimulus of any kind. We can
 341 see an immediate increase at stimulus onset, a subsequent fall, and another
 342 sustained increase until the stimulus presentation ends. 86
- 343 3.6 (A) An example of the binomial, beta-binomial, and Conway-Maxwell-binomial
 344 distributions fitted to a sample of neural activity. The Conway-Maxwell-
 345 binomial distribution is the best fit in this case. The histogram shows the
 346 empirical distribution of the sample. The probability mass function of each
 347 distribution is indicated by a different coloured line. (B) Across all samples
 348 in all trials, the proportion of samples for which each fitted distribution was
 349 the the best fit. The Conway-Maxwell-binomial distribution was the best fit
 350 for 93% of the samples taken from V1 using a bin width of 1ms. 87
- 351 3.7 (A) We fit a Conway-Maxwell-binomial distribution to the number of active
 352 neurons in 1ms time bins of a 100ms sliding window. We did this for all
 353 trials with a visual stimulus and took the average across those trials. We
 354 see a transient drop in value for the distribution's ν parameter at stimulus
 355 onset. This shows an increase in association between the neurons. (B) We
 356 measured the correlation coefficient between the spike counts of all possible
 357 pairs of neurons in the same sliding window. We took the average of those
 358 coefficients. We also did this for every visually stimulated trial, and took
 359 the average across trials. The increase in association is not reflected with an
 360 increase in average correlation. 89
- 361 3.8 (A) The mean Fano factor of the spike counts of the cells in the primary visual
 362 cortex. Means were taken across cells first, then across trials. There was a
 363 significant decrease in the Fano factors immediately after stimulus onset. (B)
 364 The mean Fano factor of the spike counts of the cells in the motor cortex. No
 365 significant change in measurements at any point. 90

366 List of Tables

367	1.1	Fixed parameters A table of the parameters fixed before optimising the	
368		model. The values of these parameters could be changed to model differ-	
369		ent fluorescent calcium indicators.	23
370	3.1	Details of the different bin width and analysis window sizes used when bin-	
371		ning spike times, and analysing those data.	75
372	3.2	Relative dispersion of the COMb distribution, and association between Bernoulli	
373		variables as represented by the value of the ν parameter.	80
374	3.3	Proportion of samples for which each distribution was the best fit, grouped	
375		by bin width. The COMb distribution is the best fit most of the time.	88

For/Dedicated to/To my...

377 **Chapter 1**

378 **Sensitivity of the**
379 **spikes-to-fluorescence transform to**
380 **calcium indicator and neuron**
381 **properties**

UNIVERSITY OF BRISTOL

Abstract

Engineering

Department of Computer Science

Doctor of Philosophy

Investigating, implementing, and creating methods for analysing large neuronal ensembles

by Thomas J. DELANEY

Fluorescent calcium indicators such as GCaMP are widely used to monitor neuronal activity. However the relationship between the fluorescence signal and the underlying action potential firing is poorly understood. This lack of knowledge makes it difficult for experimenters to decide between different indicator variants for a given application. We addressed this problem by studying a basic biophysical model of calcium dynamics in neuronal soma. We fit the model parameters to publicly available data where GCaMP6s fluorescence and whole-cell electrophysiological recordings were made simultaneously in the same single neurons. We systematically varied the model's parameters to characterise the sensitivity of spike train inference algorithms to the calcium indicator's main biophysical properties: binding rate, dissociation rate, and molecular concentration. This model should have two potential uses: experimental researchers may use it to help them select the optimal indicator for their desired experiment; and computational researchers may use it to generate simulated data to aid design of spike inference algorithms.

1.1 Introduction

Although fluorescent calcium indicators such as GCaMP are widely used to monitor neuronal activity, the relationship between the fluorescence signal and the underlying action potential firing is imperfect. The fluorescence signal has a low signal-to-noise ratio, and most indicators' kinetics are slow relative to the millisecond-timescale dynamics of the membrane voltage (example in Figure 1). This makes spike inference difficult. Furthermore, the effects of the indicator and cell properties on the fluorescence signal are unknown. For example, genetically encoded indicators can accumulate within neurons over weeks and months (Chen et al., 2013). Studies using calcium-sensitive fluorescent dyes have shown that indicator concentration has substantial effects on the spike-to-fluorescence relationship (Maravall et al., 2000). Therefore spike rates inferred from GCaMP fluorescence signals may give misleading results if comparing across imaging sessions. More generally, the poor understanding of the spike-to-fluorescence transform means experimenters may not know whether to trust the outputs of spike train inference methods in any given application.

Spike trains are usually inferred from the time series of intensity values of one pixel of the fluorescence image, where the pixel is located at the cell's soma. The problems of identifying these pixels, and inferring spikes from their time series can be solved separately or together. When attempting to infer spikes, the fluorescence trace is modelled as a linear combination of calcium concentration dynamics, a baseline calcium concentration, and some Gaussian noise. The calcium concentration dynamics are modelled as an autoregressive process of degree 1 or 2 with a pulse input corresponding to the spike train, or the number of spikes fired in a time step. The model includes no dynamics for the fluorescent indicator itself. Furthermore, in order to make this model into an easily solvable linear programming problem the number of spikes fired in a timestep is not restricted to non-negative integers but to arbitrary non-negative values (Vogelstein et al., 2010; Pnevmatikakis et al., 2016; Friedrich and Paninski, 2016; Pnevmatikakis et al., 2013; Pnevmatikakis et al., 2014). More biologically inspired spike inference models do exist (Deneux et al., 2016), but their fundamentals are very similar. In this work, we investigated the effect of changing dynamics and buffer concentrations on the accuracy of the inference algorithms based on these models.

The aim of this project was to model the fluorescence traces produced by a fluorescent calcium indicator in a neuron soma resulting from a specific spike train, given calcium indicator parameters such as binding rate, dissociation rate, and molecular concentration. Such

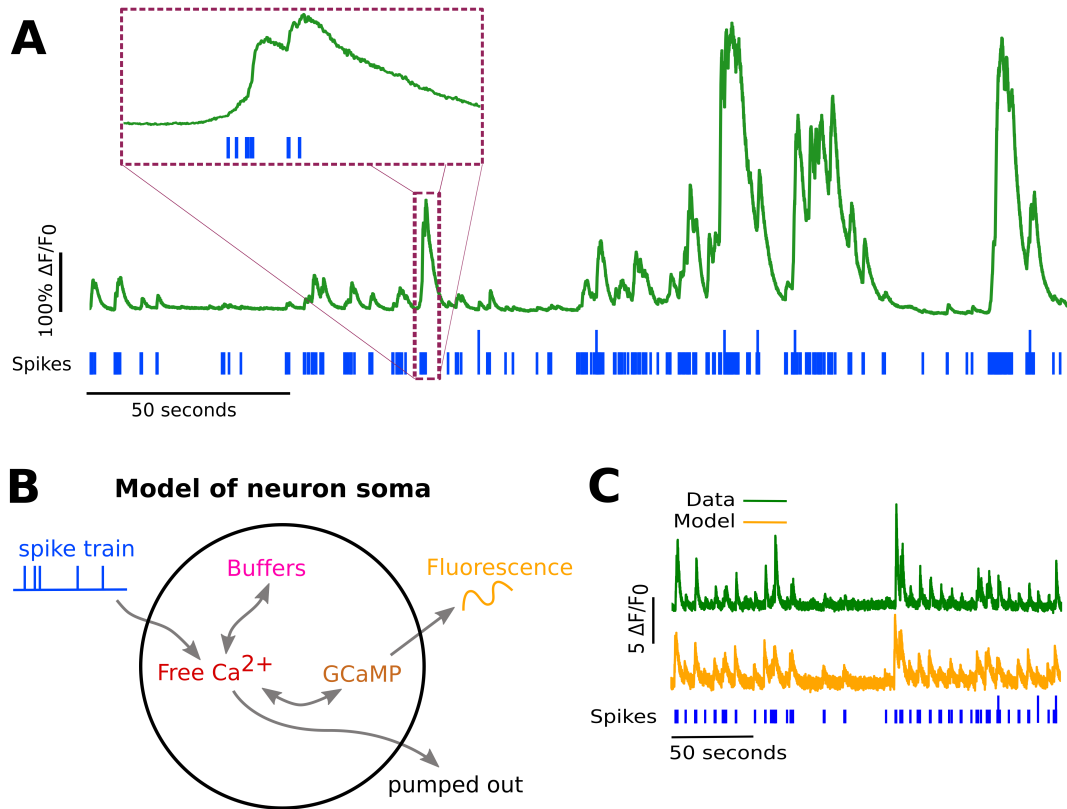


FIGURE 1.1:

A: Example spike train (blue) and the corresponding GCaMP6s fluorescence trace (green), data replotted from (Berens et al., 2018). Inset shows zoomed section of traces to highlight slow decay of GCaMP6s fluorescence relative to spike time intervals.

B: Schematic diagram of the neuron calcium and GCaMP computational model.

C: Good visual match of data fluorescence trace (green) and model simulated fluorescence (orange) in response to an identical spike train (blue).

435 a model would allow benchmarking of various spike inference algorithms, and enable under-
 436 standing of how indicator characteristics affect the quality of spike train inference.

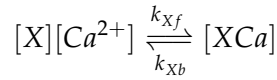
437 The model we developed consisted of free calcium, fluorescent indicator molecules, and
 438 mobile and immobile endogenous calcium buffers. The indicator molecules which were
 439 bound to a calcium molecule could be either excited, i.e. able to release a photon, or relaxed.
 440 In order to reproduce the noise inherent in the data collection, we modelled the release of
 441 photons from the excited indicator bound calcium as a stochastic process.

442 The fluorescence traces produced by the simulation were calibrated to reproduce the
 443 signal-to-noise ratio observed in experimental data. Previously published spike inference
 444 algorithms were then used to infer spike trains from the experimental fluorescence traces and
 445 the modelled fluorescence traces. The parameters of the model were then varied in order to
 446 determine the effect on the system dynamics and the effects on spike inference.

1.2 Results

1.2.1 A biophysical computational model can generate accurate fluorescence traces from spike trains

To study the relationship between action potential firing and calcium fluorescence, we built a computational model of calcium dynamics in a neuronal soma. The model consisted of four dynamic variables: the concentration of free calcium, two types of endogenous buffer, and the calcium-sensitive fluorescent indicator. Each of the buffers and the indicator could independently bind and unbind with calcium. These reactions were modelled as



where X is the buffer concentration and Ca^{2+} is the calcium concentration. Each species could therefore exist in two states: either bound with calcium or unbound. To model the imaging process, we also added a third, excited state to the indicator. When in the calcium-bound state, the indicator could be converted to an excited state, corresponding to the absorption of a photon. The rate of this excitation process could be interpreted as the intensity of the light illuminating the sample. Once excited, the species decayed back to the unexcited state at a fixed rate, corresponding to the spontaneous emission of photons. The total emitted fluorescence signal was interpreted as proportional to this de-excitation flux. To represent experimental noise in the photon capture process, we drew a random number of captured photons at each time step from a binomial distribution, parameterised by a number p that corresponds to the mean fraction of released photons that are captured.

The model had 17 parameters in total describing the molecules' concentrations and reaction rates (Methods). We set 13 of these parameters to values from the literature. The remaining 4 parameter values we fit to publicly-available data (Berens et al., 2018), briefly explained as follows (see Methods for full details). Single neurons from acute rat cortical slices expressing GCaMP6f were imaged with two-photon microscopy while the membrane potentials of the somata of the same neurons were simultaneously recorded via whole-cell patch clamp electrophysiology. In this dataset, the electrical recordings give unambiguous information about neurons' spike times. To do the parameter fitting, we feed these spike trains as inputs to the computational model. After running, the model returns a simulated fluorescence trace. We aimed to find the model parameter values that give the best match between this simulated fluorescence trace and the real fluorescence time series recorded in

the corresponding neuron. To do this we used a suite of optimisation procedures to jointly fit both the real neuron’s fluorescence time series and power spectrum, which capture complementary information about the spikes-to-fluorescence mapping (Methods). We performed the fitting procedure independently for each of the 20 neurons in the spikefinder dataset (<http://spikefinder.org>). After fitting, the model produced realistic-looking fluorescence time series (Figure 1.1).

1.2.2 Spike inference algorithms perform similarly on real data compared with time series simulated from the model

Researchers often pass the fluorescence time series through a spike inference tool before performing further statistical analyses. These spike inference algorithms take the fluorescence trace as input and attempt to estimate the neuronal spike train that triggered them (Vogelstein et al., 2010; Pnevmatikakis et al., 2016; Friedrich and Paninski, 2016; Pnevmatikakis et al., 2013; Pnevmatikakis et al., 2014; Deneux et al., 2016). Part of our motivation for building this model was to allow us to ask the question: how do the properties of the cell and the calcium indicator affect the quality of spike inference? In order to trust the conclusions from our model, we should first be confident that spike inference from our simulated fluorescence traces is similar to that from the real data. To test this we passed each of the simulated fluorescence traces through three previously published spike inference algorithms, quantified their performance against the ground-truth electrophysiology data, repeated the procedure for the real calcium fluorescence time series, and compared the accuracy of the inference processes in all cases. The *true positive rate*, also known as the *recall*, the *sensitivity*, or the *probability of detection* of spike inference varied across the three inference algorithms we tried (p value and statistical test here). The constrained non-negative matrix deconvolution algorithm (Pnevmatikakis et al., 2016) (CNMD algorithm) correctly detected approximately 45% of the true spikes, the OASIS algorithm (Friedrich and Paninski, 2016) correctly detected approximately 35% of the true spikes, and the ML spike algorithm (Deneux et al., 2016) correctly detected approximately 15% of the true spikes (see figure 1.2). Notably, for two of the three inference algorithms, the quality of inference was also fairly consistent for individual spike trains, not just the group means ($p > 0.05$, paired t-test). This demonstrates that the models were generating fluorescence time series that were similarly difficult to decode as the real data, in ways that were not specific to any one inference algorithm. This is evidence that the models captured real aspects of the spikes-to-fluorescence transform.

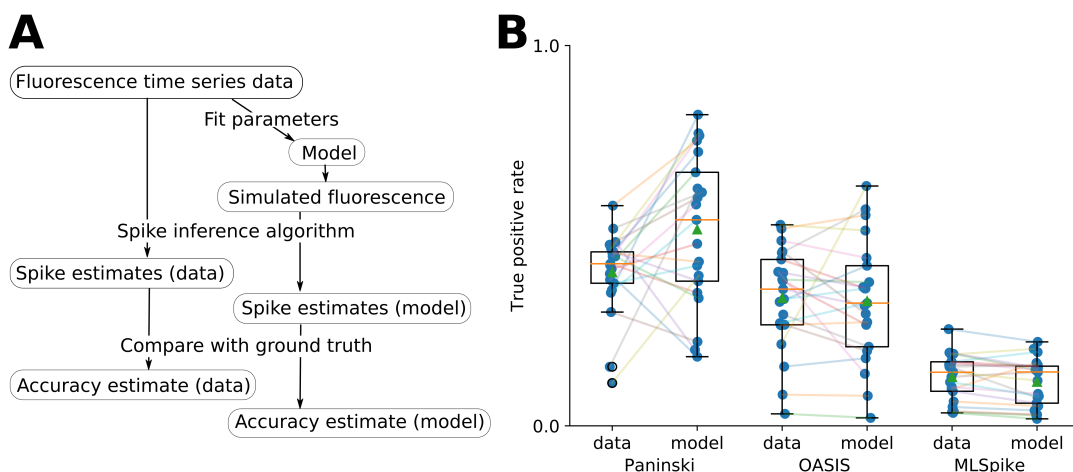


FIGURE 1.2:

A: Workflow to compare spike inference for real versus simulated fluorescence data.

B: True positive rates achieved by three different spike inference algorithms when applied to observed spike trains, and simulated spike trains. Data points overlaid as blue circles. The performance is similar from real and simulated data for each of the algorithms.

1.2.3 Relative effects of various buffers to the fluorescence signal

One of the benefits of computational models over laboratory experiments is that we can observe all the variables in the simulation to gain insight into the system's dynamics, which can be difficult to do in the lab. We plotted the concentrations of the various species over time for a version of the model fit to one data set, in response to the same train of spikes used for fitting (figure 1.3). Figure 1.3a shows the absolute values of the species concentrations, summed. Consistent with experimental estimates (Maravall et al., 2000), only a small fraction ($\sim 0.1\%$) of calcium is free and unbound to any buffer. Of the bound calcium, the vast majority, ($\sim 96\%$) is bound to the GCaMP indicator. The two types of endogenous buffer are bound to the remaining calcium ($\sim 4\%$). An influx of calcium from a single spike adds very little to the total calcium, in relative terms (red line in Figure 3a).

When calcium entered the model neuron it was rapidly buffered (Bartol et al., 2015). However the relative fractions of which buffer molecules bound to the influxed calcium was dynamic, and changed over time. Figure 1.3 (b-f) shows the time course of the various species over time in response to a calcium influx event from a single action potential. Crucially, the indicator $[BCa]$ competed with the endogenous buffers $[ImCa]$ and $[ECa]$ – all three bind calcium on similar timescales. This implies that the timecourse and amplitude of the $[BCa]$ variable will also depend on the binding rates and availabilities of the endogenous buffers. For example if we decreased the concentration of an endogenous buffer, we might

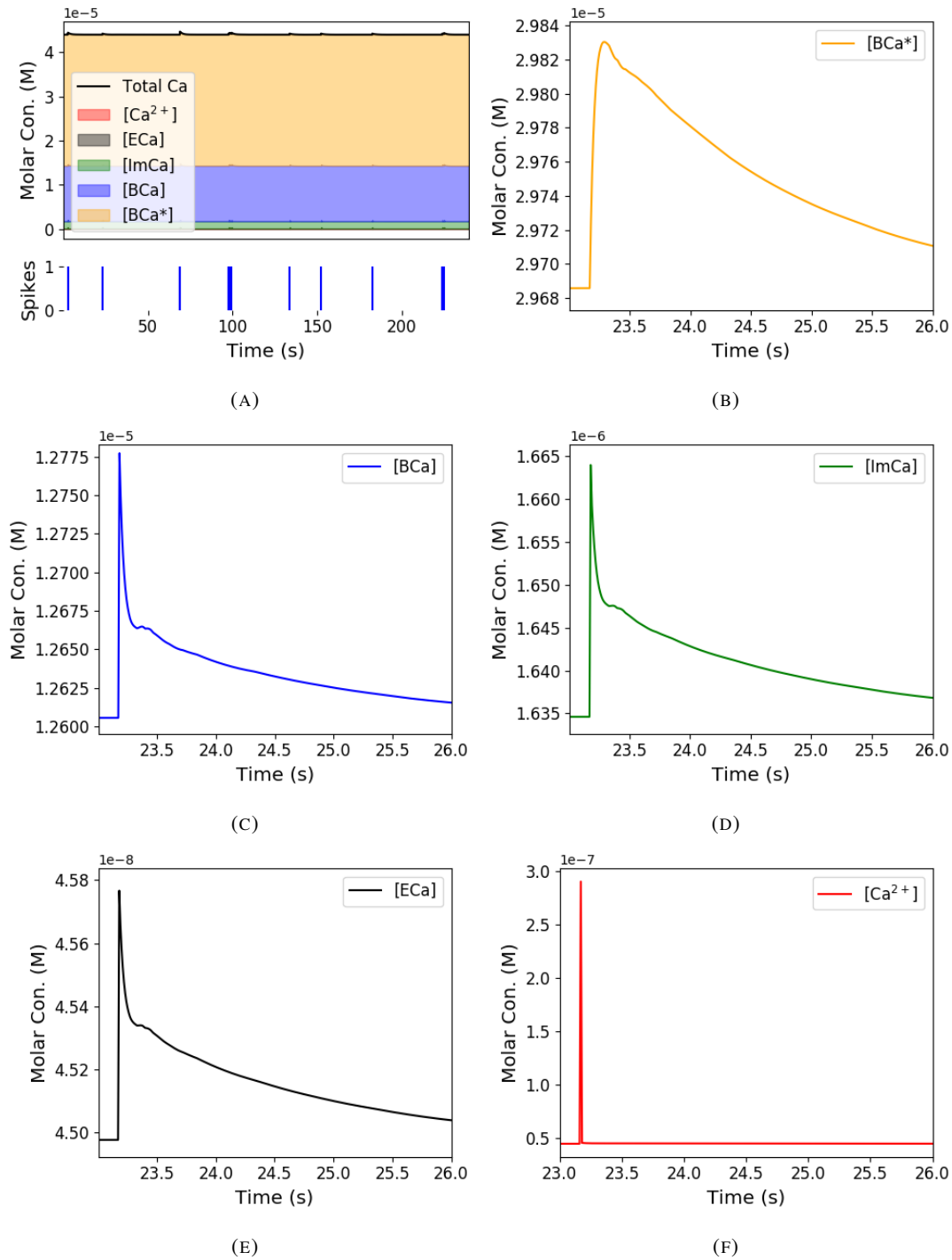


FIGURE 1.3: **Calcium Buffering Dynamics** (a) The proportions of bound and free calcium concentrations within a cell, with the associated spike train. (b)-(f) The dynamics of the concentration of (b) excited indicator bound calcium, (c) indicator bound calcium, (d) immobile endogenous buffer bound calcium, (e) mobile endogenous buffer bound calcium, and (f) free calcium in response to an action potential at ~ 23.2 s.

expect both a faster rise time and greater peak amplitude of the $[BCa]$ signal in response to a calcium influx event. The slowest component of the decay had a similar time constant for $[BCa]$, $[ImCa]$ and $[ECa]$, which in turn matched the $[Ca]$ extrusion time constant in our model ($\sim 6.29 \times 10^{-22} \text{Ms}^{-1}$). This implies that the buffers and the indicator had reached a dynamic equilibrium and were jointly tracking the free calcium concentration as calcium was slowly extruded from the cell.

Interestingly the excited bound calcium species ($[BCa^*]$) showed a qualitatively different timecourse in response to a calcium influx event. This concentration is subject to the added ‘excitation and release’ dynamic, where a certain proportion of the concentration absorbs the energy from an incoming photon and goes into an ‘excited state’ at each time step. A certain proportion of the concentration releases a photon and reverts to a ‘relaxed state’ at each timestep also. This means that the excited bound calcium lags behind the bound calcium trace. We could think of the excited bound calcium trace as a low pass filtered version of the bound calcium trace.

1.2.4 Spike inference accuracy is sensitive to indicator properties, and likely varies within and between cells

The above results imply that the fluorescence signal depends on the relative properties of both GCaMP and the endogenous buffers. We next used the model to directly ask how sensitive spike inference was to these components. We focused on three key parameters that likely vary from cell to cell and experiment to experiment: GCaMP binding kinetics, GCaMP concentration, and endogenous buffer concentration.

Several variants of GCaMP itself have been made that differ in calcium binding kinetics, baseline fluorescence, fluorescence efficiency, and other factors. For example, GCaMP6f has a decay time constant of $\sim 1\text{s}$, while GCaMP6s has a decay time constant of $\sim 2\text{s}$ (Chen et al., 2013). Here we asked how these differences in binding kinetics affect spike inference. We jointly varied the calcium binding and unbinding rates of the indicator by the same factor over a range from 100-fold slower to 100-fold faster from the fitted values, and simulated the fluorescence response for each of the parameter settings in response to the same spike trains as before (figure 1.4). Notably this manipulation does not affect the indicators affinity, and therefore would not affect steady-state responses to prolonged changes in calcium. Instead it is likely to affect its sensitivity to the spike train dynamics. We computed two summary measures from the simulated fluorescence traces: the signal-to-noise ratio for a single spike (Methods, section 1.4.6), and the accuracy of spike inference for each of the spike trains. We

observed a reduction in the signal-to-noise ratio and the spike inference quality when we set the binding and unbinding rates were set to one hundredth of their fitted values, and to one tenth of their fitted values. When we increased the value of both binding rates, we observed no change in these measurements. The reduction in both rates lead to smaller increases in fluorescence in response to an action potential and a longer decay time (figure 1.4a), this caused the reduction in signal-to-noise ratio. As both rates were increased, the change in $\Delta F/F_0$ in response to an action potential increased and the decay time decreased slightly, but the fluorescence trace created by these values was very similar to the trace created by the fitted values.

Second, the overall concentrations of GCaMP often varies from cell to cell. For example different cells, even of the same type in the same tissue, can express different levels of GCaMP, due to proximity to the infection site, or the cell becoming ‘nuclear-filled’ (Tian et al., 2009; Chen et al., 2013). Also, GCaMP is often used for longitudinal experiments where the same cells are re-imaged across multiple days or weeks. However since GCaMP expression typically ramps up over time (Chen et al., 2013), the accuracy of spike inference may differ across multiple longitudinal recordings in the same cell. We addressed this by varying the concentration of calcium indicator in the model, simulating spike trains and measuring signal-to-noise ratio and spike inference accuracy on the resulting fluorescence traces. Both increasing and decreasing the concentration of the indicator had effects on the fluorescence trace, signal-to-noise ratio, and spike inference. The signal-to-noise ratio and spike inference quality decreased with decreased indicator concentration, and both showed a decrease when the indicator concentration was increased to 100 times it’s fitted value (figure 1.5). The signal-to-noise ratio showed an increase when the indicator concentration was increased to 10 times it’s fitted value, but there was no corresponding change in the spike inference quality. The decrease in indicator concentration caused a reduction in the increase in $\Delta F/F_0$ in response to an action potential, and an increase in the decay time of this increase (figure 1.5a). The increase in indicator concentration had the opposite effect, it caused an increase in the change in $\Delta F/F_0$ in response to an action potential, and a decrease in the decay time.

Third, the concentration and types of endogenous calcium buffers also vary from neuron to neuron, both within and between cell types (Bartol et al., 2015; Maravall et al., 2000; Neher and Augustine, 1992). Since the calcium buffer capacity of neurons is high, around 50-70 (Lee et al., 2000) in excitatory hippocampal pyramidal cells, around 100-250 (Lee et al., 2000) in inhibitory hippocampal pyramidal cells, and 900-200 in Purkinje cells (depending on the age of the subject), these endogenous buffers compete with GCaMP for binding

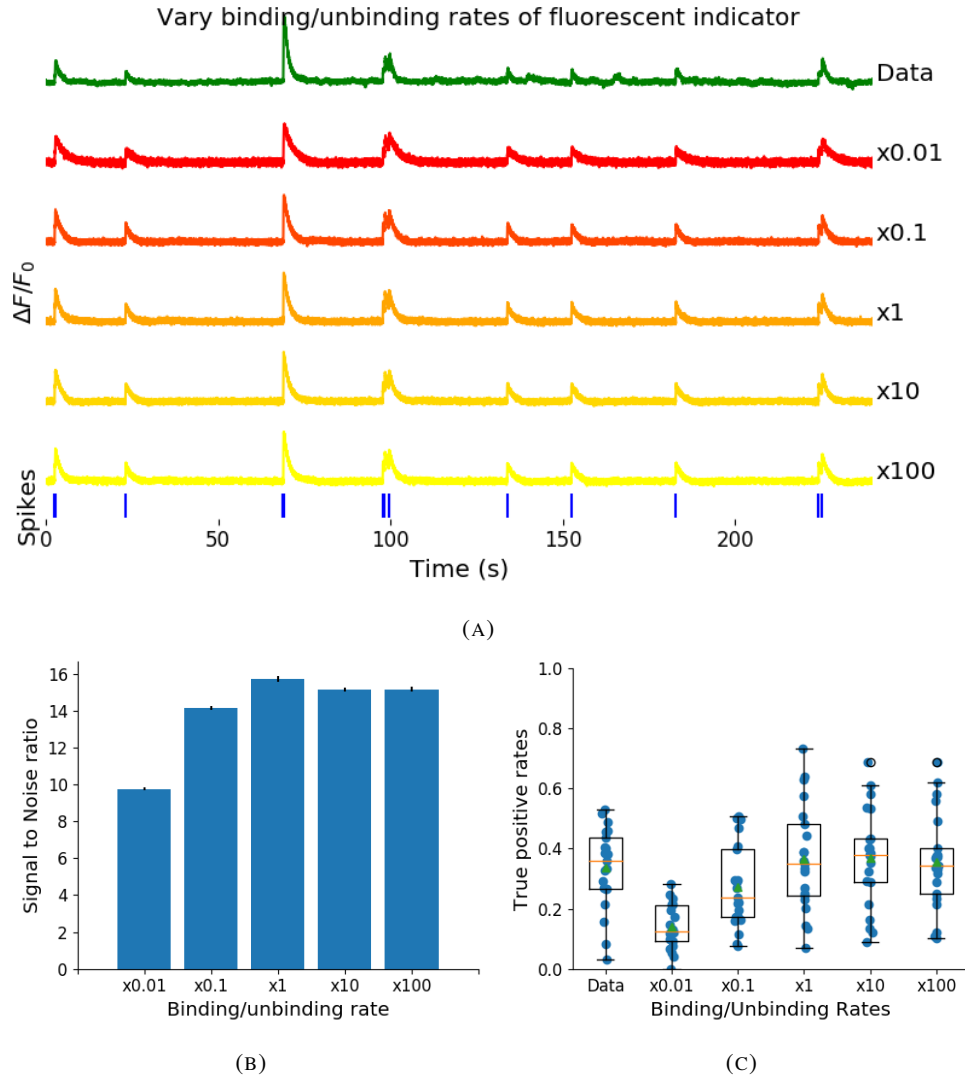


FIGURE 1.4: (a) An example trace for each of the five pairs of values used for the binding and unbinding rates of the fluorescent calcium indicator. (b) The signal-to-noise ratio of the modelled fluorescence traces using each of the four perturbed values, and the experimental value. The SNRs for the two pairs with values lower than the experimental value are lower than the experimental pair or the higher value pairs. (c) The true-positive rates of the deconvolution algorithm's predictions when inferring from the observed data, and inferring from modelled traces using the perturbed and experimental values.

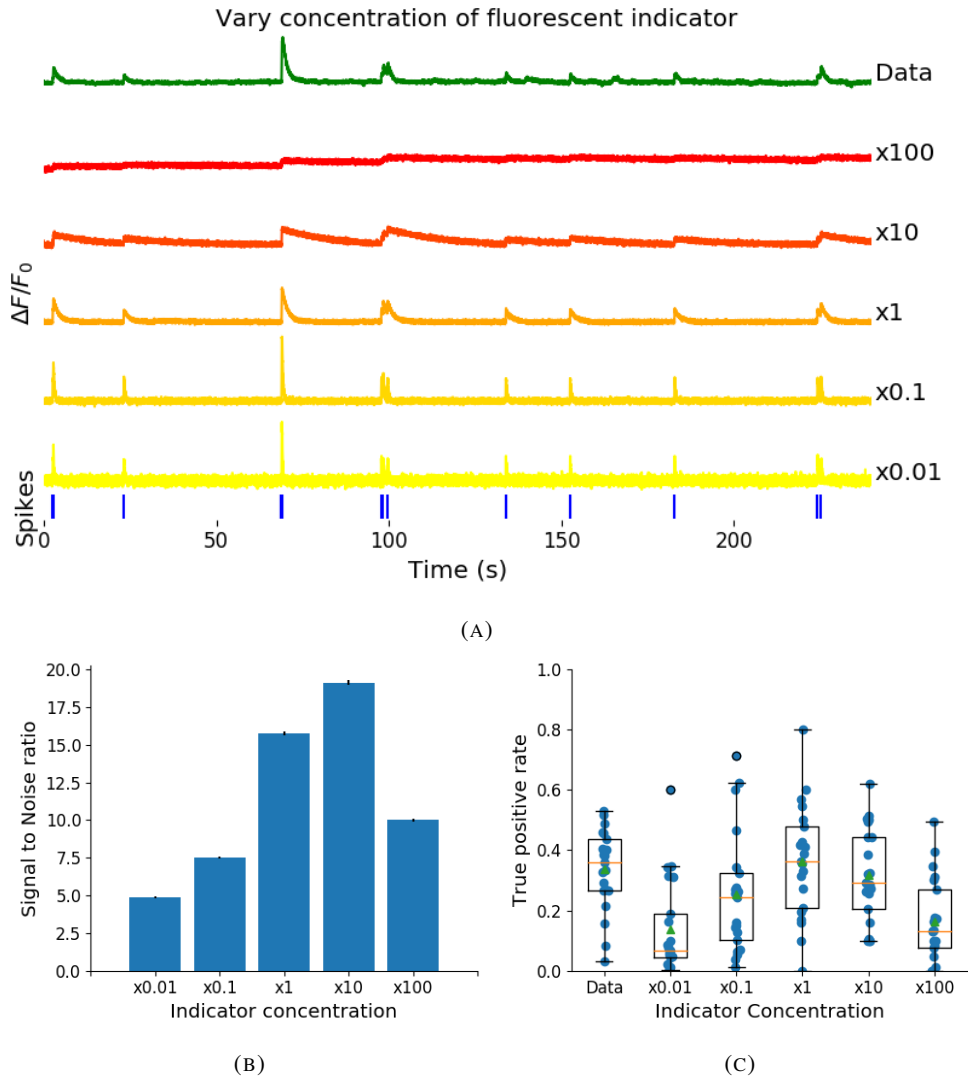


FIGURE 1.5: (a) An example trace for each of the five perturbed values for the concentration of fluorescent calcium indicator. The top two traces are produced by the lower perturbed values, the middle trace is produced by the experimental value, and the lowest two traces are produced when using the higher perturbed values. (b) The signal-to-noise ratio of the modelled fluorescence traces using each of the four perturbed values, and the experimental value. Extreme perturbations of the concentration either above or below the experimental level lowered the SNR. (c) The true-positive rates of the deconvolution algorithm's predictions when inferring from the observed data, and inferring from modelled traces using the perturbed and experimental values. We found that the algorithms performs equally badly on the two most extreme values, and performs equally well on the experimental value, and the next higher perturbed value.

to calcium, and variations in endogenous buffer concentration may affect GCaMP signal and therefore spike inference. To address this we varied the concentration of the endogenous buffer in the model neuron over five orders of magnitude from 0.8 to 8000 μM , simulated calcium fluorescence traces in response to the same set of spike trains, and performed spike inference on the resulting fluorescence time series. Increasing the endogenous buffer concentration had a substantial effect on the GCaMP fluorescence signal, both decreasing its amplitude and slowing its kinetics (figure 1.6(a)). This corresponded with a decrease in both single-spike signal-to-noise ratio (figure 1.6(b)) and spike inference accuracy (figure 1.6(c)). In contrast, decreasing endogenous buffer capacity from the fitted value had little effect on either the GCaMP signal or spike inference (figure 1.6).

1.2.5 Single spike inference accuracy drops for high firing rates, but firing rate itself can be estimated from mean fluorescence amplitude

The fluorescence signal recorded from neurons using calcium indicators is typically much slower than changes in membrane potential for two reasons: first, because the calcium and the indicator have slow binding and unbinding kinetics, the signal is a low-pass filtered version of the membrane potential. Second, neuronal two-photon imaging experiments are often performed in scanning mode, which limits their frame rate to $\sim 10\text{Hz}$ or slower. This implies that multiple spike events that occur close in time might be difficult to resolve from a calcium indicator time series. Many cells, especially several types of inhibitory interneurons, fire tonically at rates higher than 10Hz. We used the model to test whether spike inference accuracy depended on the neuron's firing frequency by driving the cell with spike trains sampled from a Poisson processes of varying frequency. We simulated a variable firing rate using an Ornstein-Uhlenbeck process, and simulated the spike trains using a Poisson distribution with its rate taken from this process. Because of the high frequency firing rate of these spike trains, we using the accuracy as the measure of spike inference quality. We simulated 30 spike trains at average firing rate of 1, 5, and 10Hz, and measured the spike inference quality of all these traces. Spike inference accuracy decreased with increasing firing rate, for up to 10Hz Poisson spike trains (figure 1.8(left)). Although, the accuracy remained above 90% for each of the three frequencies. We also plotted the average $\Delta F/F_0$ as a function of stimulation firing rate. We found that it increased monotonically as a function of firing rate (figure 1.8(right)).

We expected lower spike inference quality as the average spiking frequency increased. Since the fluorescence trace, in some sense, is a low pass filtered version of the spike train, a

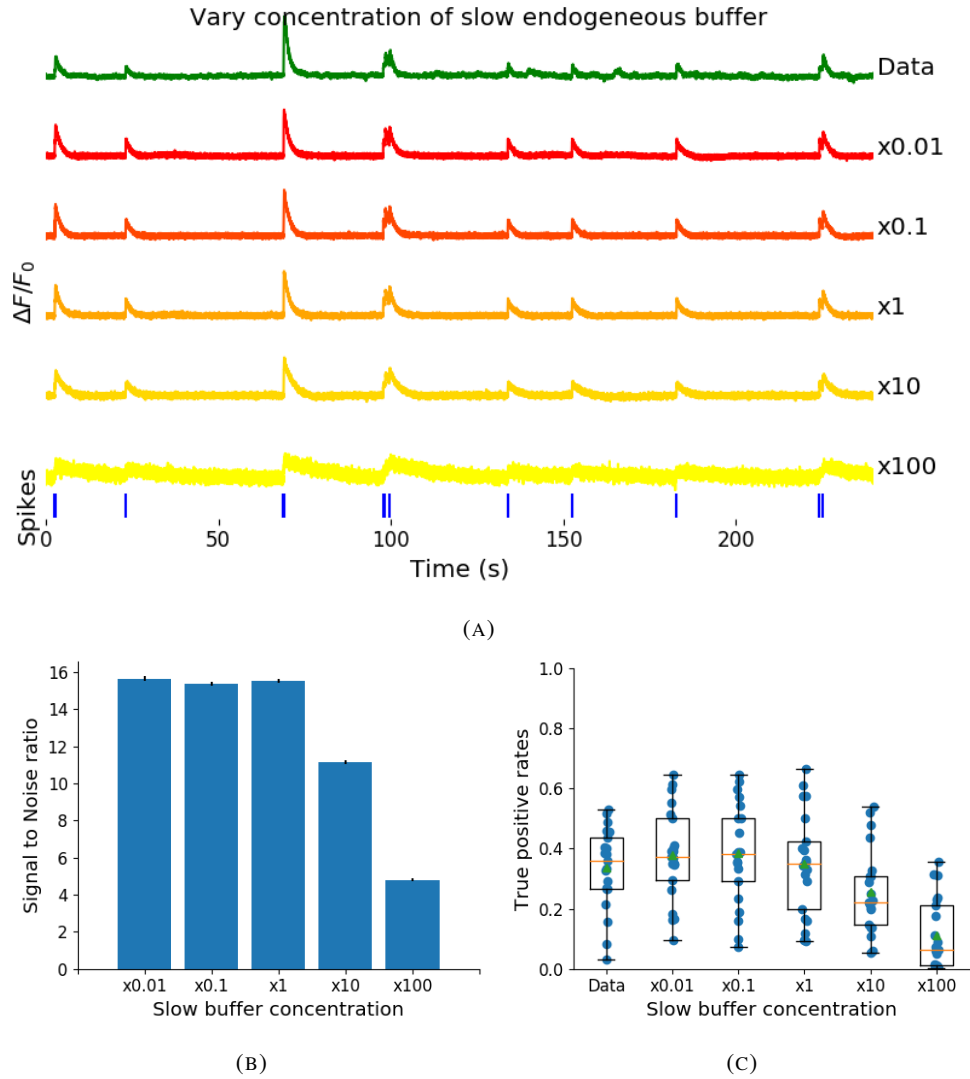


FIGURE 1.6: (a) An example trace for each of the five perturbed values for the concentration of immobile endogenous buffer. (b) The signal-to-noise ratio of the modelled fluorescence traces using each of the four perturbed values, and the experimental value. The lower values for the immobile buffer produce the same SNR as the experimental value. But the higher perturbed values produce fluorescence traces with a lower SNR. (c) The true-positive rates of the deconvolution algorithm's predictions when inferring from the observed data, and inferring from modelled traces using the perturbed and experimental values.

623 tightly packed groups of spikes will be more difficult to infer than isolated spikes. However,
 624 the increasing amplitude of the fluorescence trace with increasing frequency suggests that
 625 some spike inference algorithm could be developed based on this amplitude.

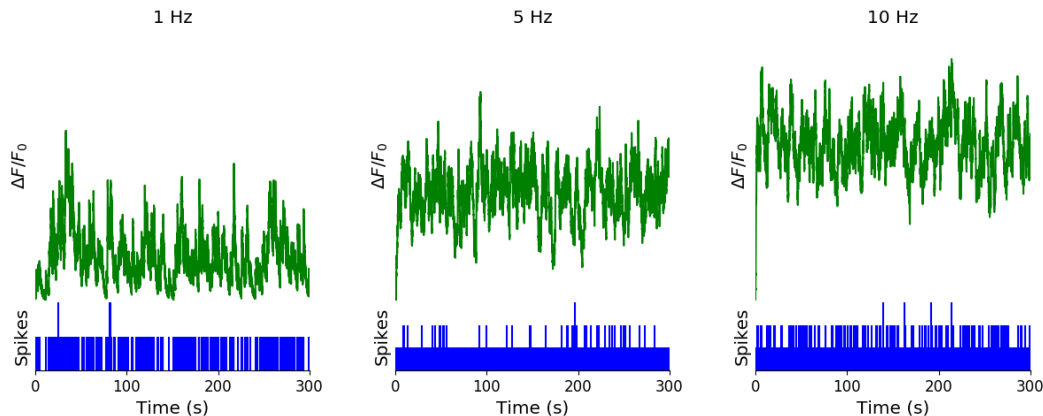


FIGURE 1.7: **Simulating fluorescence traces at different firing rates** Example modelled traces created using simulated spike trains with a mean firing rate of 1Hz (left column), 5Hz (middle column), and 10Hz (right column). Note the difference in amplitude with different mean firing rates.

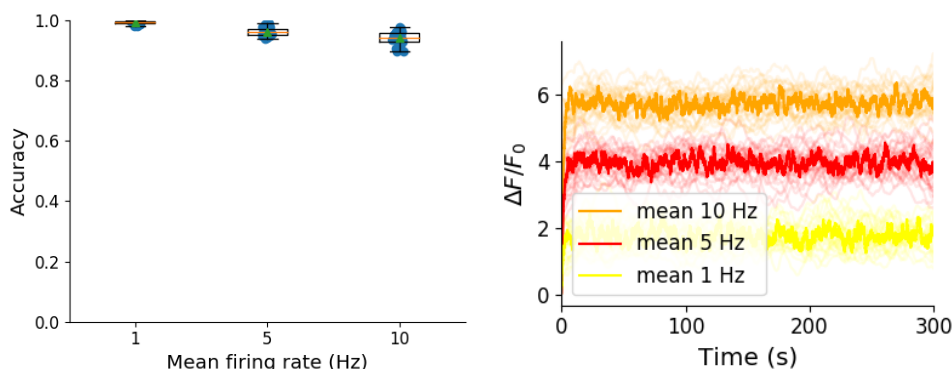


FIGURE 1.8: **Inference quality and $\Delta F/F_0$ vs Firing rate** (left) The spike inference accuracy when applied to 30 traces created using simulated spike trains with mean firing rates of 1, 5, and 10 Hz. (right) The mean $\Delta F/F_0$ across those 30 traces for each frequency.

626 1.3 Discussion

627 We designed a biophysical model for the changes in free calcium and bound calcium con-
 628 centrations within a cell soma with a fluorescent calcium indicator. We used this model to
 629 model the fluorescence trace resulting from a spike train in this cell. We fit the free parame-
 630 ters of the model by matching the power spectrum and amplitude of fluorescence traces with
 631 simultaneously measured spike trains. We inferred spikes from real fluorescence traces and

632 modelled fluorescence traces, and measured the quality of the spike inference in both cases.
633 We found that the spike inference quality was similar in both cases. We perturbed the concen-
634 tration of the calcium buffers in the model, and the binding/unbinding rates of those buffers
635 in the model, and measured the effect on the signal-to-noise ratio (SNR) of the modelled
636 fluorescence traces and the spike inference quality.

637 For the fluorescent calcium indicator, we found that any large perturbation away from
638 the experimental value led to a reduction in SNR, and spike inference quality. For the bind-
639 ing/unbinding rates, we kept the ratio of these rates constant, but altered their values in paral-
640 lel. The lower values caused a reduction in SNR, and a reduction in spike inference quality.
641 For the endogenous buffer concentration, an increase above the experimental value caused a
642 reduction in SNR and spike inference quality.

643 Although the model produced visually similar time series to the real data, there were a
644 few aspects it did not capture. First, the real data featured some low-frequency components
645 that did not appear related to the spike events. These were not captured by the models we
646 used in this study, but could be added in future by adding a suitable low-frequency term to the
647 resulting time series. Second, the real data seemed to have some nonlinearities not captured in
648 the model, for example the response to two nearby spikes was greater than expected from the
649 linear sum of two single spikes. This may be due to the co-operative binding of Calmodulin
650 to calcium, which gives calmodulin a supra-linear sensitivity to calcium concentration. The
651 model, in contrast behaved much more linearly, but could be extended in future to include
652 such nonlinearities. Third, in the real data the fluorescence peak amplitude seemed to vary
653 from spike to spike, even for well-isolated spike events. However in our model we assumed
654 each spike lead to the same fixed-amplitude injection of calcium to the cell, leading to much
655 greater regularity in fluorescence peak amplitudes. This variability could be added in future
656 versions of the model by making the injected calcium peak a random variable. Fourth, we
657 modelled the soma as a single compartment, but in reality there is likely a non-uniform spatial
658 profile of calcium concentration. This may matter because some endogenous buffers might
659 access calcium right as it influxes from the extracellular space, whereas the majority of the
660 fluorescence signal is more likely coming from the bulk of the cytoplasm. Future models
661 could attempt to model these spatial dependencies to assess whether they affect the overall
662 spike inference procedure.

663 As well as the optimised parameters, the model has 14 fixed parameters than can be
664 changed to simulate different types of calcium indicators. This model could be used to test
665 the theoretical performance of proposed new types of calcium indicator. The model could

also be used by developers of spike inference algorithms to test the effects of changing calcium indicator parameters on spike inference, or to test the affects of changing spiking characteristics on spike inference. For example, high firing rate vs low firing rate, or bursting vs no bursting. Given the increasing amplitude of the fluorescence trace with increasing mean firing rate, it would be possible to build a spike inference algorithm on this principle at least in part.

Our model has already been used as a tool by our colleagues, for simulating fluorescence traces in response to cells that can fire with a continuous rate between 10 and 20Hz, but do not always do so. Our colleagues found that a combination of the amplitude and the variance of the simulated fluorescence trace was the best indicator of firing rate. For example, when a cell was not firing, the amplitude and variance of the fluorescence trace was relatively low. When the cell fired with a low firing rate $\sim 1\text{Hz}$, the mean amplitude was still low but the variance of the fluorescence trace was high, and for high firing rate $\sim 10 - 20\text{Hz}$, the fluorescence amplitude was high, and the variance was low. In this way, our model may be useful for investigating firing rates underlying real fluorescence traces in response to cells which can fire in these rage ranges.

A recent paper by Greenberg et al (2018) described a biophysical model for spike train inference called the ‘Sequential binding model’. Similar to our model, this model included parameters for two types of endogenous buffer. But this model also included dynamics for calcium binding to and unbinding from these endogenous buffers. Furthermore, this model included dynamics for calcium binding to and unbinding from the four binding sites present on a GCaMPs6 molecule. In the accuracy measurements specified in that paper, this model performed better than the MLspike algorithm, which is also partially a biophysically model, and it performed better than the constrained non-negative deconvolution algorithm. The sequential binding model also biophysically interpretable parameters, and its fitted parameters for quantites such as buffering capacity and calcium influx upon action potential firing fall in line with experimental values (Greenberg et al., 2018). Biophysical models like this appear to be the way forward for spike inference algorithms.

1.4 Methods

1.4.1 Calcium dynamics model

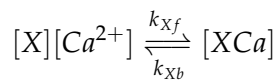
We wrote a biophysical model of the calcium dynamics within a cell soma. When a neuron fires an action potential, voltage-dependent calcium ion-channels open up that allow a

current of Ca^{2+} to flow into the neuron (Koch, 1999). The increase in the free calcium ion concentration inside of the cell, along with changes in the concentration of potassium and sodium, causes the change in cell membrane potential, which must be depolarised. The depolarising process consists of free calcium ions leaving the cell through open ion channels, or binding to molecules within the cell called buffers, or calcium storage by organelles such as the endoplasmic reticulum. A diagram illustrating the cell, its channels, and its buffers can be seen in figure 1.1A. There are several different types of calcium buffer, each with different dynamics and different concentrations within different types of excitable cell. The fluorescent calcium indicator is another calcium buffer, with the useful property that when it is bound to a calcium ion, the bound molecule may become excited by a photon and release a photon in return. This is what creates the fluorescence. After the action potential has taken place, the free calcium concentration within the cell will return to a baseline level (Maravall et al., 2000).

We modelled the the dynamics of five molecular concentrations,

- Free calcium ion concentration, $[\text{Ca}^{2+}]$
- Fluorescent indicator bound calcium, $[\text{BCa}]$
- Endogenous mobile buffer bound calcium, $[\text{ECa}]$
- Endogenous immobile buffer bound calcium, $[\text{ImCa}]$
- Excited buffered calcium, $[\text{BCa}^*]$

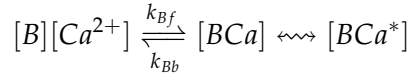
The term ‘buffering’ refers to free calcium ions coming into contact with buffer molecules and binding together. Diagrammatically:



where $[\text{X}]$ represents any buffer molecule, and k_{Xf} and k_{Xb} represent the binding and unbinding (dissociation) rates in units of per molar concentration per second ($\text{M}^{-1} \text{s}^{-1}$) and per second (s^{-1}) respectively. The speed of this chemical reaction is determined by the binding and unbinding rates.

There are a number different endogenous buffers in any neuron. Which buffers are present, and the buffers’ concentrations vary from cell to cell. In order to capture the effects of mobile and immobile endogenous buffers without introducing several parameters, they were modelled as two buffers. One representing mobile buffers and the other representing immobile buffers. Each with their own binding and unbinding rates.

The fluorescent calcium indicator behaves similarly to the other calcium buffers. The calcium is buffered by the indicator in the same way. But an indicator bound calcium molecule can become excited by absorbing the energy from a photon. An excited indicator bound calcium molecule can then release a photon to go back to its ‘relaxed’ state.



726 The released photons are captured by a photon collector. This gives us the fluorescence trace.

727 Ignoring the baseline level of free calcium in a neuron, the system of equations we used
728 to model all of these interactions is as follows:

$$\begin{aligned} \frac{d[Ca^{2+}]}{dt} = & k_{Bb}[BCa] + k_{Eb}[ECa] + k_{Imb}[ImCa] \\ & - k_{Bf}[B][Ca^{2+}] - k_{Ef}[E][Ca^{2+}] - k_{Imf}[Im][Ca^{2+}] \\ & + \beta([Ca_0^{2+}] - [Ca^{2+}]) \end{aligned} \quad (1.1)$$

$$\frac{d[BCa]}{dt} = k_{Bf}[B][Ca^{2+}] - k_{Bb}[BCa] + r[BCa^*] - e[BCa] \quad (1.2)$$

$$\frac{d[ECa]}{dt} = k_{Ef}[E][Ca^{2+}] - k_{Eb}[ECa] \quad (1.3)$$

$$\frac{d[ImCa]}{dt} = k_{Imf}[Im][Ca^{2+}] - k_{Imb}[ImCa] \quad (1.4)$$

$$\frac{d[BCa^*]}{dt} = \eta[BCa] - r[BCa^*] \quad (1.5)$$

729 where $[Ca_0^{2+}]$ is the baseline calcium concentration within the cell soma, β is a rate defining
730 how quickly free calcium enters or leaves the cell in the absence of an action potential, η
731 is the excitation rate for indicator bound calcium, r is the photon release rate for the excited
732 indicator bound calcium, and f and b are used to indicate the forward and backward rates
733 for chemical reactions respectively. The excitation rate defines the proportion of indicator
734 bound calcium that becomes excited at each time step. The photon release rate defines the
735 proportion of excited indicator bound calcium that releases a photon and returns to its relaxed
736 state at each time step. An action potential is modelled as a discontinuous increase in the free
737 calcium concentration to an appropriate value (Maravall et al., 2000).

738 Note that each of the three pairs of binding and unbinding terms in the first equation has a
739 corresponding pair in one of the subsequent three equations. Binding removes a free calcium
740 molecule and adds a bound calcium molecule, and unbinding does the opposite.

741 When using this model to simulate a fluorescence trace, the system of equations above are

first solved over a period of 25s without action potentials. This lets each of the five tracked chemical concentrations reach their steady state. Then we use the given spike train and the parameters to model the fluorescence trace.

Note that since the model has no spatial component, the mobile and immobile buffers only differ in their binding and unbinding rates.

Photon release & capture

We used a simple model for the photon release. The number of photons released at each time step was controlled by the number of excited indicator bound calcium molecules in the cell and a parameter called the ‘release rate’. The release rate is an optimised free parameter of the model.

As for the photon capture, in two-photon excitation microscopy the photons scattered by the fluorescent indicator get scattered in all directions. Therefore the number of photons detected is stochastic. This made the process for capturing photons the natural source of noise in the system. The number of photons captured, and therefore the intensity of the fluorescence, is modelled using a binomial distribution. The number of photons released was used as the number of trials. The probability of success, or ‘capture rate’ was a free parameter of the model that we optimised.

1.4.2 Parameter optimisation

The free parameters of the model are as follows:

Calcium rate, β Controls how quickly the concentration of free calcium will be driven to the baseline concentration.

Capture rate, p The average proportion of photons captured by the photon detector.

Excitation rate, η The number of indicator bound calcium molecules that become excited by photon bombardment at each time step.

Release rate, r The number of excited indicator bound calcium molecules that release a photon at each time step.

To optimise the free parameters given a fluorescence trace, we applied the following procedure:

1. The frequency power spectrum of the trace was measured.

- 771 2. The power spectrum was smoothed using a boxcar smoother (aka. sliding average, box
772 smoother).
- 773 3. The log of the smoothed power spectrum was measured.
- 774 4. Use the model to create a modelled fluorescence trace.
- 775 5. Apply steps 1, 2, and 3 to the modelled fluorescence trace.
- 776 6. Calculate the root mean squared difference between the log power of the actual fluo-
777 rescence trace, and the log power of the modelled fluorescence trace.
- 778 7. Calculate the root mean squared difference between the actual fluorescence trace and
779 the modelled fluorescence trace.
- 780 8. Use an optimisation algorithm to reapply this process, attempting to minimize the sum
781 of the two root mean squared differences at each iteration.

782 Using the root mean squared difference of the log power spectra as part of the objective
783 function forces the model to match the noise frequency of the actual fluorescence. Using
784 the root mean squared difference of the traces themselves forces the model to match the
785 amplitude of the fluorescence trace more accurately.

786 In order to minimise the objective function, a suite of meta-heuristic optimisation (aka.
787 black-box optimisation) algorithms were implemented on each of the traces in the dataset.
788 These methods were chosen because they don't require a gradient for the objective function
789 (gradient-free) and they are particularly useful for minimising stochastic objective functions
790 like the one we used here. The free parameters were optimised for each individual fluores-
791 cence trace. The most successful method for each trace was recorded. The method that was
792 most often successful was probabilistic descent, and the second most successful method was
793 generating set search. Both of these methods are examples of pattern search. These two
794 methods were the best optimisers on about 75% of the traces in the dataset.

795 Although this optimisation procedure minimises the value of the optimisation function,
796 the value never reaches zero for a number of reasons. Firstly, the fluorescence traces carry low
797 frequency fluctuations that cannot be captured by the model. Secondly, the model assumes
798 that the process of calcium binding to the fluorescent indicator is linear in time (see equation
799 1), but there are more complicated dynamics involved here. Fluorescent calcium indicators
800 are often built upon the calcium binding protein called 'calmodulin'. This protein has four
801 calcium binding sites. These sites are locally split into two pairs. Each pair has a different

Parameter	Description	Value	Source
baseline	The baseline concentration of free calcium within the cell soma	$4.5 \times 10^{-8}\text{M}$	(Maravall et al., 2000)
cell radius	The radius of the soma (assumed to be spherical)	10^{-5}M	(Fiala and Harris, 1999)
endogenous	The concentration of endogenous mobile buffer within the cell soma	10^{-4}M	(Faas et al., 2011)
frequency	The frequency at which the spike trains are sampled.	100Hz	
immobile	The concentration of endogenous immobile buffer within the cell soma	$7.87 \times 10^{-5}\text{M}$	(Bartol et al., 2015)
indicator	The concentration of fluorescent indicator within the cell soma	10^{-4}M	(Maravall et al., 2000)
k_{Bb}	The unbinding rate of the fluorescent calcium indicator	160s^{-1}	(Bartol et al., 2015)
k_{Bf}	The binding rate of the fluorescent calcium indicator	$7.77 \times 10^8\text{s}^{-1}\text{M}^{-1}$	(Bartol et al., 2015)
k_{Eb}	The unbinding rate of the endogenous mobile buffer	10^4s^{-1}	(Bartol et al., 2015)
k_{ef}	The binding rate of the endogenous mobile buffer	$10^8\text{s}^{-1}\text{M}^{-1}$	(Bartol et al., 2015)
k_{Imb}	The unbinding rate of the endogenous immobile buffer	524s^{-1}	(Bartol et al., 2015)
k_{Imf}	The binding rate of the endogenous immobile buffer	$2.47 \times 10^8\text{s}^{-1}\text{M}^{-1}$	(Bartol et al., 2015)
peak	The increase in free calcium concentration within the cell induced by an action potential	$2.9 \times 10^{-7}\text{M}$	(Maravall et al., 2000)

TABLE 1.1: **Fixed parameters** A table of the parameters fixed before optimising the model. The values of these parameters could be changed to model different fluorescent calcium indicators.

802 affinity for calcium, and the affinity of the binding sites is affected by the occupancy of
803 the other binding sites (Kilhoffer et al., 1992). So the calcium to calcium indicator binding
804 process is non-linear, but the model does not take this into account.

805 **Fixed parameters**

806 As well as the optimised parameters mentioned in section 1.4.2, the model also has thirteen
807 fixed parameters. Please see table 1.1 for details of these parameters and their values. In
808 an application of the model, these parameters can be changed in order to model any given
809 fluorescent calcium indicator.

810 1.4.3 Julia

811 The programming language used to write and execute the model was ‘Julia’. Julia is a dynamic programming language designed for technical computing. Julia was designed specifically to provide a convenient high-level dynamic language similar to MATLAB, or Python, with improved performance. Julia’s type system and Julia’s direct interfaces with C and Fortran allow this aim to be achieved (Bezanson et al., 2012). The Julia version of the ‘Sundials’ package for ODE solving was used to solve the system of equations above. The BlackBoxOptim.jl package for Julia was used to perform the optimisation.

818 1.4.4 Spike inference

819 We used spike inference algorithms to compare the quality of spike inference using the modelled traces to the quality of spike inference using the observed traces. We also used the spike inference algorithms to assess the effect of parameter perturbation on the spike inference. Three algorithms were used:

823 **Constrained non-negative deconvolution algorithm (aka Pnevmatikakis algorithm)** This algorithm uses a constrained version of non-negative Weiner deconvolution to infer a calcium signal and a ‘spiking activity signal’ from the fluorescence trace (Vogelstein et al., 2010; Pnevmatikakis et al., 2016). The spiking activity signal is a non-negative vector of real numbers reflecting the cell’s activity rather than an actual spike train. We inferred a spike train by choosing an optimised threshold for the spiking activity signal. Whenever the spiking activity signal exceeded that threshold, an action potential was inferred. The threshold was optimised by minimising the difference between the number of spikes observed and the number of spikes predicted.

832 **ML-Spike algorithm** This algorithm uses a generalised version of the Viterbi algorithm to return the spike train that maximises the likelihood of producing the given fluorescence trace. The Viterbi algorithm is an algorithm for estimating the most likely sequence of hidden states resulting in a sequence of observed states in a discrete-time finite-state Markov process (forney). In this case, each hidden state is defined by the presence or absence of an action potential, and each observed state is the value of the fluorescence trace at each time step. This algorithm assumes that the concentration of calcium within the cell will decay to a drifting baseline, rather than a fixed baseline (Deneux et al., 2016).

Online Active Set method to Infer Spikes (OASIS) This algorithm is once again based on an auto-regressive model of the fluorescence trace, but can be generalised to any order. The algorithm itself is a generalisation of the pool adjacent violators algorithm (PAVA) that is used in isotonic regression. The OASIS algorithm works through the fluorescence trace from beginning to end, this combined with the speed of the algorithm means that it could be used for real-time online spike inference (Friedrich and Paninski, 2016). Given a fluorescence trace, the algorithm will return the most likely spike train and an inferred denoised fluorescence signal.

In order to quantify the quality of spike inference for a given algorithm, we ran that algorithm on all of the fluorescence traces in dataset number eight of the spike finder datasets. Then we measured some binary classification measures on the results. These measures included

- Accuracy
- True positive rate (aka recall, sensitivity, hit rate)
- True negative rate (aka specificity)
- Precision
- Negative predicted value
- False negative rate (aka miss rate)
- False positive rate (aka fall-out)
- False discovery rate
- False omission rate

In making these measurements, we allowed a tolerance of two subsequent time bins for spike prediction. For example, the spike train data is a vector of 0s and 1s, with one element for each time bin. A ‘0’ denotes inactivity, a ‘1’ denotes the presence of at least one action potential. The inferred spike trains produced by the spike inference algorithms take the same form. In our analysis, if a spike appeared in the inferred spike train up to two time frames after a spike in the observed spike train, that spike was considered correctly inferred i.e. a true positive. However, once a spike in the inferred spike train was matched to a spike from the observed spike train, the inferred spike could not be matched to another observed spike. To illustrate, if two spikes were inferred in the two time bins following an isolated observed

spike, the first inferred spike was considered correctly inferred, but the second inferred spike was considered incorrectly inferred, i.e. a false positive.

The most useful measure was the true positive rate. This is because the spiking is sparse and this measurement is sensitive to the number of spikes observed and inferred, but is not affected by the true negative or false negative rates. After optimising the parameters for each fluorescence trace we measured the spike inference quality for the observed fluorescence traces, and compared this to the spike inference quality for the modelled traces.

When measuring the spike inference quality for higher frequency spike train (1 – 10Hz), we used the accuracy as our binary classification measure. At these frequencies the variance of the fluorescence trace was much higher than for sparser spiking regimes, therefore we wanted to take into account the number of false negatives inferred by the algorithm.

Comparing spike inference quality

In order to compare spike inference quality we had to use methods for comparing samples. When comparing the true positive rate distributions arising from two different datasets, or two different algorithms on the same dataset, we compared the distributions using a paired t-test.

1.4.5 Perturbation analysis

In order to measure the sensitivity of spike inference to changes in a given model parameter, we perturbed the parameter and compared the quality of spike inference with the perturbed parameters to the quality of spike inference with the experimental or optimised parameters. In order to maximise the possibility of observing a difference due to the perturbation, we perturbed the chosen parameter by a relatively large amount. For example, the experimental value for the molar concentration of the fluorescent indicator within the cell was 10^{-4}M (Maravall et al., 2000). The perturbed values used for this parameter were 10^{-2}M , 10^{-3}M , 10^{-5}M , and 10^{-6}M . The quality of the inference was compared by measuring the true positive rate for each perturbed value and using a t-test to compare the distributions of the results.

This analysis was performed firstly without any optimisation of the free parameters for use with the perturbed parameters. Then the analysis was performed after the optimised parameters for each perturbed value were calculated.

899 **1.4.6 Signal-to-noise ratio**

900 To assess the effect of perturbation on the modelled traces, we measured and compared the
901 signal to noise ratio (SNR) on each of the modelled traces. We calculated the SNR as the
902 peak change in fluorescence divided by the standard deviation of the baseline fluctuation of
903 the fluorescence trace (Tada et al., 2014). We measured these values by running the model
904 on a spike train consisting a long period of inactivity followed by one action potential. We
905 ran the model on this spike train one hundred times. We then measured the mean change
906 in fluorescence and standard deviation of baseline activity across the one hundred modelled
907 fluorescence traces, and calculated the SNR.

908 **1.4.7 Data sources**

909 All of the data used in this project was sourced from the ‘Spike Finder’ project (spikefinder.codeneuro.org).
910 The data consisted of a collection of datasets with simultaneously measured fluorescence
911 traces and action potentials (Berens et al., 2018).

Chapter 2

**Functional networks expand across
anatomical boundaries as correlation
time-scale increases**

UNIVERSITY OF BRISTOL

Abstract

Engineering

Department of Computer Science

Doctor of Philosophy

Investigating, implementing, and creating methods for analysing large neuronal ensembles

by Thomas J. DELANEY

Decades of research has established that correlated spiking plays a crucial role in representing sensory information. One drawback associated with the recent improvement in recording technology and consequent large datasets is the difficulty in analysing higher order correlations in large neuronal ensembles. One benefit of these datasets that has not yet been explored is the opportunity to compare correlations within anatomical regions to correlations across anatomical regions. In this work, we measured correlations between neurons residing in nine different brain regions in three awake and behaving mice. Using these correlation measurements, we created weighted undirected graph networks and applied network science methods to detect functional communities in our neural ensembles. We compared these functional communities to their anatomical distribution. We repeated the analysis, using different timescales for our correlation measurements, and found that functional communities were more likely to be dominated by neurons from a single brain region at shorter timescales ($< 100\text{ms}$).

2.1 Introduction

Decades of research has established that correlations play a crucial role in representing sensory information. For example, the onset of visual attention has been shown to have a greater affect on the correlations in the macaque V4 region than on the firing rates in that region (Cohen and Maunsell, 2009). Recent findings show that spontaneous behaviours explain correlations in parts of the brain not associated with motor control (Stringer et al., 2019), that satiety state appears to have a brain wide representation (Allen et al., 2019), and that subject exploratory and nonexploratory states are represented in the amygdala (Gründemann et al., 2019). So, behavioural states are likely represented across many regions of the brain, not just motor related areas. In order to understand the brain, we must understand the interactions between neurons and regions.

Because of limitations in recording technology almost all research has explored correlations between neurons within a given brain region, or within only two regions at most (Wierzynski et al., 2009; Patterson et al., 2014; Girard, Hupé, and Bullier, 2001). Relatively little is known about correlations between neurons in many different brain regions. However, the recent development of ‘Neuropixels’ probes (Jun et al., 2017) has allowed extracellular voltage measurements to be collected from multiple brain regions simultaneously routinely, and in much larger numbers than traditional methods. In this project we used a publicly-available Neuropixels dataset to analyse correlations between different brain regions (Stringer et al., 2019).

A drawback associated with the improvement in recording technology is an increase in the difficulty in analysing these data. For example, analysing the i th order interactions of N neurons generally requires estimation of N^i parameters. A number that becomes astronomical for large N . New methods are required for analysing these new large datasets. We attempted to address this requirement in this piece of research by applying a cutting-edge network science community detection method to neural data.

Another unexplored area of research is the changes in cell interactions at different timescales. Studies have shown different timescales for fluctuations in spiking activity (Murray et al., 2014), and different time scales for event representation (Baldassano et al., 2017) across different brain regions. Still most studies focus on quantifying interactions at a given timescale. But neurons may interact differently, or may interact with different neurons at different timescales. Here we explore correlated communities of neurons at different timescales.

In this work, we measured correlations between binned spike counts from neurons from

nine different regions of the mouse brain. These measurements induced a weighted undirected graph or network where each neuron is represented by a node, and the strength of the connection between these nodes/neurons is the strength of the correlation between their spike counts. We then applied newly invented network methods (Humphries et al., 2019) to this network to find any community structure, and place the neurons in these correlation based communities. Finally, we compared these functional communities to the anatomical membership of the neurons.

To investigate the functional communities and their relationship with anatomy at different time scales, we repeated these analyses using different length bin widths when binning spike times.

To find and analyse functional networks while controlling for the subject's behaviour, we conditioned the binned spike counts on data from a video of the subject's face, and repeated our analysis for spike count correlations (or noise correlations) and signal correlations.

2.2 Results

Note that in the following text, we refer to the correlation coefficient between two sequences of spike counts from two different cells as the *total correlation*. We refer to the correlation between spike counts in response to a certain stimulus as the *spike count correlation* aka *noise correlation*, and we refer to the correlation between mean or expected responses to different stimuli as the *signal correlation* (Cohen and Kohn, 2011).

The nine different brain regions from which we had data were the caudate putamen (CP), frontal motor cortex (FrMoCtx), hippocampus (HPF), lateral septum (LS), midbrain (MB), primary visual cortex (V1), superior colliculus (SC), somatomotor cortex (SomMoCtx), and thalamus (TH).

2.2.1 Average correlation size increases with increasing time bin width

First we inspected the affect of time bin width on total correlations. We know that using short time bins results in artificially small correlation measurements (Cohen and Kohn, 2011), so we expected to see an increase in correlation amplitude with increasing time bin width. That is exactly what we observed. Taking 50 cells at random, we calculated the total correlation between every possible pair of these cells, using different time bin widths ranging from 0.005s to 3s. We found that the longer the time bin width, the greater the correlations (see figure 2.2a).

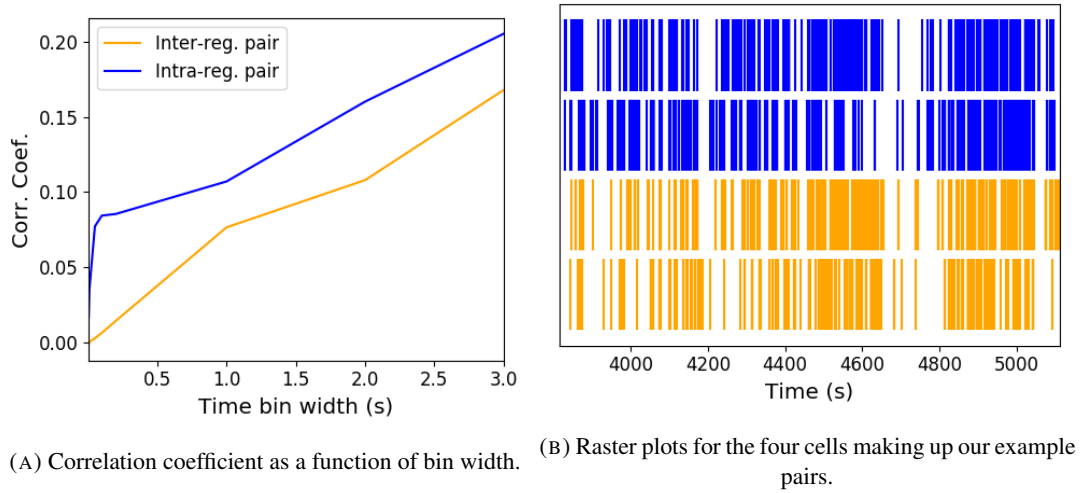


FIGURE 2.1: (A) An example of the correlation coefficients between two different pairs of cells, one where both cells are in the same brain region (intra-regional pair), and one where both cells are in different brain regions (inter-regional pair). The correlation coefficients have been measured using different time bin widths, ranging from 5ms to 3s. Note the increasing amplitude of the correlations with increasing bin width. (B) A raster plot showing the spike times of each pair of cells.

We also separated the positively correlated pairs from the negatively correlated pairs using the mean correlation of each pair across all bin widths (see section 2.5.2). We found that the positively correlated pairs become more positively correlated with increasing time bin width, and the negatively correlated pairs become more negatively correlated with increasing time bin width (see figures 2.2b and 2.2c).

In figure 2.1a we plot correlations from two example pairs, one pair from within a region, and one pair between regions. It can be seen that the correlation coefficient increases with bin width. The correlations can be observed by eye in the raster plot for these cells in figure 2.1b.

When taking the mean across all pairs, the positively correlated pairs dominate in terms of both number of pairs, and amplitude of correlations. Therefore the mean across all pairs is positive.

These results were observed in each of the three mouse subjects from which we had data.

2.2.2 Goodness-of-fit for Poisson and Gaussian distributions across increasing time bin widths

We wanted to investigate if the width of the time bin used to bin spike times into spike counts had an effect on the distribution of spike counts. We used the χ^2 statistic as a goodness-of-fit measure for Poisson and Gaussian (normal) distributions to the spike count of 100 randomly

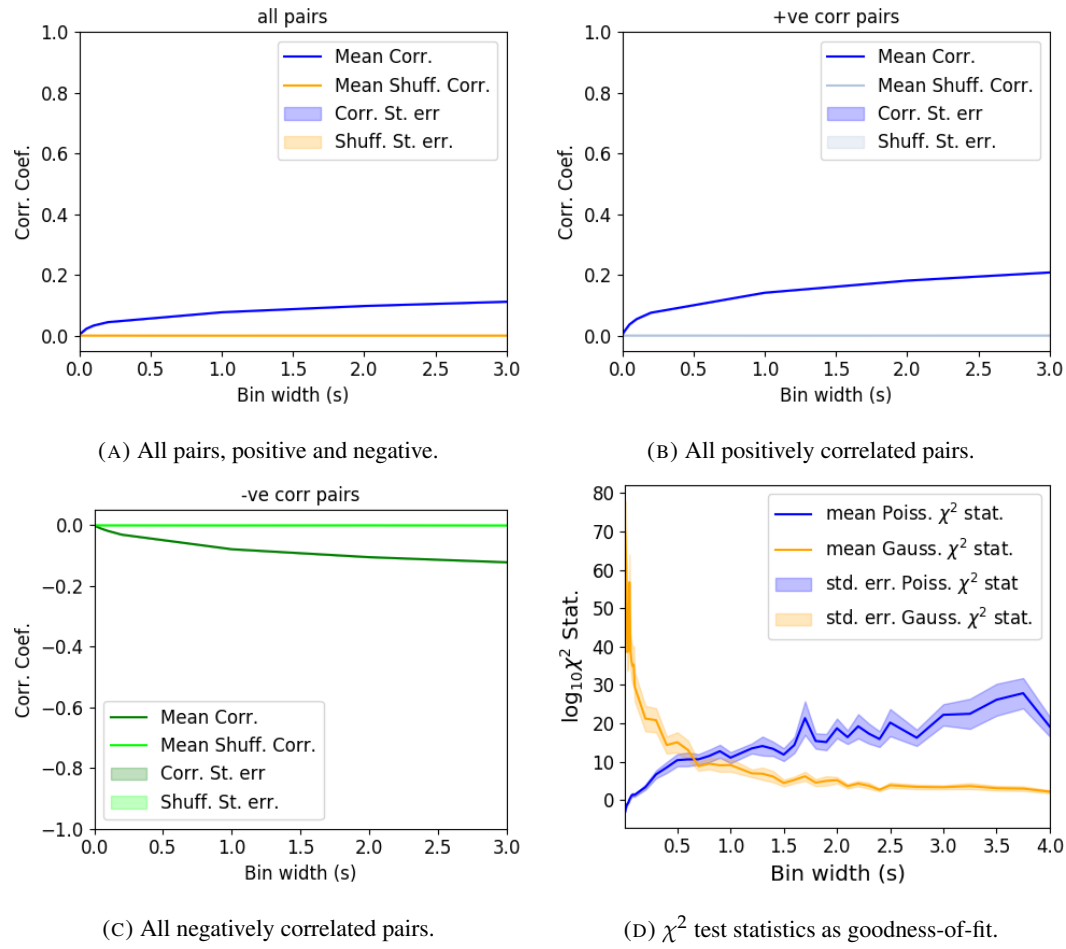


FIGURE 2.2: Mean correlation coefficients measured from pairs of 50 randomly chosen neurons. (A) All possible pairs, (B) positively correlated pairs, and (C) negatively correlated pairs. (D) Mean and standard error of χ^2 test statistics for Poisson and Gaussian distributions fitted to neuron spike counts.

1019 chosen neurons for a number of bin widths ranging from 0.01s to 4s. For the χ^2 statistic, the
1020 higher the value, the worse the fit.

1021 We expected a Poisson distribution to be a better fit for shorter time bin widths because
1022 spike counts must be non-negative, therefore any distribution of spike counts with mass dis-
1023 tributed at or close to 0 will be skewed. The distribution of spike counts is more likely to be
1024 distributed close to 0 when the time bin widths used to bin spike times into spike counts are
1025 small relative to the amount of time it takes for a neuron to fire an action potential (~ 1 ms in
1026 the case of non-burst firing neurons).

1027 We expected a Gaussian distribution to be a better fit for longer time bin widths, because
1028 a Poisson distribution with a large rate is well approximated by a Gaussian distribution with
1029 mean and variance equal to the Poisson rate. Therefore, a Gaussian distribution would ap-
1030 proximate the mean of a collection of large spike counts, and have more flexibility than a
1031 Poisson distribution to fit the variance.

1032 We found that that a Poisson distribution is the best fit for shorter time bins less than 0.7s
1033 in length. Then a Gaussian distribution is a better fit for time bins greater than 0.7s in length
1034 (see figure 2.2d).

1035 **2.2.3 Differences between and inter- and intra- regional correlations decrease** 1036 **with increasing bin width**

1037 We investigated the differences in distribution between inter-regional correlations, i.e. corre-
1038 lations between neurons in different brain regions, and intra-regional correlations, i.e. corre-
1039 lations between neurons in the same brain region.

1040 Firstly, we investigated these quantities for all possible pairs of ~ 500 neurons taken
1041 from across all the 9 brain regions from which we had data. We distributed these neurons as
1042 evenly as possible across all of the regions, so that cells from one region would not dominate
1043 our data. We observed that the mean intra-regional correlations were always higher than the
1044 mean inter-regional correlations for every value of time bin width used. We also observed
1045 that as the time bin width increased these mean correlations increased and the difference
1046 between the mean inter-regional and intra-regional correlations grew (see figure 2.3 (Left)).

1047 Stringer et al. (2019) had a similar finding using the same data. They used only one value
1048 for the time bin width, 1.2s. Using this time bin width to bin spike times and measure total
1049 correlations, they found that the mean ‘within-region’ correlations were always greater than
1050 the ‘out-of-region’ correlations (Stringer et al., 2019). The figure from thier paper showing
1051 this result can be seen in figure 2.3 (Right).

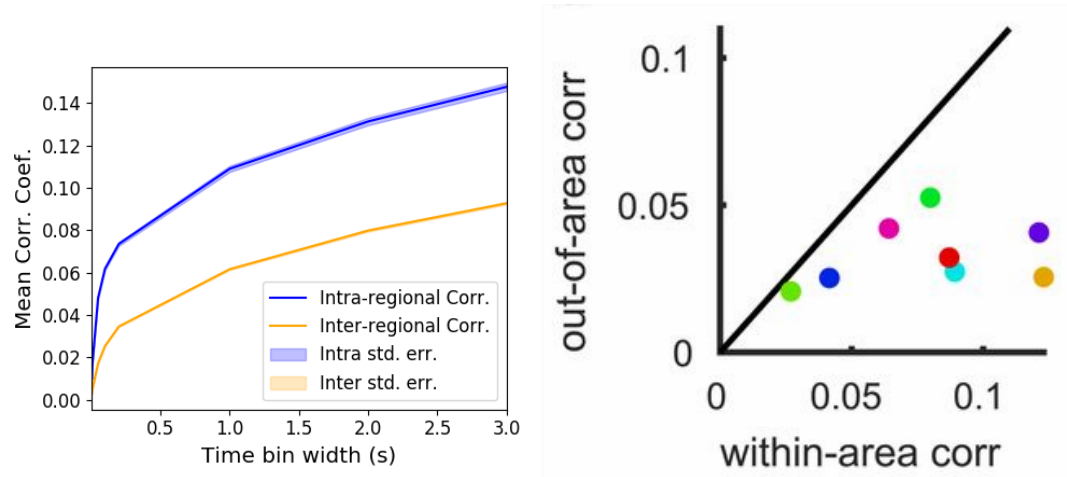


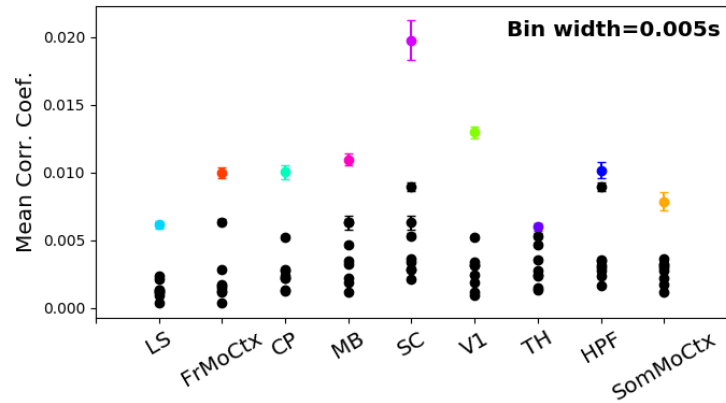
FIGURE 2.3: (Left) The mean intra-region and inter-region correlations using all possible pairs of ~ 500 neurons, spread across 9 different brain regions. (Right) Courtesy of Stringer et al. (2019), mean inter-regional (out-of-area) correlation coefficients vs mean intra-regional (within-area) correlation coefficients for a bin width of 1.2s. Note that the intra-regional coefficients are higher in each case.

Examples of the correlations of one intra-regional pair and one inter-regional pair can be seen in figure 2.1.

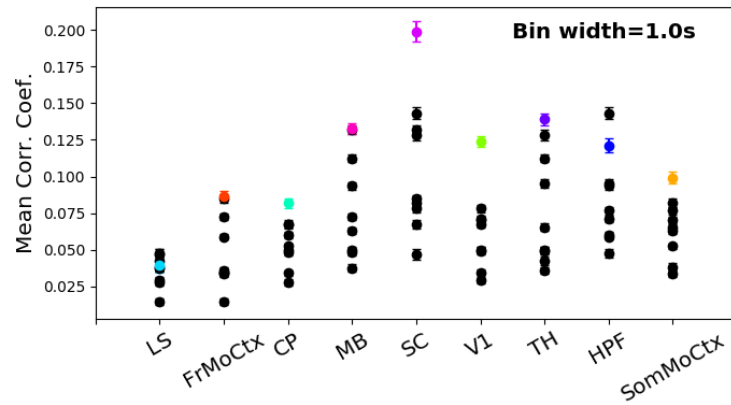
Secondly, we separated those pairs into intra-regional and inter-regional groups. We noted that the mean intra-regional correlations (coloured dots in figures 2.4a and 2.4b) for a given region tended to be higher than the mean inter-regional correlations (black dots in figures 2.4a and 2.4b) involving cells from that region. However, in contrast with our previous result, we noted that the difference between the mean intra-regional correlations and most highly correlated inter-regional correlations reduced as we increased the time bin width (see figures 2.4a and 2.4b). This shows that the mean correlations shown in figure 2.3 are not distributed evenly across all region pair combinations.

Finally, to see these regional mean correlations in a bit more detail, to examine the individual pair combinations in particular, we displayed these data in a matrix of mean correlations (see figure 2.5), showing the mean intra-regional correlations on the main diagonal, and the mean inter-regional correlations off diagonal. Comparing a version of this figure created using a short time bin width of 5ms (figure 2.5a) and a version using a longer time bin width of 1s (figure 2.5b) we observed that the mean intra-regional correlations are always relatively high in comparison to the mean inter-regional correlations, but the mean correlations in some inter-regional pairs are relatively much higher when using the longer time bin width.

This could indicate information being processed quickly at a local or within-region level, and the local representations of this information spreading between regions at longer timescales.



(A) Mean inter-regional and intra-regional correlations using a time bin width of 5ms.



(B) Mean inter-regional and intra-regional correlations using a time bin width of 1s.

FIGURE 2.4: The mean intra-regional correlations (coloured dots) and mean inter-regional correlations (black dots) for a given region, indicated on the x-axis, for different time bin widths. Each black dot represents the mean inter-regional correlations between the region indicated on the x-axis and one other region. (A) shows these measurements when we used a time bin width of 5ms. (B) shows these measurements when we used a time bin width of 1s. Note that the difference between the mean inter-regional correlations and mean intra-regional correlations is smaller for 1s bins.

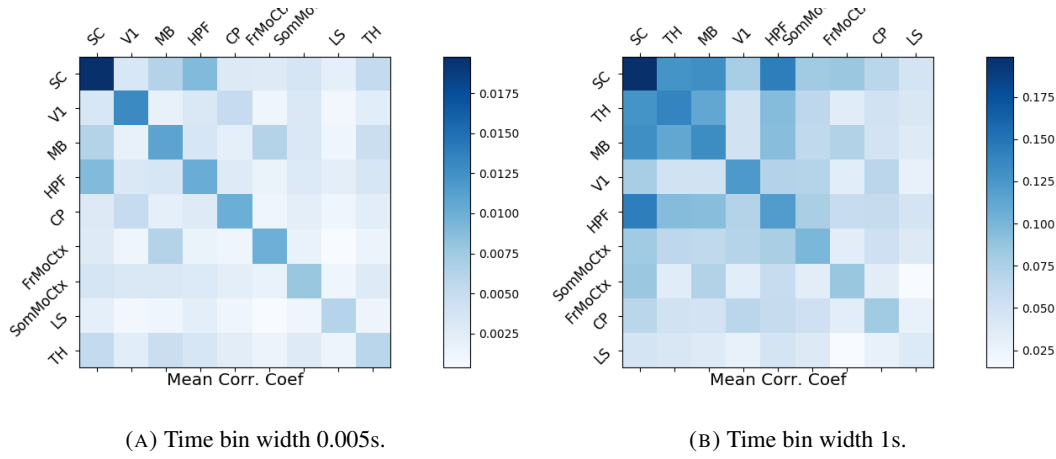


FIGURE 2.5: Mean inter-regional (main diagonal) and intra-regional (off diagonal) correlation coefficients. (a) Shows these measurements when spike times were binned using 5ms time bins. (b) Shows the same, using 1s time bins. Note that the matrices are ordered according to the main diagonal values, therefore the ordering is different in each subfigure.

These results were consistent across the three mouse subjects. But, the relative magnitudes of the mean intra-regional and inter-regional correlations were not consistent. For example, the region with the highest mean intra-regional correlations when using 1s bin widths for subject one is the superior colliculus (SC), but for subject two it is the midbrain (MB).

2.2.4 Connected and divided structure in correlation based networks reduces in dimension with increasing bin width

We used the correlation measurements to create weighted undirected graphs/networks where each node represents a neuron, and the weight of each edge is the pairwise correlation between those neurons represented by the nodes at either end of that edge. We aimed to find communities of neurons within these networks, and compare the structure of these communities to the anatomical division of those neurons. The first step of this process involved applying the ‘spectral rejection’ technique developed by Humphries et al (2019) (Humphries et al., 2019). This technique compares our data network to a chosen null network model, and finds any additional structure in the data network beyond that which is captured in the null network model (if there is any such structure).

By comparing the eigenspectrum of the data network to the eigenspectrum of many samples from the null network model, this technique allows us to estimate the dimensionality of the additional structure in the data network, and gives us a basis for that vector space. It also divides the additional structure into connected structure, and k -partite (or divided) structure. For example, if our algorithm found two dimensions of additional connected structure, and

one dimension of additional divided structure. We might expect to find three communities, that is groups more strongly connected within group than without, and we might expect to find bi-partite structure, that is two sets that are more strongly connected between groups than within groups.

The technique also finds which nodes contribute to this additional structure, and divides our data network into signal and noise networks. The details of spectral rejection and node rejection can be found in sections 2.5.5 and 2.5.5 respectively, and a full overview can be found in (Humphries et al., 2019).

We chose the sparse weighted configuration model (see section 2.5.5) as our null network model. This model matches the sparsity and the total weight of the original network but distributes the weight at random across the sparse network.

We applied the spectral rejection method to our networks based on total correlations using different values for the time bin width. We observed that for smaller time bin widths, our data networks had both k -partite structure, and community structure. As the width of the time bin increased, we found that the k -partite structure disappeared from our data networks, and the dimension of the community structure reduced in two of the three mice from which we had data (see figure 2.6).

2.2.5 Detecting communities in correlation based networks

We applied the community detection procedure described in section 2.5.5 to our signal networks for our various time bin widths. We detected a greater number of smaller communities at shorter time bin widths, and a smaller number of larger communities for longer time bin widths (see figure 2.7). This was expected after the results found in section 2.2.4. We found more dimensions of additional structure at shorter time bin widths, therefore we found more communities at shorter time bin widths.

We also noticed that at short time bin widths the communities detected tended to be dominated by cells from one region. Whereas communities existing in networks created using wider time bin widths tended to contain cells from many different brain regions. More on this in the next section.

2.2.6 Functional communities resemble anatomical division at short timescales

In order to quantify the similarity of the communities detected to the anatomical division of the cells. We treated both the anatomical division and the communities as clusterings of these cells. We then used measures for quantifying the difference or similarity between clusterings

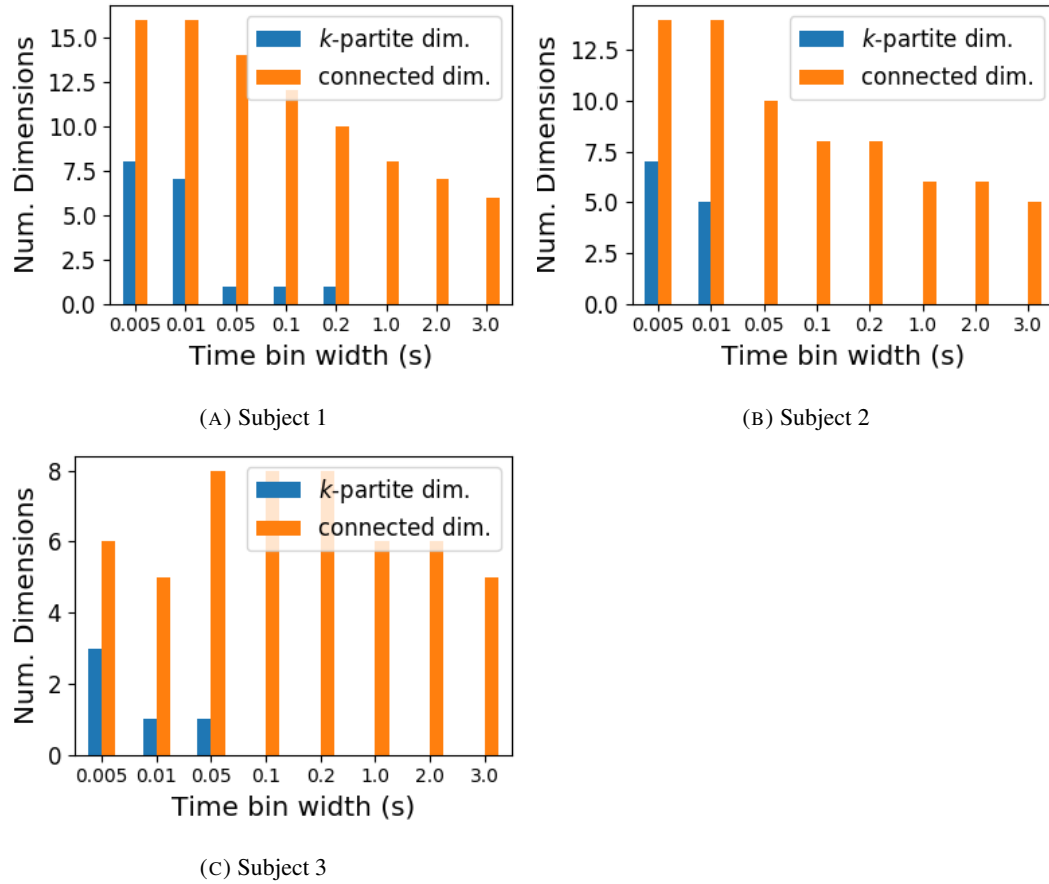


FIGURE 2.6: The number of dimensions in the k -partite and connected structure in the correlation based networks beyond the structure captured by a sparse weighted configuration null network model (see section 2.5.5), shown for different time bin widths. Note that the k -partite structure disappears for time bin width greater than 200ms for all three subjects. The dimension of the connected structure reduces with increasing bin width for 2 of the 3 subjects (top row).

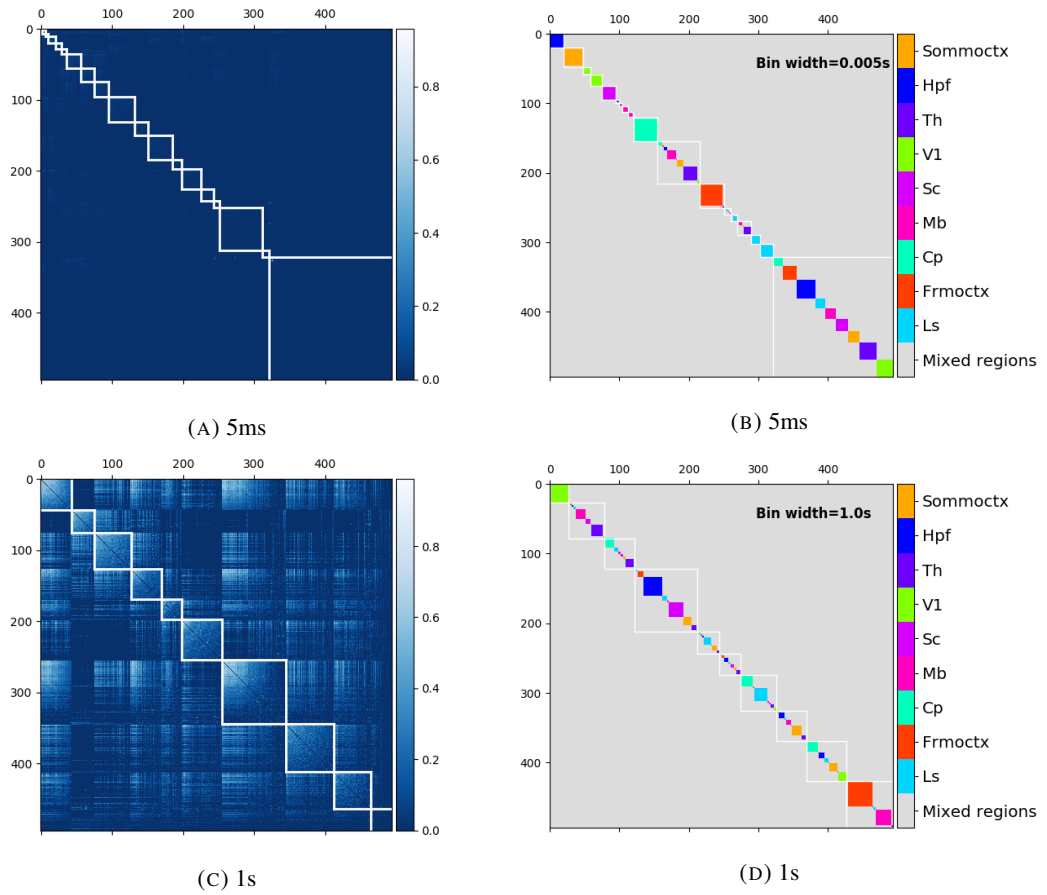


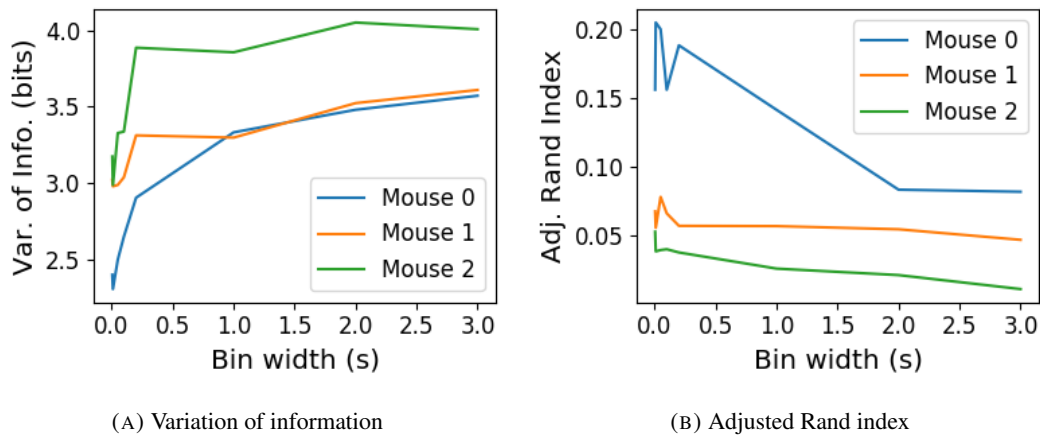
FIGURE 2.7: (A) and (C) Correlation matrices with detected communities indicated by white lines. Each off main diagonal entry in the matrix represents a pair of neurons. Those entries within a white square indicate that both of neurons are in the same community as detected by our community detection procedure. Matrices shown are for 5ms and 1s time bin widths respectively. (B) and (D) Matrices showing the anatomical distribution of pairs along with their community membership. Entries where both cells are in the same region are given a colour indicated on the colour bar. Entries where cells are in different regions are given the grey colour also indicated on the colour bar.

to quantify the difference or similarity between the detected communities and the anatomical division. Details of these measures can be found in section 2.5.6 or in (Vinh, Epps, and Bailey, 2010).

We used two different types of measures for clustering comparison; information based measures (see section 2.5.6) and pair counting based measures (see section 2.5.6). We include one example of each in figure 2.8.

The variation of information is the information based measure included in figure 2.8a. This measure forms a metric on the space of clusterings. The larger the value for the variation of information, the more different the clusterings.

The adjusted Rand index is the pair counting based measure included in figure 2.8b. In contrast with the variation of information, the adjusted Rand index is a normalised similarity measure. The adjusted Rand index takes value 1 when the clusterings are identical, and takes value 0 when the clusterings are no more similar than chance.



(A) Variation of information

(B) Adjusted Rand index

FIGURE 2.8: (a) The variation of information is a measure of distance between clusterings. The distance between the anatomical ‘clustering’ and community detection ‘clustering’ increases with increasing time bin width. (b) The adjusted Rand index is a normalised similarity measure between clusterings. The anatomical and community detection clusterings become less similar as the time bin width increases.

Both measures indicated that the detected communities and the anatomical division of the cells were more similar when we used shorter time bins widths (see figure 2.8). This indicates that correlated behaviour in neuronal ensembles is more restricted to individual brain regions at short timescales ($< 250\text{ms}$), and the correlated activity spreads out across brain regions over longer time scales.

2.2.7 Conditional correlations & signal correlations

In light of the excellent research of Stringer et al (2019) showing that spontaneous behaviours can drive activity in neuronal ensembles across the visual cortex and midbrain (Stringer et al., 2019), we decided to control for the mouse’s behaviour when performing our analyses. It is possible that our community detection process may be detecting communities across multiple brain regions at longer time scales due to aggregating neuronal activity driven by several spontaneous behaviours occurring during the time interval covered by a given time bin. A time bin of 1s, for example, could contain a spike count where those spikes were driven by different spontaneous behaviours. We aimed to investigate this possibility by applying our community detection analysis to conditional correlation measures.

We used the top 500 principal components of a video of the mouse’s face as a measure of the mouse’s behaviour (see section 2.4.2). We modelled the spike counts as a linear combination of the principal components using linear regression with ElasticNet regularisation (see section 2.5.3). Using this model, we quantified the expected spike count given the mouse’s behaviour $E[X|Z_1, \dots, Z_{500}]$.

We used these expected values to measure $\text{cov}(E[X|Z], E[Y|Z])$, and we used that value, the covariance $\text{cov}(X, Y)$, and the *law of total covariance* (see section 2.5.3) to measure $E[\text{cov}(X, Y|Z)]$. Here X and Y represent spike counts from individual cells, and Z is shorthand for the 500 principal components mentioned above. The two components of the covariance, $\text{cov}(E[X|Z], E[Y|Z])$ and $E[\text{cov}(X, Y|Z)]$, represent a ‘signal covariance’ and expected value of a ‘spike count covariance’ respectively, analogous to the signal correlation and spike count correlation (Cohen and Kohn, 2011).

We examined the means of these components for different values of the time bin width (see figure 2.9). We observed a consistent increase in $E[\text{cov}(X, Y|Z)]$ as the time bin width increased. But we saw different trends for $\text{cov}(E[X|Z], E[Y|Z])$ for each mouse.

Using $\text{cov}(E[X|Z], E[Y|Z])$ we measured the signal correlation, ρ_{signal} , and using $E[\text{cov}(X, Y|Z)]$ we measured the event conditional correlation, $\rho_{X,Y|Z}$ (see section 2.5.3 for more details). We saw a consistent increase in $\rho_{X,Y|Z}$ as the time bin width increased, this corresponds to the result for $E[\text{cov}(X, Y|Z)]$. We observed different trends for ρ_{signal} for each mouse, this corresponds to the result for $\text{cov}(E[X|Z], E[Y|Z])$.

We applied our network noise rejection and community detection process to networks based on the spike count correlations $\rho_{X,Y|Z}$ and the signal correlations ρ_{signal} . We noted that the community detection on $\rho_{X,Y|Z}$ behaved similarly to the community detection on the total correlation. We can see this in figures 2.11a and 2.11b. At very short time bin widths, we

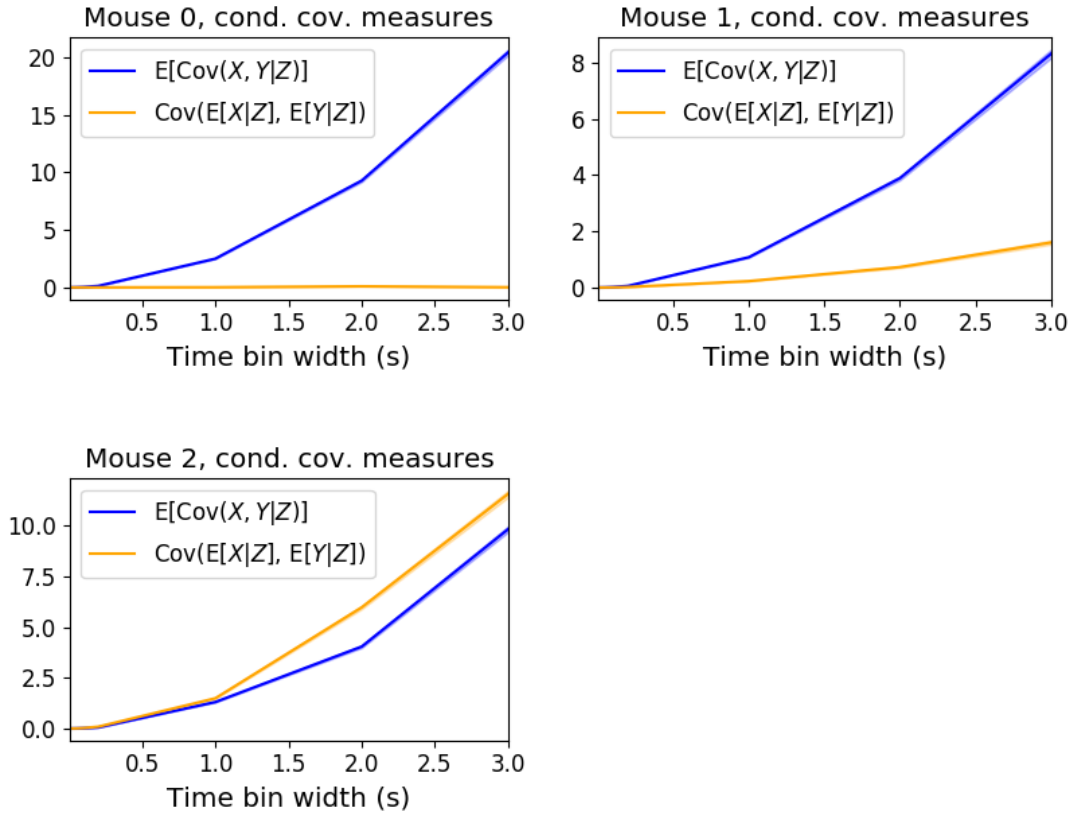


FIGURE 2.9: Comparing the components of the spike count covariance across different values for the time bin width. We observed a consistent increase in $E[\text{cov}(X, Y|Z)]$ as the time bin width increased. But we saw different trends for $\text{cov}(E[X|Z], E[Y|Z])$ for each mouse.

1176 detect more communities, and those communities often contain cells from one brain region
 1177 only. At longer time bin widths, we detect fewer communities, and those communities tend
 1178 to contain cells from multiple brain regions. When we examine the distance between (or
 1179 similarity between) the anatomical division of the cells, and the detected communities we
 1180 notice that the two clusterings are more similar at shorter time bin widths (see figure 2.12).

1181 When we applied the network noise rejection and community detection process to the
 1182 networks based on the signal correlations ρ_{signal} we found the number of communities we
 1183 detected reduced with increasing time bin width. But the number of communities detected
 1184 was less than that for the total correlations or the spike count correlations. The commu-
 1185 nities detected always tended to contain cells from multiple regions at both short and long
 1186 timescales (see figures 2.11c and 2.11d). The communities detected bore very little relation
 1187 to the anatomical division of the cells. The adjusted Rand index between the community
 1188 clustering and the anatomical ‘clustering’ is close to zero for every time bin width (see figure
 1189 2.13b). This indicates that the similarity between the clusterings is close to chance. We did

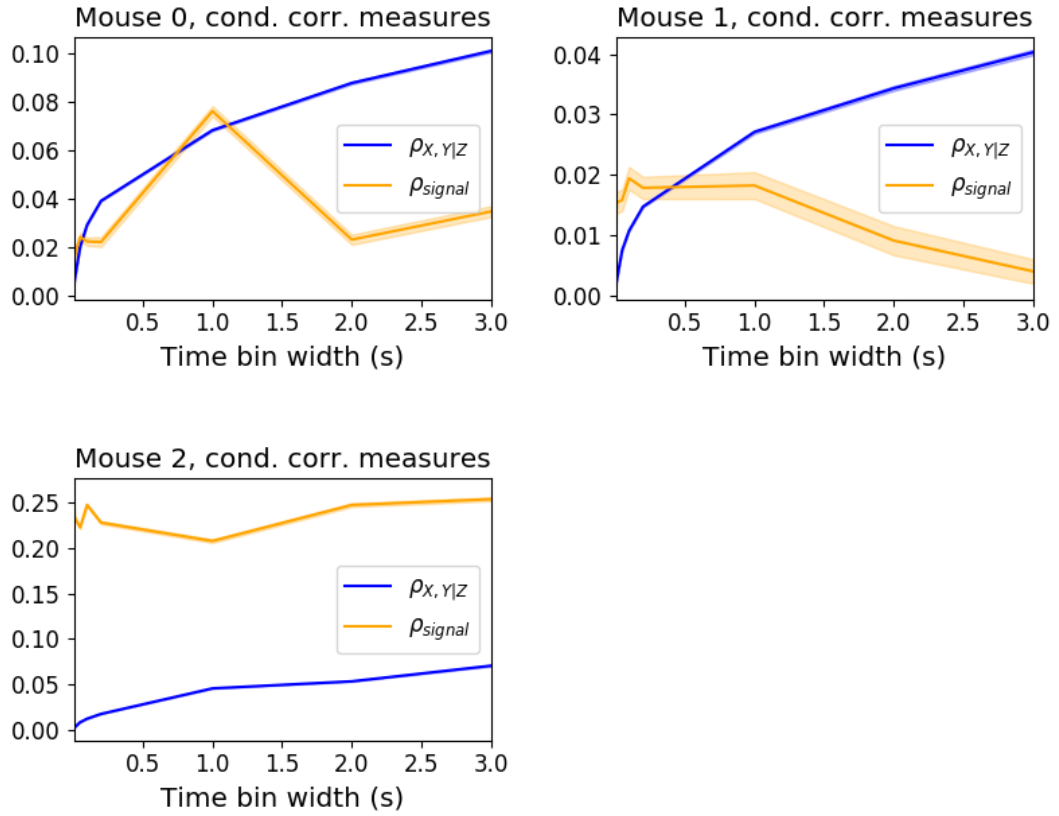


FIGURE 2.10: Comparing the components of the total spike count covariance across different values for the time bin width. We saw a consistent increase in $\rho_{X,Y|Z}$ as the time bin width increased in all three subjects. But we saw different trends for in ρ_{signal} for each of the subjects.

1190 observe a slight downward trend in the variation of information with increasing bin width
 1191 (see figure 2.13a), but this is more likely due to a decrease in the number of communities
 1192 detected rather than any relationship with anatomy.

1193 We also observed that the network noise rejection process rejected some of the cells
 1194 when applied to the network based on the signal correlations. This means that those cells
 1195 did not contribute to the additional structure of the network beyond that captured by the
 1196 sparse weighted configuration model. This is why the matrices in figures 2.11c and 2.11d are
 1197 smaller than their analogues in figures 2.11a and 2.11b.

1198 2.2.8 Absolute correlations and negative rectified correlations

1199 At the moment, the network noise rejection protocol can only be applied to weighted undi-
 1200 rected graphs with non-negative weights. This meant that we had to rectify our correlated
 1201 networks before applying the network noise rejection and community detection process. We

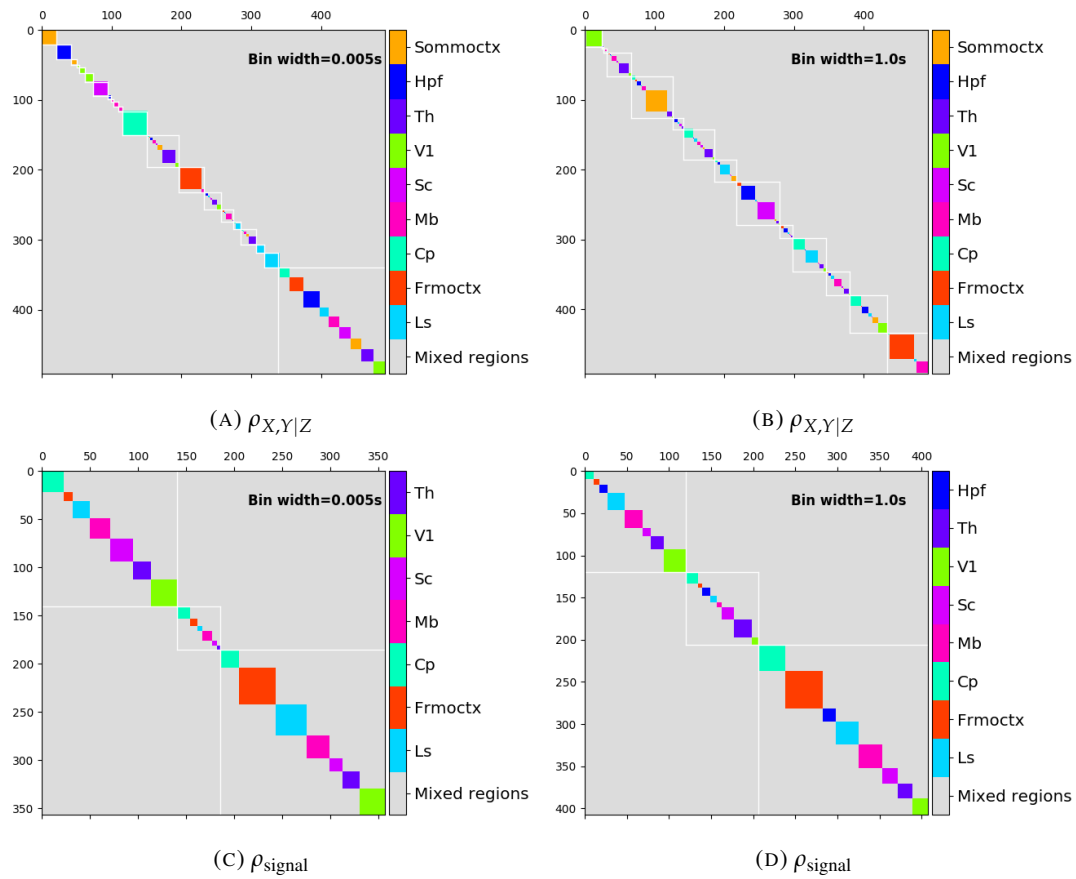


FIGURE 2.11: Matrices showing the regional membership of pairs by colour, and the communities in which those pairs lie. (A-B) Detected communities and regional membership matrix for network based on rectified spike count correlation $\rho_{X,Y|Z}$, using time bin widths of 0.005s and 1s respectively. (C-D) Detected communities and regional membership matrix for network based on rectified signal correlation ρ_{signal} , using time bin widths of 0.005s and 1s respectively.

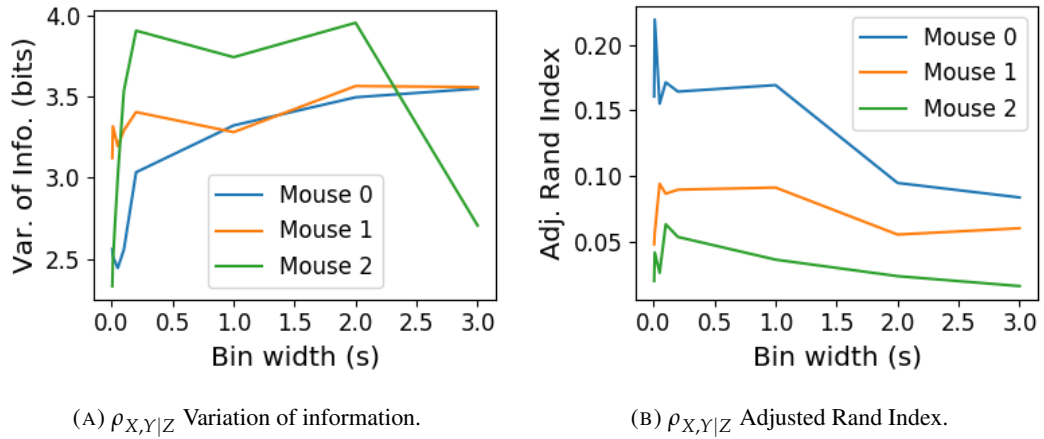


FIGURE 2.12: Distance and similarity measures between the anatomical division of the neurons, and the communities detected in the network based on the spike count correlations $\rho_{X,Y|Z}$. (a) The variation of information is a ‘distance’ measure between clusterings. The distance between the anatomical ‘clustering’ and the community clustering increases as the time bin width increases. (b) The adjusted Rand index is a similarity measure between clusterings. The detected communities become less similar to the anatomical division of the cells as the time bin width increases.

1202 wanted to investigate what would happen if instead of rectifying the correlations, we used the
 1203 absolute value, or reversed the signs of the correlations and then rectified.

1204 When we used the absolute value of the correlations, we found very similar results to
 1205 those shown above for the rectified total correlations and the rectified spike count correla-
 1206 tions. The only exception being that we detected more communities. This could indicate that
 1207 we detected both positively and negatively correlated communities, but we haven’t done any
 1208 further investigation so we cannot say for sure.

1209 When we used the sign reversed rectified correlated networks, we tended to find fewer
 1210 communities and often found no signal network after applying network noise rejection. This
 1211 indicates that there was not much structure in the negatively correlated networks beyond that
 1212 captured by the sparse weighted configuration model.

1213 2.3 Discussion

1214 It is well established that the brain uses correlated behaviour in neuronal ensembles to repre-
 1215 sent the information taken in through sensation (Cohen and Maunsell, 2009; Litwin-Kumar,
 1216 Chacron, and Doiron, 2012; deCharms and Merzenich, 1996). However, most studies that
 1217 examine the nature of these correlations in-vivo, study an ensemble of cells from only one
 1218 brain region (Cohen and Kohn, 2011). Furthermore, recent results have shown that behaviour

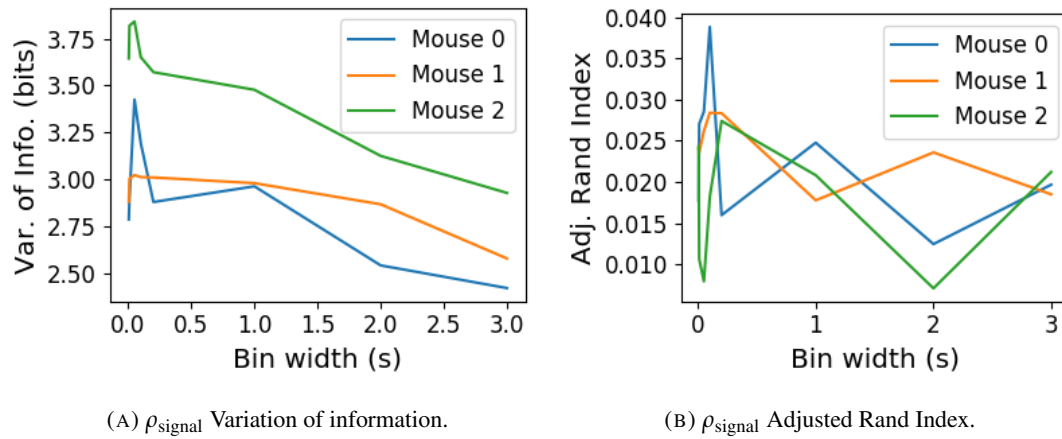


FIGURE 2.13: Distance and similarity measures between the anatomical division of the neurons, and the communities detected in the network based on the signal correlations ρ_{signal} . (a) The variation of information is a ‘distance’ measure between clusterings. The distance between the anatomical ‘clustering’ and the community clustering increases as the time bin width increases. (b) The adjusted Rand index is a similarity measure between clusterings. The detected communities become less similar to the anatomical division of the cells as the time bin width increases.

can drive correlated activity in multiple brain regions, including those not normally associated with motor control (Stringer et al., 2019). In this study, we utilised one of the newly recorded large datasets containing electrophysiological recordings from multiple brain regions simultaneously. We investigated correlated behaviour in these different brain regions and we investigated correlated behaviour between neurons in different regions, during spontaneous behaviour.

A number of studies have found that the timescale of correlated behaviour induced by a stimulus can be modulated by the stimulus structure and behavioural context. For example, the spike train correlations between cells in weakly electric fish are modulated by the spatial extent of the stimulus (Litwin-Kumar, Chacron, and Doiron, 2012), and neurons in the marmoset primary auditory cortex modulate their spike timing (and therefore correlation) in response to stimulus features without modulating their firing rate (deCharms and Merzenich, 1996). Furthermore, the width of the time bins over which spike counts are measured has been shown to have an effect on the magnitude of those correlations (Cohen and Kohn, 2011). Despite this, very little research has been done comparing correlation measures from the same dataset at different timescales. We investigated this by varying the time bin width used to bin spike times into spike counts from as short as 5ms up to 3s.

In order to further investigate the effect of these correlations at different timescales, we regarded our neuronal ensemble as a weighted undirected graph, where each neuron is represented by a node, and the weight on each edge is the correlation between the neurons

connected by that edge. We then applied a novel clustering method from network science (Humphries et al., 2019) to identify communities in these networks. These networks, and the community detection process, were completely agnostic of anatomical division of the cells in our ensemble. When we compared the detected communities with the anatomical division of the cells using distance and similarity measures for clusterings, we found that the detected communities were more similar to the anatomical division and shorter timescales. That is, when we used a wider time bin to count spikes, and computed pairwise correlations with these spike counts, the correlated communities tended to exist within anatomical regions at shorter timescales, and tended to span anatomical regions at longer timescales. This could reflect localised functional correlations at short time scales rippling outwards across brain regions at longer timescales.

We acknowledged that the region spanning correlated communities that we detected at longer time scales could exist due to collating activity driven by distinct spontaneous activities. In order to account for this, we modelled the spike counts as a linear function of the top 500 principal components of a video of the mouse's face filmed simultaneously with the electrophysiological readings. We applied our network noise rejection and community detection process to the weighted undirected networks formed by the spike count correlations and the signal correlations that we calculated using our model. For the spike count correlation networks, we found much the same results as for the total correlations as described above. For the signal correlations, the communities detected in these networks bore little relation to the anatomical division of the cells.

There is a lot of room for further investigation based on this research. For a start, the data that we used here were collected from nine different regions in the mouse brain, but none of these regions were part of the somatosensory cortex. Given that a mouse experiences so much of its environment through its sense of smell, some data from this region would be interesting to investigate. On the same theme, the mice in the experiment from which the data were collected were headfixed and placed on a rotating ball, but were otherwise behaving spontaneously. Had these mice been exposed to a visual, aural, or olfactory stimulus, we could have examined the responses of the cells in the brain regions corresponding to vision, hearing, and olfaction, and compared these responses to the responses from the other brain regions. Furthermore, we could have investigated the interaction between the sets of responses.

Another space for further investigation is the community detection. The algorithm that we used here never detects overlapping communities. But functional communities could indeed

have overlaps. Clustering methods that detect overlapping clusters do exist (Baadel, Thabtah, and Lu, 2016). Applying one of those algorithms could yield some interesting results. Also, the community detection algorithm that we used here cannot process graphs with negative weights, this forced us to separate positive and negative correlations before applying our network noise rejection and community detections process, or use the absolute value of our correlations. A community detection algorithm that can work on weighted undirected graphs with negative weights could yield some interesting results here.

2.4 Data

The data that we used in this project were collected by Nick Steinmetz and his lab members (Stringer et al., 2019).

2.4.1 Brain regions

Neuropixels probes were used to collect extracellular recordings (Jun et al., 2017) from three different mice. The mice were awake, headfixed, and engaging in spontaneous behaviour. The mice were of different sexes and different ages. One mouse was ‘wild-type’, the others were mutants. Details as follows:

1. male, wild type, P73.
2. female, TetO-GCaMP6s, Camk2a-tTa, P113
3. male, Ai32, Pvalb-Cre, P99

Eight probes were used to collect readings from 2296, 2668, and 1462 cells respectively.

Data were collected from nine brain regions in each mouse:

- Caudate Putamen (CP)
- Frontal Motor Cortex (Frmoctx)
- Hippocampal formation (Hpf)
- Lateral Septum (Ls)
- Midbrain (Mb)
- Superior Colliculus (Sc)
- Somatomotor cortex (Sommoctx)

- Thalamus (Th)
- Primary visual cortex (V1)

Readings were continuous and lasted for about 1 hour (Stringer et al., 2019). Locations of each of the probes can be seen in figure 2.14.

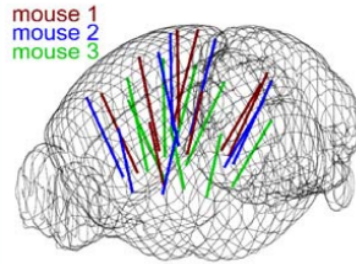


FIGURE 2.14: **Probe Locations:** The locations of the probes in each of the three mouse brains (Stringer et al., 2019).

2.4.2 Video recordings

Video recordings of the mouse's face were taken during the spontaneous behaviour. We had access to the top 500 principle components and top 500 eigenvectors of the processed videos. The frequency of recording was slightly less than 40Hz. Each frame contained 327×561 pixels. These principal components were used as behavioural data. We controlled for these components when taking measurements conditioned on behaviour.

2.5 Methods

2.5.1 Binning data

We transformed the spike timing data into binned spike count data by dividing the experimental period into time bins and counting the spikes fired by each cell within the time period covered by each of those bins. The data were divided into time bins of various widths ranging from 0.01s to 4s.

If the total length of the recording period was not an integer multiple of the time bin width, we cut off the remaining time at the end of the recording period. This period was at most 3.99s. This is far less than the total recording time of around 1 hour. So, this detail would not affect our results.

2.5.2 Correlation coefficients

We calculated Pearson's correlation coefficient for pairs of spike counts from pairs of neurons. For jointly distributed random variables X and Y , Pearson's correlation coefficient is defined as:

$$\rho_{XY} = \frac{\text{cov}(X, Y)}{\sigma_X \sigma_Y} \quad (2.1)$$

$$= \frac{E[(X - \mu_X)(Y - \mu_Y)]}{\sigma_X \sigma_Y} \quad (2.2)$$

where E denotes the expected value, μ denotes the mean, and σ denotes the standard deviation. The correlation coefficient is a normalised measure of the covariance. It can take values between 1 (completely correlated) and -1 (completely anti-correlated). Two independent variables will have a correlation coefficient of 0. But, having 0 correlation does not imply independence.

If we do not know the means and standard deviations required for equation 2.1, but we have samples from X and Y , Pearson's sample correlation coefficient is defined as:

$$r_{XY} = \frac{\sum_{i=1}^n (x_i - \bar{x})(y_i - \bar{y})}{\sqrt{\sum_{i=1}^n (x_i - \bar{x})^2} \sqrt{\sum_{i=1}^n (y_i - \bar{y})^2}} \quad (2.3)$$

where $\{(x_i, y_i)\}$ for $i \in \{1, \dots, n\}$ are the paired samples from X and Y , and $\bar{x} = \frac{1}{n} \sum_{i=1}^n x_i$, and $\bar{y} = \frac{1}{n} \sum_{i=1}^n y_i$ are the sample means.

In practice we used the python function `scipy.stats.pearsonr` to calculate the correlation coefficients.

Total correlations, r_{SC}

The total correlation (r_{SC}) of two cells is the correlation between the spike counts of those cells in response to a given stimulus condition.

Shuffled total correlations

We measured the shuffled total correlations between two neurons by randomly permuting one of the neuron's spike counts and measuring the total correlations. These shuffled correlations were useful when measuring the effect of time bin width on correlations, and when deciding which correlations should be preserved when creating correlation networks (see section 2.5.5).

1339 Separating Correlations & Anti-correlations

1340 In order to compare the effect of bin width on measures of negative r_{SC} (anti-correlation) and
 1341 positive r_{SC} separately, we had to separate correlated and anti-correlated pairs. To do this, we
 1342 simply measured the mean r_{SC} , taking the mean across all the bin widths. If this quantity was
 1343 positive or zero we regarded the pair as positively correlated. If this quantity was negative
 1344 we regarded the pair as anti-correlated.

1345 2.5.3 Conditioning on behavioural data

Our behavioural data consisted of the top 500 principal components (PCs) of a processed video recording of the mouse's face (see section 2.4.2). Denoting the spike count of a given cell by X , and the PCs by Z_1, \dots, Z_{500} , we wanted to model X as a function of Z_1, \dots, Z_{500} in order to estimate

$$E[X|Z_1, \dots, Z_{500}] = \int_{x \in X} xP(X = x|Z_1, \dots, Z_{500})dx \quad (2.4)$$

$$= \int_{x \in X} x \frac{P(X = x, Z_1, \dots, Z_{500})}{P(Z_1, \dots, Z_{500})} dx \quad (2.5)$$

1346 Given the 500 components, a naïve estimation of $P(Z_1, \dots, Z_{500})$ or $P(X, Z_1, \dots, Z_{500})$ by
 1347 histogramming was impossible. Therefore we modelled X as a linear combination of the
 1348 PCs.

1349 Linear regression

1350 We modelled the spike count of a given cell, X , as a linear combination of the PCs of the
 1351 video of the mouse's face, $\mathbf{Z} = Z_1, \dots, Z_{500}$. We tried three different types of regularization

- 1352 • $L1$ or 'Lasso'
- 1353 • $L2$ or 'Ridge regression'
- 1354 • 'Elastic net' regularisation (a linear combination of both $L1$ and $L2$ regularisation penalties)
- 1355

1356 The elastic net regularisation performed the best, so we stuck with that.

1357 Elastic net regularisation

Suppose we wish to model n observations of a random variable X , $\mathbf{x} = (x_1, \dots, x_n)$ using n instances of m predictors $\mathbf{Z} = (Z_1, \dots, Z_m)$. The naïve elastic net criterion is

$$L(\lambda_1, \lambda_2, \boldsymbol{\beta}) = \|\mathbf{x} - \mathbf{Z}\boldsymbol{\beta}\|^2 + \lambda_2 \|\boldsymbol{\beta}\|_2 + \lambda_1 \|\boldsymbol{\beta}\|_1 \quad (2.6)$$

where

$$\|\boldsymbol{\beta}\|_2 = \sum_{j=1}^m \beta_j^2 \quad (2.7)$$

$$\|\boldsymbol{\beta}\|_1 = \sum_{j=1}^m |\beta_j| \quad (2.8)$$

The naïve elastic net estimator $\hat{\boldsymbol{\beta}}$ is the minimiser of the system of equations 2.6 (Zou and Hastie, 2005)

$$\hat{\boldsymbol{\beta}} = \arg \min_{\boldsymbol{\beta}} L(\lambda_1, \lambda_2, \boldsymbol{\beta}) \quad (2.9)$$

1358 We implemented the model using the `ElasticNetCV` method of Python's

1359 `sklearn.linear.models` package.

1360 As well as using the PCs, we also tried fitting the models using the raw video data recon-
1361 structed from the PCs and eigenvectors. These models performed worse than those using the
1362 PCs. We expected this because each representation contains the same amount of information,
1363 but the raw video representation spreads this information across many more components.
1364 This requires more parameter fitting, but given the same information.

1365 Conditional covariance

We calculated the expected value of the conditional covariance using the law of total covariance.

$$\text{cov}(X, Y) = E[\text{cov}(X, Y|Z)] + \text{cov}(E[X|Z], E[Y|Z]) \quad (2.10)$$

1366 where these expected values are calculated with respect to the distribution of Z as a random
1367 variable.

1368 The law of total covariance breaks the covariance into two components. The first com-
1369 ponent $E[\text{cov}(X, Y|Z)]$ is the expected value, under the distribution of Z , of the conditional

covariance $\text{cov}(X, Y|Z)$. This covariance could be interpreted as the unnormalised version of what Cohen et al. (2011) call the spike count correlation (Cohen and Kohn, 2011), aka. the noise correlation. In particular, this is the covariance of the spike counts in response to repeated presentation of identical stimuli.

The second component is analogous to what Cohn et al. (2011) call the *signal correlation* (Cohen and Kohn, 2011). In particular, $\text{cov}(E[X|Z], E[Y|Z])$ is the covariance between spike counts in response to different stimuli.

Using our linear model, we calculated $E[X|Z_1, \dots, Z_{500}]$ for each cell X . Then we proceeded to calculate

$$E[\text{cov}(X, Y|Z_1, \dots, Z_{500})] = \text{cov}(X, Y) - \quad (2.11)$$

$$\text{cov}(E[X|Z_1, \dots, Z_{500}], E[Y|Z_1, \dots, Z_{500}]) \quad (2.12)$$

Measures of conditional correlation

As a measure of expected correlation, we measured the ‘event conditional correlation’ (Maugis, 2014)

$$\rho_{XY|Z} = \frac{E[\text{cov}(X, Y|Z)]}{\sqrt{E[\text{var}(X|Z)]E[\text{var}(Y|Z)]}} \quad (2.13)$$

Although this is not an actual correlation, it is an intuitive analogue to the correlation as a normalised version of the covariance.

For comparison, we also measured the ‘signal correlation’

$$\rho_{\text{signal}} = \frac{\text{cov}(E[X|Z], E[Y|Z])}{\sqrt{\text{var}(E[X|Z])\text{var}(E[Y|Z])}} \quad (2.14)$$

this is an actual correlation.

2.5.4 Information Theory

Entropy $H(X)$

The entropy of a random variable X , with outcomes x_1, \dots, x_N , and corresponding probabilities p_1, \dots, p_N is defined as

$$H(X) = - \sum_{n=1}^N p_n \log_2 p_n \quad (2.15)$$

1383 This quantity is also known as the information entropy or the ‘surprise’. It measures the
 1384 amount of uncertainty in a random variable. For example, a variable with a probability of 1
 1385 for one outcome, and 0 for all other outcomes will have 0 bits entropy, because it contains no
 1386 uncertainty. But a variable with a uniform distribution will have maximal entropy as it is the
 1387 least predictable. This quantity is analogous to the entropy of a physical system (Shannon,
 1388 1948). Note that any base may be used for the logarithm in equation 2.15, but using base 2
 1389 means that the quantity will be measured in ‘bits’.

The joint entropy of two jointly distributed random variables X and Y , where Y has outcomes y_1, \dots, y_M , is defined as

$$H(X, Y) = - \sum_{n=1}^N \sum_{m=1}^M P(X = x_n, Y = y_m) \log_2 P(X = x_n, Y = y_m) \quad (2.16)$$

1390 If X and Y are independent then $H(X, Y) = H(X) + H(Y)$. Otherwise $H(X, Y) <$
 1391 $H(X) + H(Y)$. When X and Y are completely dependent $H(X, Y) = H(X) = H(Y)$.

The conditional entropy of Y conditioned on X is defined as

$$H(Y|X) = - \sum_{n=1}^N \sum_{m=1}^M P(X = x_n, Y = y_m) \log_2 \frac{P(X = x_n, Y = y_m)}{P(X = x_n)} \quad (2.17)$$

1392 When X and Y are independent $H(Y|X) = H(Y)$. Intuitively, we learn nothing of Y by
 1393 knowing X , so Y is equally uncertain whether we know X or not. If Y is totally dependent
 1394 on X , then the fraction in the logarithm is 1, which gives $H(Y|X) = 0$.

1395 These entropy measures are the basis of the mutual information measure.

1396 Maximum entropy limit

When spiking data is binned into spike counts there is an upper limit on the entropy of these data. The maximum entropy discrete distribution is the discrete uniform distribution. A random variable with this distribution will take values from some finite set with equal probabilities. Binned spike count data will take values between 0 and some maximum observed spike count n_{\max} . A neuron with responses that maximises entropy will take these values with equal probability, i.e. if $i \in \{0, \dots, n_{\max}\}$ then $P(X = i) = \frac{1}{n_{\max} + 1}$. The entropy of

this neuron will be

$$\begin{aligned}
 H(X) &= - \sum_{i=0}^{n_{\max}} P(X=i) \log_2 P(X=i) \\
 &= - \sum_{i=0}^{n_{\max}} \frac{1}{n_{\max}+1} \log_2 \left(\frac{1}{n_{\max}+1} \right) \\
 &= - \log_2 \left(\frac{1}{n_{\max}+1} \right) \\
 &= \log_2 (n_{\max}+1)
 \end{aligned}$$

Therefore, the maximum entropy of the binned spike counts of a neuron is $\log_2 (n_{\max} + 1)$. Of course, it would be very unusual for a neuron to fire in accordance with the discrete uniform distribution. Most measurements of entropy taken on binned spiking data will be much lower than the maximum. See figure 2.15 to see the maximum entropy as a function of the maximum observed spike count.

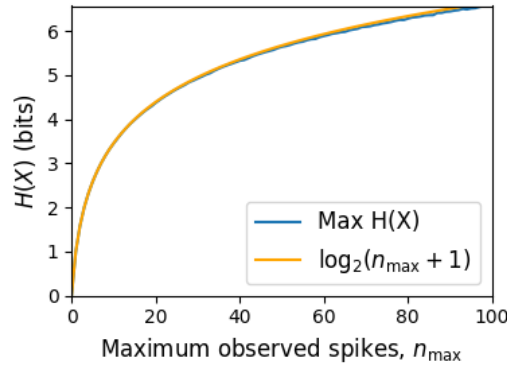


FIGURE 2.15: **Entropy Limit:** The upper limit on entropy of binned spike count data as a function of the maximum observed spike count. The orange line is the analytical maximum. The blue line is the entropy of samples with $N = 1000$ data points taken from the discrete uniform distribution.

1402 **Mutual Information** $I(X;Y)$

1403 The mutual information can be defined mathematically in a number of ways, all of which are
 1404 equivalent. These definitions illustrate the different ways of interpreting the mutual informa-
 1405 tion.

For two jointly distributed random variables X and Y , the mutual information $I(X; Y)$ is defined as

$$I(X; Y) = H(Y) - H(Y|X) \quad (2.18)$$

$$= H(X) - H(X|Y) \quad (2.19)$$

Equation 2.18 fits with the following intuition: The mutual information between X and Y is the reduction in uncertainty about X gained by knowing Y , or vice versa. We could also say the mutual information is the amount of information gained about X by knowing Y , or vice versa.

Another useful entropy based definition for the mutual information is

$$I(X; Y) = H(X) + H(Y) - H(X, Y) \quad (2.20)$$

This definition is useful because it does not require the calculation of conditional probabilities.

The mutual information can also be defined in terms of marginal, joint, and conditional distributions. For example,

$$I(X; Y) = - \sum_{n=1}^N \sum_{m=1}^M P(X = x_n, Y = y_m) \log_2 \frac{P(X = x_n, Y = y_m)}{P(X = x_n)P(Y = y_m)} \quad (2.21)$$

Notice that this can be rewritten as a Kullback–Leibler divergence.

$$I(X; Y) = D_{KL}(P(X, Y) || P(X)P(Y)) \quad (2.22)$$

So, we can also think of the mutual information as a measure of the difference between the joint distribution of X and Y , and the product of their marginal distributions. Since the product of the marginal distributions is the joint distribution for independent variables, we can think of the mutual information as a measure of the variables' dependence on one another.

The minimum value that $I(X; Y)$ can take is 0. This occurs when the random variables X and Y are independent. Then we have $H(X|Y) = H(X)$, and $H(Y|X) = H(Y)$, which according to equation 2.18, gives $I(X; Y) = 0$. We also have that $H(X, Y) = H(X) + H(Y)$ in this case, which according equation 2.20, gives $I(X; Y) = 0$. Finally, we also have $P(X, Y) = P(X)P(Y)$, which leaves us with 1 in the argument for the logarithm in equation 2.21, which again gives $I(X; Y) = 0$.

The mutual information reaches its maximum value when one of the variables X and Y is completely determined by knowing the value of the other. In that case $I(X; Y) = \min\{H(X), H(Y)\}$.

Variation of Information $VI(X, Y)$

The variation of information is another information theoretical quantity based on the mutual information. It is defined as

$$VI(X; Y) = H(X) + H(Y) - 2I(X; Y) \quad (2.23)$$

We can rewrite this as the summation of two positive quantities

$$VI(X; Y) = [H(X) - I(X; Y)] + [H(Y) - I(X; Y)] \quad (2.24)$$

In English, the variation of information is the summation of the uncertainty in the random variables X and Y excluding the uncertainty shared by those variables.

This measure will become more relevant when we go on to talk about clusterings because $VI(X; Y)$ forms a metric on the space of clusterings.

Measuring entropies & mutual information

In practice, we measured the mutual information between spike counts using Python and the python package `pyitlib`. We used the PT-bias correction technique to estimate the bias of our measurements when measuring the mutual information between the spike counts of two cells (Treves and Panzeri, 1995).

When measuring the mutual information between clusterings we used Python, but we used the `mutual_info_score`, `adjusted_mutual_info_score`, and `normalized_mutual_info_score` functions from the `sklearn.metrics` part of the `sklearn` package.

2.5.5 Network analysis

Correlation networks

In order to analyse functional networks created by the neurons in our ensemble, we measured the total correlation between each pair of neurons. These measurements induced an

undirected weighted graph/network between the neurons. The weight of each connection was equal to the total correlation between each pair of neurons.

We followed the same procedure for total correlations 2.5.2, spike count correlations, and signal correlations 2.5.3.

Rectified correlations

At the time of writing, the community detection method outlined in (Humphries et al., 2019) could only be applied to networks with positively weighted connections. But many neuron pairs were negatively correlated. To apply the community detection method, we *rectified* the network, by setting all the negative weights to zero.

We also looked for structure in the network created by negative correlations by reversing the signs of the correlations, and rectifying these correlations before applying our network analysis.

Finally, we used the absolute value of the correlations as the weights for the graph/network. By doing this, we hoped to identify both correlated and anti-correlated functional communities of neurons.

Sparsifying data networks

When creating our correlation networks, we wanted to exclude any correlations that could be judged to exist ‘by chance’. To do this, we measured the 5th and 95th percentile of the shuffled correlations (see section 2.5.2) for the given mouse and time bin width. We then set all the data correlations between these two values to 0. This excluded any ‘chance’ correlations from our network, and created a sparser network. This allowed us to make use of the ‘sparse weighted configuration model’ as described in section 2.5.5.

Communities

Given some network represented by an adjacency matrix \mathbf{A} , a community within that network is defined as a collection of nodes where the number of connections within these nodes is higher than the expected number of connections between these nodes. In order to quantify the ‘expected’ number of connections, we need a model of expected networks. This is analogous to a ‘null model’ in traditional hypothesis testing. We test the hypothesis that our data network departs from the null network model to a statistically significant degree. For undirected unweighted networks, the canonical model of a null network is the configuration

1473 model (Fosdick et al., 2016). Since we are working with weighted sparse networks, we used
 1474 more suitable null models, described below.

1475 **Weighted configuration model**

1476 The *weighted configuration model* is a canonical null network model for weighted networks.
 1477 Given some data network, the weighted configuration model null network will preserve the
 1478 degree sequence and weight sequence of each node in the data network. But the edges will
 1479 be distributed randomly (Fosdick et al., 2016). Any structure in the data network beyond
 1480 its degree sequence and weight sequence will not be captured in the weighted configuration
 1481 model. So, this model can be used in testing the hypothesis that this extra structure exists.

1482 **Sparse weighted configuration model**

1483 The *sparse weighted configuration model* is another null network model. Similar in nature to
 1484 the weighted configuration model (see section 2.5.5), but the sparsity of the data network is
 1485 preserved in the null network. This is achieved by sampling from a probability distribution
 1486 for the creation or non-creation of each possible connection, then distributing the weight of
 1487 the data network randomly in this sparse network (Humphries et al., 2019). This is the null
 1488 network that we used when searching for additional structure in our data networks.

1489 **Spectral rejection**

1490 We made use of the spectral rejection algorithm as outlined in (Humphries et al., 2019). The
 1491 spectral rejection algorithm is a method for finding structure in a network not captured by a
 1492 supposed null model, if such structure exists.

To describe the method, we denote our data network matrix \mathbf{W} , we denote the expected network of our null network model as $\langle \mathbf{P} \rangle$. Then the departure of our data network from the null network can be described by the matrix

$$\mathbf{B} = \mathbf{W} - \langle \mathbf{P} \rangle \quad (2.25)$$

1493 a common choice for $\langle \mathbf{P} \rangle$ in community detection is the ‘configuration model’ (Fosdick et
 1494 al., 2016; Humphries, 2011). The matrix \mathbf{B} is often called the configuration matrix, in this
 1495 context we will use the term ‘deviation matrix’ as it captures the deviation of \mathbf{W} from the
 1496 null model.

To test for structure in the network represented by \mathbf{W} , we examine the eigenspectrum of \mathbf{B} and compare it to the eigenspectrum of our null model. Firstly, note that since our data model doesn't allow self loops, and is not directed, the matrix representing the network will be symmetric and positive semi-definite, and will therefore be invertible with real eigenvalues. We selected a null model with the same characteristics.

To find the eigenspectrum of the null model, we generated N samples from our null model P_1, \dots, P_N , and we measured their deviation matrices B_1, \dots, B_N . We then calculated the eigenspectrum of each of those samples. We calculated the upper bound of the null model eigenspectrum by taking the mean of the largest eigenvalues of B_1, \dots, B_N . We calculated a lower bound on the null model eigenspectrum by taking the mean of the smallest eigenvalues of B_1, \dots, B_N .

We then calculated the eigenspectrum of \mathbf{B} , our data network deviation matrix. If any of those eigenvalues lay outside of the upper or lower bounds of the null model eigenspectrum, this is evidence of additional structure not captured by the null model. If we chose the sparse weighted configuration model (see section 2.5.5) as our null network model, then eigenvalues lying below the lower bound indicate k -partite structure in the network. For example, if one eigenvalue lay below the lower bound, this would indicate some bipartite structure in the data network. If any eigenvalues lay above the upper bound of the null model eigenspectrum, this is evidence of community structure in the data network. For example, one eigenvalue of \mathbf{B} lying above the upper bound of the null model eigenspectrum indicates the presence of two communities in the network (Humphries, 2011).

Node rejection

If there are d data eigenvalues lying outside of the null network eigenspectrum, the d eigenvectors corresponding to these eigenvalues will form a vector space. If we project the nodes of our network into this vector space, by projecting either rows or columns of the data matrix, we can see how strongly each node contributes to the vector space. Nodes that contribute strongly to the additional structure will project far away from the origin, nodes that do not contribute to the additional structure will project close to the origin. We want to use this information to discard those nodes that do not contribute.

We can test whether a node projects *far* away from the origin or *close* to the origin using the eigenvalues and eigenvectors of B_1, \dots, B_N . The j th eigenvector and eigenvalue of B_i gives a value for a null network's projection into the j th dimension of the additional structure vector space. The matrices B_1, \dots, B_N give N projections into that dimension.

1530 These projections are a distribution of the null networks' projections. If the data node's
 1531 projection exceeds that of the null network projections this node is judged to project *far* from
 1532 the origin, and therefore contribute to the additional structure. Otherwise, the node is judged
 1533 to project *close* to the origin, and is therefore rejected (Humphries et al., 2019).

1534 Community detection

1535 Another application for this d dimensional space is community detection. We first project
 1536 all of the nodes into this d -dimensional space, then perform the clustering in this space. The
 1537 clustering and community detection procedure is described in (Humphries, 2011).

1538 In practice, the procedure is carried out n times (we chose $n = 100$ times), this returns n
 1539 clusterings. We resolve these n clusterings to one final clustering using *consensus clustering*.
 1540 We used the consensus clustering method that uses an explicit null model for the consensus
 1541 matrix, as outlined in (Humphries et al., 2019).

1542 2.5.6 Clustering Comparison

A clustering \mathcal{C} is a partition of a set D into sets C_1, C_2, \dots, C_K , called clusters, that satisfy the following for all $k, l \in \{1, \dots, K\}$:

$$C_k \cap C_l = \emptyset \quad (2.26)$$

$$\bigcup_{k=1}^K C_k = D \quad (2.27)$$

1543 If we consider two clusterings, \mathcal{C} with clusters C_1, C_2, \dots, C_K and \mathcal{C}' with clusters
 1544 C'_1, C'_2, \dots, C'_K . There are a number of measurements we can use to compare \mathcal{C} and \mathcal{C}' . In
 1545 the following, the number of elements in D is denoted by n , and the number of elements in
 1546 cluster C_k is n_k .

1547 Adjusted Rand Index

1548 The *adjusted Rand Index* is a normalised similarity measure for clusterings based on pair
 1549 counting.

1550 If we consider the clusterings \mathcal{C} and \mathcal{C}' , and denote

- 1551 • the number of pairs in the same cluster in \mathcal{C} and \mathcal{C}' by N_{11}
- 1552 • the number of pairs in different clusters in \mathcal{C} and \mathcal{C}' by N_{00}

- 1553 • the number of pairs in the same cluster in \mathcal{C} and different clusters in \mathcal{C}' by N_{10}
- 1554 • the number of pairs in different clusters in \mathcal{C} and the same cluster in \mathcal{C}' by N_{01}

then the *Rand Index* is defined as

$$RI = \frac{N_{11} + N_{00}}{N_{11} + N_{00} + N_{10} + N_{01}} = \frac{N_{11} + N_{00}}{\binom{n}{2}} \quad (2.28)$$

1555 The Rand Index is 1 when the clusterings are identical, and 0 when the clusterings are com-
1556 pletely different.

The *adjusted Rand Index* intends on correcting the Rand Index for chance matching pairs. This is defined as

$$ARI = \frac{2(N_{00}N_{11} - N_{01}N_{10})}{(N_{00} + N_{01})(N_{01} + N_{11}) + (N_{00} + N_{10})(N_{10} + N_{11})} \quad (2.29)$$

1557 The adjusted Rand Index is 1 when the clusterings are identical, and 0 when the Rand Index
1558 is equal to its expected value.

1559 Clusterings as random variables

If we take any random element of D , the probability that this element is in cluster C_k of clustering \mathcal{C} is

$$P(K = k) = \frac{n_k}{n} \quad (2.30)$$

1560 this defines a probability distribution, which makes the clustering a random variable. Any
1561 clustering can be considered as a random variable this way.

This means that we can measure any of the information theoretic quantities defined in section 2.5.4 with respect to clusterings. For example, the entropy of a clustering is

$$H(\mathcal{C}) = - \sum_{k=1}^K \frac{n_k}{n} \log \frac{n_k}{n} \quad (2.31)$$

If we have two clusterings, the joint probability distribution of these clusterings is defined as

$$P(K = k, K' = k') = \frac{|C_k \cap C'_{k'}|}{n} \quad (2.32)$$

1562 The joint distribution allows us to define the mutual information between two clusterings,
1563 $I(\mathcal{C}; \mathcal{C}')$ (Meilă, 2007).

1564 Information based similarity measures

The mutual information between two clusterings is a similarity measure, with $I(\mathcal{C}; \mathcal{C}') = 0$ if \mathcal{C} and \mathcal{C}' are completely different, and $I(\mathcal{C}; \mathcal{C}') = H(\mathcal{C}) = H(\mathcal{C}')$ if \mathcal{C} and \mathcal{C}' are identical. This can be normalised in a number of different ways to make more similarity measures (Vinh, Epps, and Bailey, 2010)

$$NMI_{joint} = \frac{I(\mathcal{C}; \mathcal{C}')}{H(\mathcal{C}, \mathcal{C}')} \quad (2.33)$$

$$NMI_{max} = \frac{I(\mathcal{C}; \mathcal{C}')}{\max\{H(\mathcal{C}), H(\mathcal{C}')\}} \quad (2.34)$$

$$NMI_{sum} = \frac{2I(\mathcal{C}; \mathcal{C}')}{H(\mathcal{C}) + H(\mathcal{C}')} \quad (2.35)$$

$$NMI_{sqr} = \frac{I(\mathcal{C}; \mathcal{C}')}{\sqrt{H(\mathcal{C})H(\mathcal{C}')}} \quad (2.36)$$

$$NMI_{min} = \frac{I(\mathcal{C}; \mathcal{C}')}{\min\{H(\mathcal{C}), H(\mathcal{C}')\}} \quad (2.37)$$

We can control for chance similarities between the two clusterings by measuring the *adjusted mutual information* between the clusterings. This is defined as

$$AMI_{sum} = \frac{I(\mathcal{C}; \mathcal{C}') - E\{I(\mathcal{C}; \mathcal{C}')\}}{\frac{1}{2}[H(\mathcal{C}) + H(\mathcal{C}')] - E\{I(\mathcal{C}; \mathcal{C}')\}} \quad (2.38)$$

1565 The first term in the demoniator, taking the average of the marginal entropies, can be replaced
1566 by taking the maximum, minimum, or the geometric mean (Vinh, Epps, and Bailey, 2010).

1567 Information based metrics

The variation of information between two clusterings $VI(\mathcal{C}; \mathcal{C}')$ (see section 2.5.4) is a metric on the space of clusterings (Meilă, 2007). That is,

$$VI(\mathcal{C}; \mathcal{C}') \geq 0 \quad (2.39)$$

$$VI(\mathcal{C}; \mathcal{C}') = 0 \iff \mathcal{C} = \mathcal{C}' \quad (2.40)$$

$$VI(\mathcal{C}; \mathcal{C}') = VI(\mathcal{C}'; \mathcal{C}) \quad (2.41)$$

$$VI(\mathcal{C}; \mathcal{C}'') \leq VI(\mathcal{C}; \mathcal{C}') + VI(\mathcal{C}'; \mathcal{C}'') \quad (2.42)$$

Another metric is the *information distance* (Vinh, Epps, and Bailey, 2010)

$$D_{max} = \max\{H(\mathcal{C}), H(\mathcal{C}')\} - I(\mathcal{C}; \mathcal{C}') \quad (2.43)$$

Both of these can be normalised

$$NVI(\mathcal{C}; \mathcal{C}') = 1 - \frac{I(\mathcal{C}; \mathcal{C}')}{H(\mathcal{C}, \mathcal{C}')} \quad (2.44)$$

$$d_{max} = 1 - \frac{I(\mathcal{C}; \mathcal{C}')}{\max\{H(\mathcal{C}), H(\mathcal{C}')\}} \quad (2.45)$$

1568 Comparing detected communities and anatomical divisions

1569 In order to quantify the difference or similarity between the communities detected in our cor-
 1570 relation network and the anatomical classification of the cells in that network, we considered
 1571 the communities and the anatomical regions as clusters in two different clusterings, \mathcal{C}_{comm}
 1572 and \mathcal{C}_{anat} , respectively. We then measured the similarity between the clusterings using the
 1573 mutual information, the adjusted mutual information, and the normalised mutual informa-
 1574 tion. We measured the difference between, or the distance between, the clusterings using the
 1575 variation of information, the normalised variation of information, and the normalised infor-
 1576 mation distance. We also measured the difference between the clusterings using the adjusted
 1577 Rand Index, just to use a non-information based measure.

1578 We took all of these measures for communities detected using different time bin widths.
 1579 This gave us an idea of the effect of time bin width on correlation networks in neural ensem-
 1580 bles relative to anatomical regions within those ensembles.

1581 **Chapter 3**

1582 **A simple two parameter distribution**
1583 **for modelling neuronal activity and**
1584 **capturing neuronal association**

UNIVERSITY OF BRISTOL

Abstract

Engineering

Department of Computer Science

Doctor of Philosophy

Investigating, implementing, and creating methods for analysing large neuronal ensembles

by Thomas J. DELANEY

Recent developments in electrophysiological technology have lead to an increase in the size of electrophysiology datasets. Consequently, there is a requirement for new analysis techniques that can make use of these new datasets, while remaining easy to use in practice. In this work, we fit some one or two parameter probability distributions to spiking data collected from a mouse exposed to visual stimuli. We show that the Conway-Maxwell-binomial distribution is a suitable model for the number of active neurons in a neuronal ensemble at any given moment. This distribution fits these data better than binomial or beta-binomial distributions. It also captures the correlated activity in the primary visual cortex induced by stimulus onset more effectively than simply measuring the correlations, at short timescales ($< 10\text{ms}$). We also replicate the finding of Churchland et al (2010) relating to stimulus onset quenching neural variability in cortical areas, and we show a correspondence between this quenching and changes in one of the parameters of the fitted Conway-Maxwell-binomial distributions.

3.1 Introduction

Recent advances in electrophysiological technology, such as ‘Neuropixels’ probes (Jun et al., 2017) have allowed extracellular voltage measurements to be collected from larger numbers of cells than traditional methods, in multiple brain regions simultaneously, and routinely. These larger datasets require innovative methods to extract information from the data in a reasonable amount of time, ‘reasonable’ being subjective in this case.

Theoretically, all the information at any given moment in an electrophysiological dataset with n neurons could be captured by calculating the probability distribution for every possible spiking pattern. This would require defining a random variable with 2^n possible values, a task that quickly becomes impossible as n increases. Attempts at approximating this random variable often involve measuring pairwise or higher order correlations (Schneidman et al., 2006; Flach, 2013; Ganmor, Segev, and Schneidman, 2011). But pairwise correlations may not be enough to characterise instantaneous neural activity (Tkačik et al., 2014). Furthermore, these kinds of models tend to ignore the temporal structure of neuronal data, in favour of smaller model size, and scalability.

Higher order correlations would be helpful here, but defining these correlations can be tricky, never-mind quantifying them. If we use the interaction parameters arising from the exponential family model as measures of higher order correlations, measuring these correlations becomes computationally impractical quite quickly also (the number of ‘three neuron correlations’ to measure scales with $\binom{n}{3}$). In this paper, we dispense with measuring correlations directly, and attempt to characterise correlated behaviour by measuring ‘association’; a more general concept that includes correlation.

In this work, we examined the ability of simple distributions to model the number of active (spiking) neurons in a neuronal ensemble at any given timepoint. We compared a little-known distribution named the Conway-Maxwell-binomial distribution to the binomial distribution and the beta-binomial distribution. The binomial distribution is a probability distribution over the number of successes in a sequence of independent and identical Bernoulli trials. The beta-binomial distribution is similar, but allows for a bit more flexibility while still being a model for heterogeneity. Similar to the binomial and beta-binomial, the Conway-Maxwell-binomial distribution is a probability distribution over the number of successes in a series of Bernoulli trials, but allows over- and under-dispersion relative to the binomial distribution. This distribution should therefore be a good candidate for our purposes. We found that Conway-Maxwell-binomial distribution was usually the best candidate of the three that

we examined.

We also observed some interesting changes in the number of active neurons in the primary visual cortex and hippocampus at stimulus onset and some changes in this activity in the thalamus which were sustained for the full duration of the stimulus presentation. This let us know that there were some responses to model.

We found that fitting a Conway-Maxwell-binomial distribution was a better method of capturing association between neurons than measuring the spike count correlation for the short time bins that we used ($< 10\text{ms}$).

Finally, we also wanted to investigate parallels between the parameters of the Conway-Maxwell-binomial distribution and quantities that have been established as relevant to sensory processing. So, we replicated the findings made by Churchland et al. (2010) relating to a reduction in neural variability at stimulus onset in the macaque cortical regions, but for data taken from the mouse primary visual cortex. We compared these findings to the values of the fitted Conway-Maxwell-binomial distribution parameters.

3.2 Data

We used data collected by Nick Steinmetz and his lab ‘CortexLab at UCL’ (Steinmetz, Carandini, and Harris, 2019). The data can be found online ¹ and are free to use for research purposes.

Two ‘Phase3’ Neuropixels (Jun et al., 2017) electrode arrays were inserted into the brain of an awake, head-fixed mouse for about an hour and a half. These electrode arrays recorded 384 channels of neural data each at 30kHz and less than $7\mu\text{V}$ RMS noise levels. The sites are densely spaced in a ‘continuous tetrode’-like arrangement, and a whole array records from a 3.8mm span of the brain. One array recorded from visual cortex, hippocampus, and thalamus, the other array recorded from motor cortex and striatum. The data were spike-sorted automatically by Kilosort and manually by Nick Steinmetz using Phy. In total 831 well-isolated individual neurons were identified.

3.2.1 Experimental protocol

The mouse was shown a visual stimulus on three monitors placed around the mouse at right angles to each other, covering about ± 135 degrees azimuth and ± 35 degrees elevation.

¹<http://data.cortexlab.net/dualPhase3/>

The stimulus consisted of sine-wave modulated full-field drifting gratings of 16 drift directions ($0^\circ, 22.5^\circ, \dots, 337.5^\circ$) with 2Hz temporal frequency and 0.08 cycles/degree spatial frequency displayed for 2 seconds plus a blank condition. Each of these 17 conditions were presented 10 times in a random order across 170 different trials. There were therefore 160 trials with a drifting-grating visual stimulus present, and 10 trials with a blank stimulus.

3.3 Methods

3.3.1 Binning data

We converted the spike times for each cell into spike counts by putting the spike times into time bins of a given ‘width’ (in milliseconds). We used time bins of 1ms, 5ms, and 10ms. We used different time bin widths to assess the impact of choosing a bin width.

3.3.2 Number of *active* neurons

To count the number of active neurons in each neuronal ensemble, we split the time interval for each trial into bins of a given width. We counted the number of spikes fired by each cell in each bin. If a cell fired *at least* one spike in a given bin, we regarded that cell as active in that bin. We recorded the number of active cells in every bin, and for the purposes of further analysis, we recorded each cell’s individual spike counts.

It should be noted that when we used a bin width of 1ms, the maximum number of spikes in any bin was 1. For the wider time bins, some bins had spike counts greater than 1. Consequently when using a bin width of 1ms, the number of active neurons and the total spike count of a given bin were identical. But for wider bin widths, the total spike count was greater than the number of active neurons.

So for the 1ms bin width, the activity of a neuron and the number of spikes fired by that neuron in any bin can be modelled as a Bernoulli variable. But for wider time bins, only the activity can be modelled in this way.

3.3.3 Moving windows for measurements

When taking measurements (e.g. moving average over the number of active neurons) or fitting distributions (eg. the beta binomial distribution) we slid a window containing a certain number of bins across the data, and made our measurements at each window position. For example, when analysing 1ms bin data, we used a window containing 100 bins, and we slid

Bin width (ms)	Window size (bins)	Window size (ms)	Windows per trial
1ms	100	100ms	296
5ms	40	200ms	286
10ms	40	400ms	266

TABLE 3.1: Details of the different bin width and analysis window sizes used when binning spike times, and analysing those data.

the window across the time interval for each trial moving 10 bins at a time. So that for 3060ms of data, we made 296 measurements.

For the 5ms bin width data, we used windows containing 40 bins, and slid the window 2 bins at a time when taking measurements.

For the 10ms bin width data, we used windows containing 40 bins, and slid the window 1 bin at a time when taking measurements (see table 3.1 for concise details).

By continuing to use windows containing 40 bins, we retained statistical power but sacrificed the number of measurements taken.

There was an interval between each trial with a grey image in place of the moving of the moving bar stimulus. This interval varied in time. But we included some of this interval when recording the data for each trial. We started recording the number of active neurons, and the number of spikes from each neuron from 530ms before each trial until 1030ms after each trial. This way, we could see the change in our measurements at the onset of a stimulus and the end of stimulus presentation.

As mentioned in section 3.3.2, we recorded the number of active neurons in each bin, and the spike count for each neuron in each bin. The actual measurements we took using these data in each window were as follows:

Moving average The average number of active cells in each window.

Moving variance The variance of the number of active cells in each window.

Average correlation We measured the correlation between the spike counts of each pair of cells in the ensemble, and took the average of these measurements.

Binomial p We fitted a binomial distribution to the data in each window and recorded the fitted probability of success, p in each case.

Beta-binomial α, β We fitted a beta-binomial distribution to the data in each window, and recorded the values of the fitted shape parameters, α and β , of each distribution.

1721 **Conway-Maxwell-binomial distribution** p, ν We fitted a Conway-Maxwell-binomial dis-
 1722 tribution to the data in each window, and recorded the fitted values of p and ν for each
 1723 distribution.

1724 **Log-likelihoods** We also recorded the log-likelihood of each of the fitted distributions for
 1725 each window.

1726 3.3.4 Fano factor

The *Fano factor* of a random variable is defined as the ratio of the variable's variance to its mean.

$$F = \frac{\sigma^2}{\mu} \quad (3.1)$$

1727 We measured the Fano factor of the spike count of a given cell by measuring the mean and
 1728 variance of the spike count across trials, and taking the ratio of those two quantities. When
 1729 calculated in this way the Fano factor can be used as a measure of neural variability that
 1730 controls for changes in the firing rate. This is similar to the calculation used in (Churchland
 1731 et al., 2010).

1732 3.3.5 Probability Distributions suitable for modelling ensemble activity

1733 We present here three different probability distributions that could be suitable to model the
 1734 number of active neurons in an ensemble. Each distribution has the set $\{0, \dots, n\}$ as its sup-
 1735 port, where n is the number of neurons in the ensemble. These are simple distributions with
 1736 either two or three parameters each. However, we regard n as known when using these dis-
 1737 tributions for modelling, so in effect each distribution has either one or two free parameters.

1738 Association

1739 *Association* between random variables is similar to the correlation between random variables
 1740 but is more general in concept. The correlation is a measure of association; and association
 1741 doesn't have a mathematical definition like correlation does. Essentially, the association
 1742 between two random variables is their tendency to take the same or similar values. Positively
 1743 associated variables tend to take the same value, and negatively associated variables tend to
 1744 take different values. In this research, we work with probability distributions of the number of
 1745 successes in a set of Bernoulli trials. These Bernoulli variables may or may not be associated.

1746 A probability distribution over the number of successes in n Bernoulli trials, where the
 1747 Bernoulli variables may be associated, could constitute a good model for the number of active
 1748 neurons in an ensemble of n neurons.

1749 **Binomial distribution**

The binomial distribution is a two parameter discrete probability distribution that can be thought of as a probability distribution the number of successes from n independent Bernoulli trials, each with the same probability of success. The parameters of the binomial distribution are n the number of trials, and $0 \leq p \leq 1$, the probability of success for each of these trials. A random variable with the binomial distribution can take values from $\{0, \dots, n\}$. The probability mass function of the distribution is

$$P(k; n, p) = \binom{n}{k} p^k (1 - p)^{n-k} \quad (3.2)$$

1750 As a model for the activity of a neuronal ensemble, the main problem with the binomial
 1751 distribution is that it treats each neuron, represented as a Bernoulli trial, as independent. It is
 1752 well known that neurons are not independent, and that correlated behaviour between neurons
 1753 is vital for representing sensory information (**cohen**). The binomial distribution falls short
 1754 in this regard, but it is useful as performance benchmark when assessing the performance of
 1755 other models.

1756 **Beta-binomial distribution**

1757 The beta distribution is the conjugate distribution of the binomial distribution. The beta-
 1758 binomial distribution is the combination of the beta distribution and the binomial distribution,
 1759 in that the probability of success for the binomial distribution is sampled from the beta dis-
 1760 tribution. This allows the beta-binomial distribution to capture some over dispersion relative
 1761 to the binomial distribution.

The beta-binomial distribution is a three parameter distribution, n the number of Bernoulli trials, and $\alpha \in \mathbb{R}_{>0}$ and $\beta \in \mathbb{R}_{>0}$ the shape parameters of the beta distribution. The probability mass function for the beta-binomial distribution is

$$P(k; n, \alpha, \beta) = \binom{n}{k} \frac{B(k + \alpha, n - k + \beta)}{B(\alpha, \beta)} \quad (3.3)$$

1762 where $B(\alpha, \beta)$ is the beta function.

This probability distribution can be reparametrised in a number of ways. One of which defines new parameters π and ρ by

$$\pi = \frac{\alpha}{\alpha + \beta} \quad (3.4)$$

$$\rho = \frac{1}{\alpha + \beta + 1} \quad (3.5)$$

This reparametrisation is useful because π acts as a location parameter analogous to the p parameter of a binomial distribution. A value of $\rho > 0$ indicates over-dispersion relative to a binomial distribution.

As a model for the activity of a neuronal ensemble, the beta-binomial distribution is more suitable than a binomial distribution because the over-dispersion of the beta-binomial distribution can be used to model positive association between the neurons. An extreme example of this over-dispersion/positive association can be seen in figure 3.1b. In this figure, the neurons are positively associated and so tend to take the same value, consequently the probability mass of the beta-binomial distribution builds up close to $k = 0$ and $k = n$. It is worth noting that the location parameter for each distribution has the same value, $p = \pi = 0.5$.

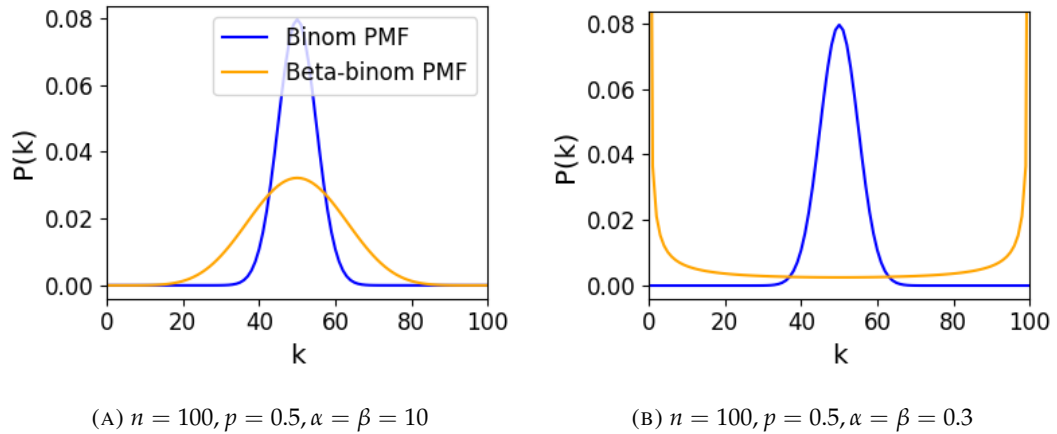


FIGURE 3.1: Figures showing the over-dispersion possible for a beta-binomial distribution relative to a binomial distribution. Parameters are shown in the captions.

Conway-Maxwell-binomial distribution

The Conway-Maxwell-binomial distribution (COMb distribution) is a three parameter generalisation of the binomial distribution that allows for over dispersion and under dispersion

relative to the binomial distribution. The parameters of the distribution are n the number of Bernoulli trials, and two shape parameters $0 \leq p \leq 1$, and $\nu \in \mathbb{R}$.

The probability mass function of the COMb distribution is

$$P(k; n, p, \nu) = \frac{1}{S(n, p, \nu)} \binom{n}{k}^{\nu} p^k (1-p)^{n-k} \quad (3.6)$$

where

$$S(n, p, \nu) = \sum_{j=0}^n \binom{n}{j}^{\nu} p^j (1-p)^{n-j} \quad (3.7)$$

The only difference between this PMF and the PMF for the standard binomial is the introduction of ν and the consequent introduction of the normalising function $S(n, p, \nu)$.

Indeed, if $\nu = 1$ the COMb distribution is identical to the binomial distribution with the same values for n and p . We can see in figure 3.2d that the KL-divergence $D_{KL}(P_{COMb}(n, p, \nu) || P_{Bin}(n, p)) = 0$ along the line where $\nu = 1$. The analytical expression for the divergence is

$$D_{KL}(P_{COMb}(k; n, p, \nu) || P_{Bin}(k; n, p)) = (\nu - 1) E_{P_{COMb}(k; n, p, \nu)} \left[\log \binom{n}{k} \right] \quad (3.8)$$

$$- \log S(n, p, \nu) \quad (3.9)$$

At $\nu = 1$, we have $S(n, p, 1)$ which is just the sum over the binomial PMF, so $S(n, p, 1) = 1$ and therefore $D_{KL}(P_{COMb}(n, p, \nu) || P_{Bin}(n, p)) = 0$.

If $\nu < 1$ the COMb distribution will exhibit over-dispersion relative to the binomial distribution. If $p = 0.5$ and $\nu = 0$ the COMb distribution is the discrete uniform distribution, and if $\nu < 0$ the mass of the COMb distribution will tend to build up near $k = 0$ and $k = n$. This over-dispersion represents positive association in the Bernoulli variables. An example of this over-dispersion can be seen in figure 3.2b.

If $\nu > 1$ the COMb distribution will exhibit under-dispersion relative to the binomial distribution. The larger the value of ν the more probability mass will build up at $n/2$ for even n , or at $\lfloor n/2 \rfloor$ and $\lceil n/2 \rceil$ for odd n . This under-dispersion represents negative association in the Bernoulli variables. An example of this under-dispersion can be seen in figure 3.2a.

It should be noted that the p parameter of the COMb distribution does not correspond to the mean of the distribution, as is the case for the binomial p parameter, and beta-binomial π parameter. That is, the COMb p parameter is not a location parameter. An illustration of this can be seen in figure 3.2c. This is because an interaction between the p and ν parameters skews the mean. There is no analytical expression for the mean of the COMb distribution.

ν	Relative dispersion	Association between neurons/variables
< 1	over	positive
1	none	none
> 1	under	negative

TABLE 3.2: Relative dispersion of the COMb distribution, and association between Bernoulli variables as represented by the value of the ν parameter.

1797 Since the COMb distribution has the potential to capture positive and negative associa-
 1798 tions between the neurons/Bernoulli variables, it should be an excellent candidate for mod-
 1799 elling the number of active neurons in a neuronal ensemble.

1800 We wrote a dedicated Python package to enable easy creation and fitting of COMb dis-
 1801 tribution objects. The format of the package imitates the format of other distribution objects
 1802 from the `scipy.stats` Python package. The COMb package can be found here:

1803 https://github.com/thomasjdelaney/Conway_Maxwell_Binomial_Distribution

1804 3.3.6 Fitting

1805 We fitted binomial, beta-binomial, and Conway-Maxwell-binomial (COMb) distributions to
 1806 the neural activity in each of the overlapping windows covering each trial. To fit the distribu-
 1807 tions we minimised the appropriate negative log likelihood function using the data from the
 1808 window.

There is an analytical solution for maximum likelihood estimate of the binomial distribu-
 tion's p parameter.

$$\hat{p} = \frac{1}{n} \sum_{i=1}^N k_i \quad (3.10)$$

1809 We minimised the negative log likelihood function of the beta-binomial distribution nu-
 1810 merically. We calculated the negative log likelihood for a sample directly, by taking the sum
 1811 of the log of the probability mass function for each value in the sample. We minimised the
 1812 negation of that function using the `minimise` function of the `scipy.optimize` Python
 1813 package.

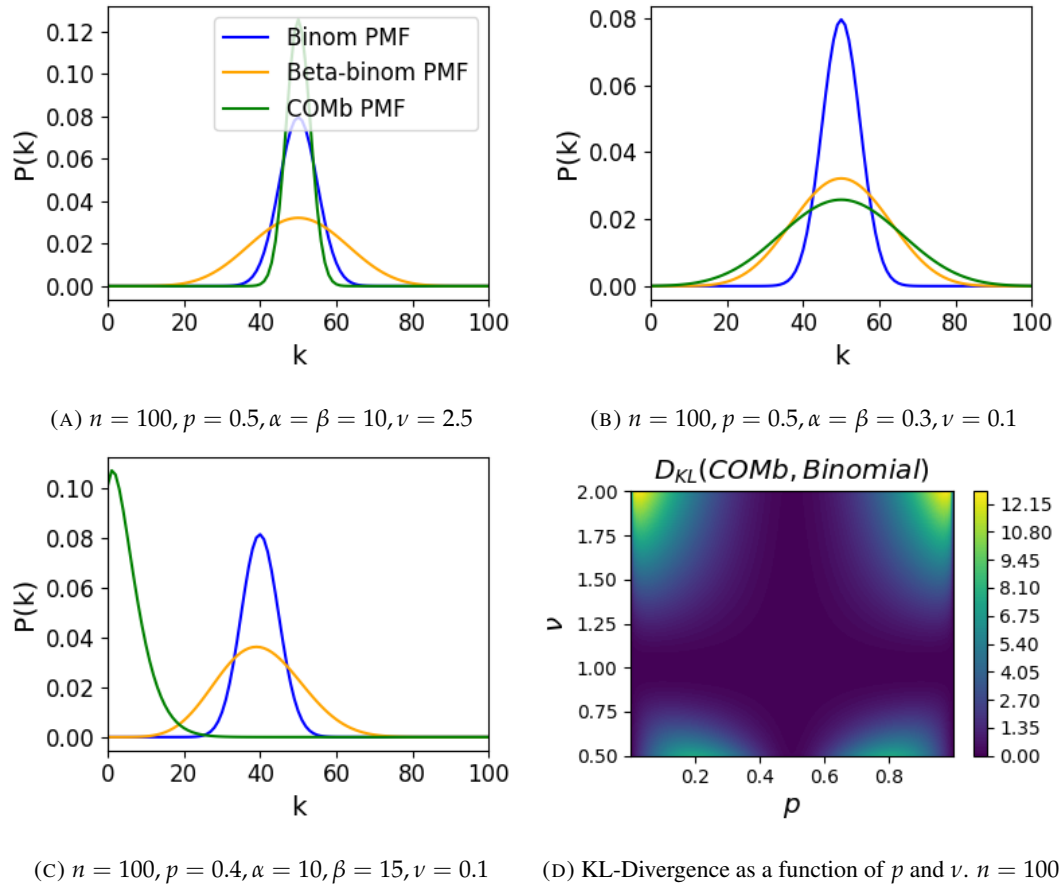


FIGURE 3.2: Figures showing (A) the under-dispersion and (B) over-dispersion permitted by the COMB distribution relative to a binomial distribution. (C) illustrates that the p parameter of the COMB distribution does not correspond to the mean of the distribution, as it does for the binomial and beta-binomial distributions. (D) shows a heatmap for the value of the Kullback-Liebler divergence between the COMB distribution and the standard binomial distribution with same value for n , as a function of p and ν . Parameters are shown in the captions.

The log likelihood function of the COMb distribution given some sample $\{k_1, \dots, k_N\}$ is

$$\ell(p, \nu | k_1, \dots, k_N) = N [n \log(1 - p) - \log S(n, p, \nu)] \quad (3.11)$$

$$+ \log \frac{p}{1 - p} \sum_{i=1}^N k_i \quad (3.12)$$

$$+ \nu \sum_{i=1}^N \log \binom{n}{k_i} \quad (3.13)$$

We minimised the negation of this function using numerical methods. More specifically, we used the `minimise` function of the `scipy.optimize` Python package.

3.3.7 Goodness-of-fit

After fitting, we measured the goodness-of-fit of each model/distribution with their log likelihood. We calculated this directly using the `logpmf` functions of the distribution objects in Python.

3.4 Results

We defined a neuron as *active* in a time bin if it fires at least one spike during the time interval covered by that bin. We measured the number of active neurons in the primary visual cortex of a mouse in 1ms bins across 160 trials of a moving bar visual stimulus. We then slid a 100ms window across these 1ms bins taking measurements, and fitting distributions along the way. We did the same for neurons in the thalamus, hippocampus, striatum, and motor cortex. We repeated the analysis for 5ms time bins with 40 bin windows, and 10ms time bins with 40 bin windows.

3.4.1 Increases in mean number of active neurons and variance in number of active neurons at stimulus onset in some regions

We measured the average number of active neurons, and the variance of the number of active neurons in a 100ms sliding window starting 500ms before stimulus onset until 1000ms after stimulus onset. We found differences in the response across regions. There were no observed changes in response to the stimulus in the motor cortex or the striatum. The changes in the other regions are detailed below.

Primary visual cortex

We found a transient increase in both the average and variance of the number of active neurons at stimulus onset, followed by a fall to pre-stimulus levels, followed by another transient increase (see figure 3.3). The oscillation in both of these measurements appear to reflect the frequency of the stimulus (see Data section 3.2.1), and it is known that stimulus structure can influence response structure (“parencite –litwinkumar”). We see a similar but lower amplitude oscillation at the end of the stimulus presentation.

Hippocampus

In the hippocampus we observed a transient increase in the average number of active neurons and in the variance of the number of active neurons at stimulus onset (see figure 3.4). The increase lasted about 125ms, and the subsequent fall to baseline took the a similar amount of time.

Thalamus

In the thalamus we observed a transient increase in the both the average and variance of the number of active neurons on stimulus onset, followed by a fall to pre-stimulus levels, followed by a sustained increase until the stimulus presentation ends.

As one you might expect for a visual stimulus, the change in the average number of active neurons was greatest in the primary visual cortex. In this region, this quantity doubled on stimulus onset. In contrast, in the hippocampus and the thalamus, the average number of active neurons only increased by a fraction of the unstimulated baseline value. The duration of the response in V1 and the hippocampus at stimulus onset was 300 – 400ms, but the response in the thalamus appeared to last for the duration of stimulus presentation. The V1 also showed a change in the average number of active neurons at stimulus end. The change was similar to that observed at stimulus onset, but smaller in magnitude (see figures ??)

3.4.2 Conway-Maxwell-binomial distribution is usually a better fit than binomial or beta-binomial

Since the Conway-Maxwell-binomial distribution has not been fitted to neuronal data before, it is not clear that it would be a better fit than the binomial or beta-binomial distributions. In order to find out which parametric distribution was the best fit for the largest proportion of our data, we fit a binomial, a beta-binomial, and a Conway-Maxwell-binomial (COMb)

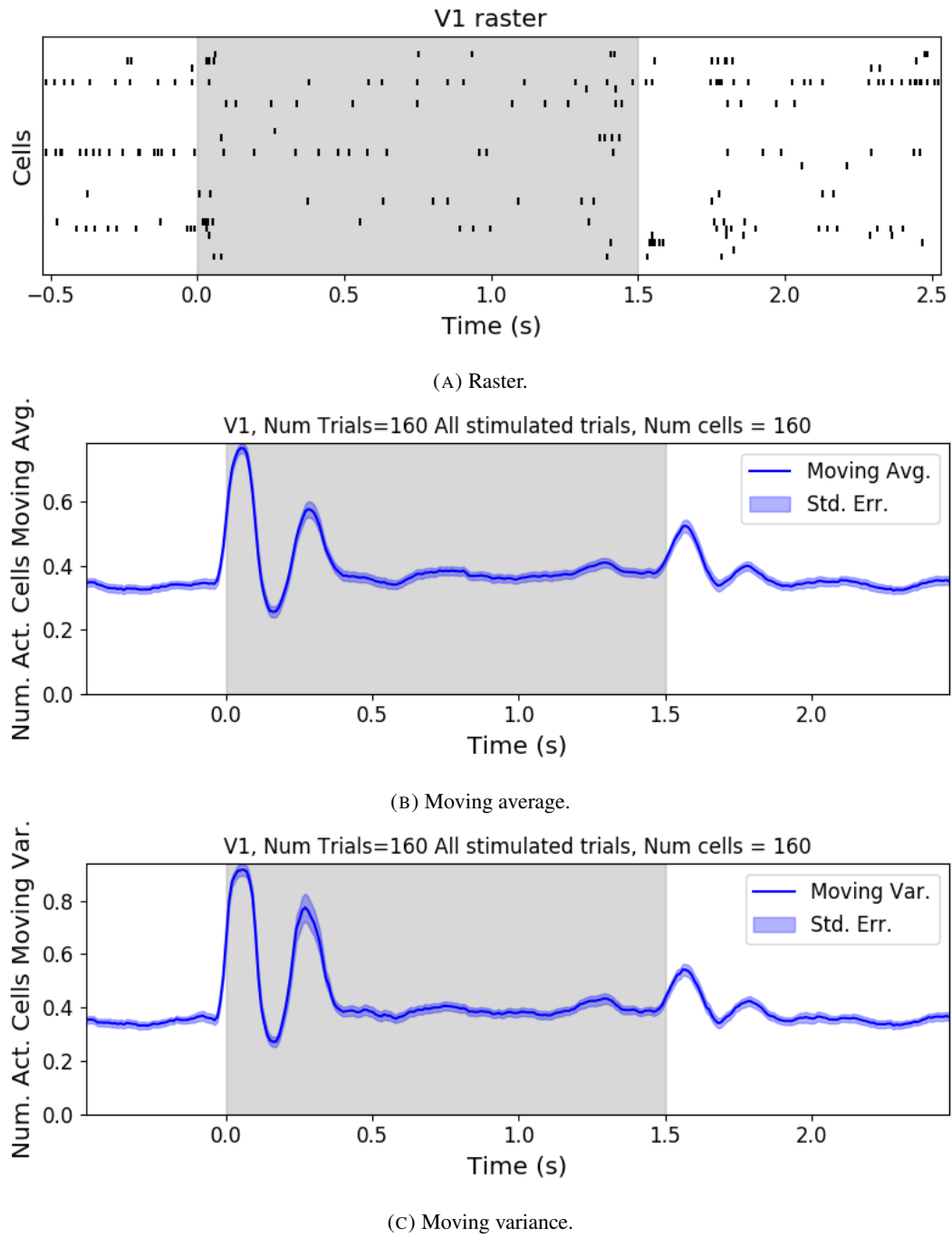


FIGURE 3.3: (A) Raster plot showing the spikes fired by 33 randomly chosen neurons in the primary visual cortex. (B-C) (B) average and (C) variance of the number of active neurons, measured using a sliding window 100ms wide, split into 100 bins. The midpoint of the time interval for each window is used as the timepoint (x-axis point) for the measurements using that window. The grey shaded area indicates the presence of a visual stimulus. The opaque line is an average across the 160 trials that included a visual stimulus of any kind. We can see a transient increase in the average number of active neurons and the variance of this number, followed by a fluctuation and another increase.

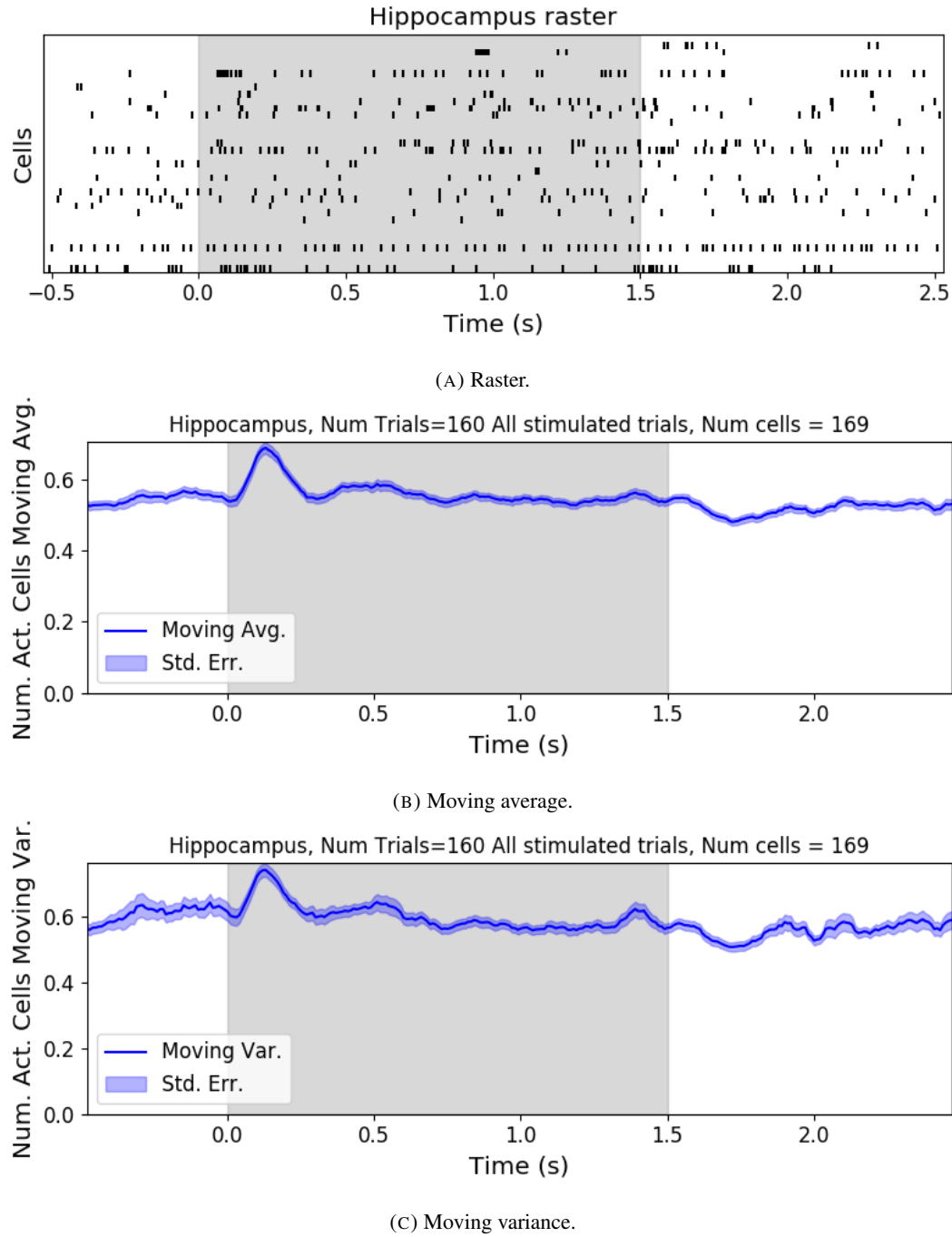
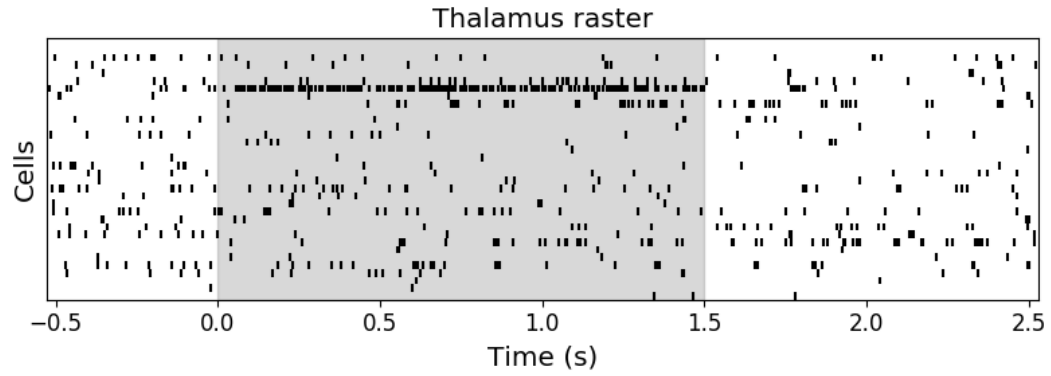
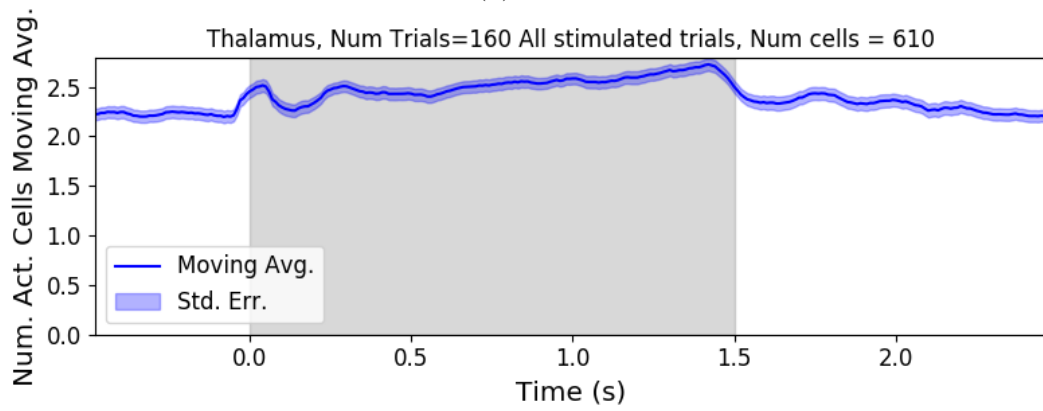


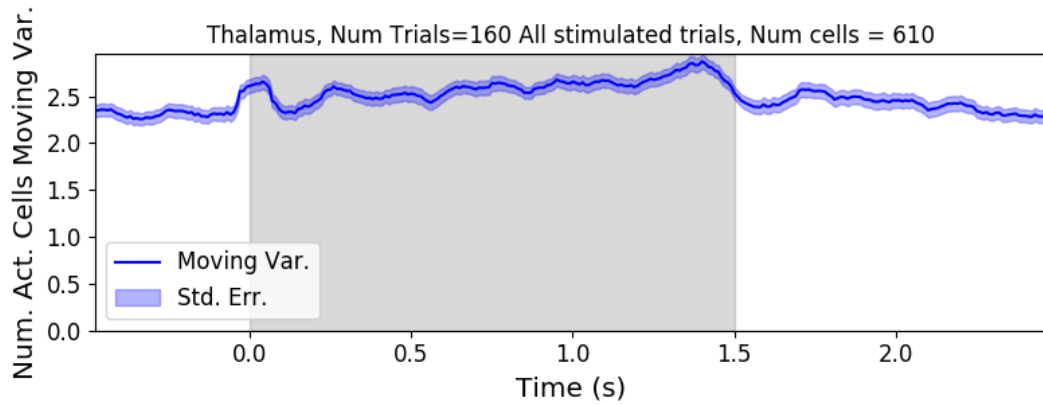
FIGURE 3.4: (A) Raster plot showing the spikes fired by 33 randomly chosen neurons in the hippocampus. (B-C) (B) average and (C) variance of the number of active neurons, measured using a sliding window 100ms wide, split into 100 bins. The midpoint of the time interval for each window is used as the timepoint (x-axis point) for the measurements using that window. The grey shaded area indicates the presence of a visual stimulus. The opaque line is an average across the 160 trials that included a visual stimulus of any kind. We can see a transient increase in the average number of active neurons and the variance of this number at stimulus onset.



(A) Raster.



(B) Moving average.



(C) Moving variance.

FIGURE 3.5: (A) Raster plot showing the spikes fired by 33 randomly chosen neurons in the thalamus. (B-C) (B) average and (C) variance of the number of active neurons, measured using a sliding window 100ms wide, split into 100 bins. The midpoint of the time interval for each window is used as the timepoint (x-axis point) for the measurements using that window. The grey shaded area indicates the presence of a visual stimulus. The opaque line is an average across the 160 trials that included a visual stimulus of any kind. We can see in immediate increase at stimulus onset, a subsequent fall, and another sustained increased until the stimulus presentation ends.

distribution to each window for each bin width, and each region. Then we assessed the goodness-of-fit of each distribution by calculating the log-likelihood of each fitted distribution using the associated sample. We measured the proportion of samples for which each distribution was the best fit, for each bin width value and each region.

We found that the COMb distribution was the best fit for most of the samples regardless of bin width or region. The bin width had an effect on the number of samples for which the COMb distribution was the best fit. The results are summarised in table 3.3. For a bin width of 1ms, the COMb distribution was the best fit for over 90% of samples, the beta-binomial distribution was the best fit for less than 10% of samples, and the binomial distribution was the best fit for less than 1% of samples, across regions. For 5ms bins, the COMb distribution was the best fit for 70 – 80% of samples, the beta-binomial distribution was the best fit for 20 – 30% of the samples, and again the binomial distribution was the best fit for less than 1% of samples, across regions. Finally, for 10ms bins, the COMb distribution was the best fit for 53 – 80% of samples, the beta-binomial distribution was the best fit for 20 – 47% of the samples, and the binomial distribution was the best fit for less than 0.1% of samples, across regions.

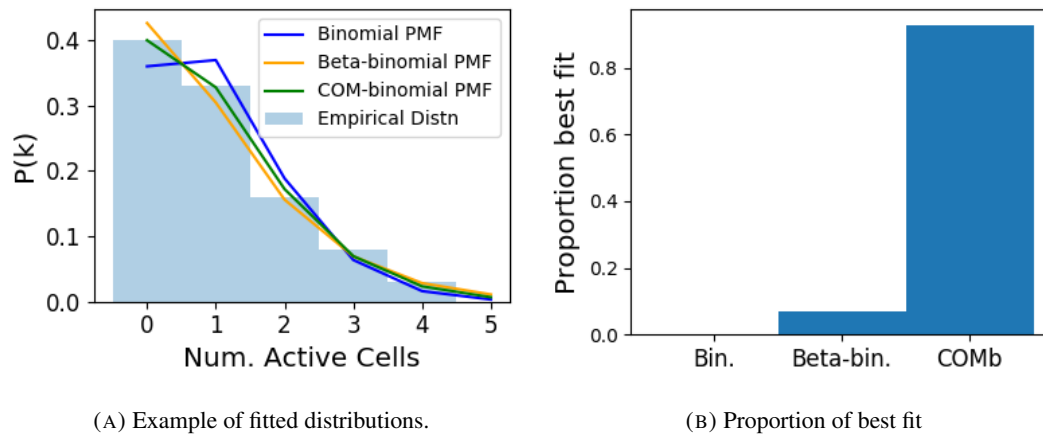


FIGURE 3.6: (A) An example of the binomial, beta-binomial, and Conway-Maxwell-binomial distributions fitted to a sample of neural activity. The Conway-Maxwell-binomial distribution is the best fit in this case. The histogram shows the empirical distribution of the sample. The probability mass function of each distribution is indicated by a different coloured line. (B) Across all samples in all trials, the proportion of samples for which each fitted distribution was the the best fit. The Conway-Maxwell-binomial distribution was the best fit for 93% of the samples taken from V1 using a bin width of 1ms.

Bin Width (ms)	Binomial	Beta-binomial	COMb
1ms	< 1%	< 10%	> 90%
5ms	< 0.1%	20 – 30%	70 – 80%
10ms	< 0.1%	20 – 47%	53 – 80%

TABLE 3.3: Proportion of samples for which each distribution was the best fit, grouped by bin width. The COMb distribution is the best fit most of the time.

3.4.3 Conway-Maxwell-binomial distribution captures changes in association at stimulus onset

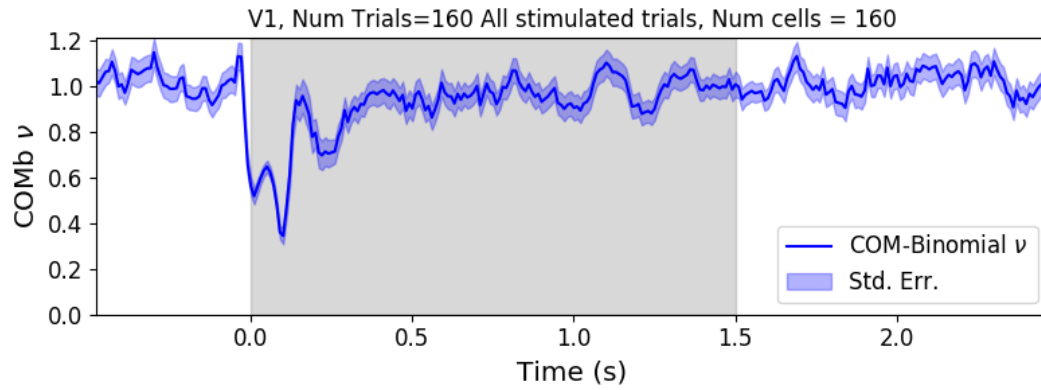
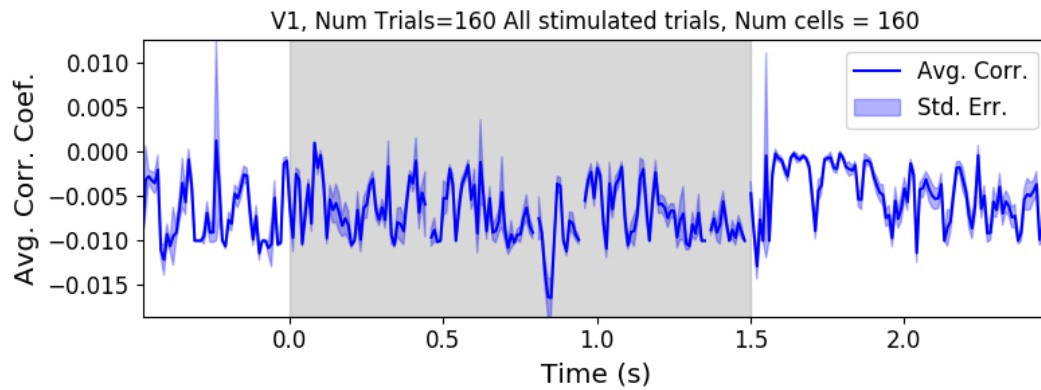
We fit a Conway-Maxwell-binomial (COMb) distribution to the number of active neurons in the 1ms time bins in a 100ms sliding window. We also measured the correlation coefficient between the spike counts of all possible pairs of neurons, and took the average of these coefficients. We did this for all the trials with a visual stimulus. We observed a reduction in the COMb distribution's ν parameter at stimulus onset from around 1 to between 0 and 1 (see figure 3.7a). A value of ν less than 1 indicates positive association between the neurons (see section 3.3.5). We might expect to see this positive association reflected in the correlation coefficients, but this is not the case. We see no change in the time series of average correlation measures at stimulus onset.

This may be due to the very short time bin we used in this case. We know that using small time bins can artificially reduce correlation measurements (**cohen**). In this case, fitting the COMb distribution may be a useful way to measure association in a neuronal ensemble over very short timescales ($< 10\text{ms}$).

3.4.4 Replicating stimulus related quenching of neural variability

Churchland et al. (2010) inspected the effect of a stimulus on neural variability. One of the measures of neural variability that they employed was the Fano factor of the spike counts of individual cells (see section 3.3.4). They found a reduction in neural variability as measured by the Fano factor in various cortical areas in a macaque at the onset of various visual stimuli, or a juice reward (Churchland et al., 2010).

We measured the Fano factor of the spike count of each cell in each brain region, during each trial. We measured the mean and standard error of these Fano factors from 500ms before stimulus onset until 1000ms after stimulus end. For the primary visual cortex, we found a transient reduction in the Fano factor immediately after stimulus onset. We used a Mann-Whitney U test to check that the Fano factors measured in a window starting at

(A) COMb ν parameter.

(B) Average correlation coefficient.

FIGURE 3.7: (A) We fit a Conway-Maxwell-binomial distribution to the number of active neurons in 1ms time bins of a 100ms sliding window. We did this for all trials with a visual stimulus and took the average across those trials. We see a transient drop in value for the distribution's ν parameter at stimulus onset. This shows an increase in association between the neurons. (B) We measured the correlation coefficient between the spike counts of all possible pairs of neurons in the same sliding window. We took the average of those coefficients. We also did this for every visually stimulated trial, and took the average across trials. The increase in association is not reflected with an increase in average correlation.

stimulus onset and ending 100ms later were significantly lower than the factors measured in a window ending at stimulus onset ($p < 0.001$, see figure 3.8a). We did not get this statistically significant result in any other region.

Our findings agree with those of Churchland et al. for the primary visual cortex. However Churchland also found a reduction in the Fano factor in the dorsal premotor cortex (PMd) at stimulus onset. Our measurements from the mouse motor cortex show no change at stimulus onset (see figure 3.8b). This could indicate some difference in the functionality of the motor cortex in a macaque and the motor cortex of a mouse.

Similar to these findings in the Fano factor, we found a reduction in the ν parameter of the COMB distribution on stimulus onset in V1 (figure 3.7a) and in no other region from

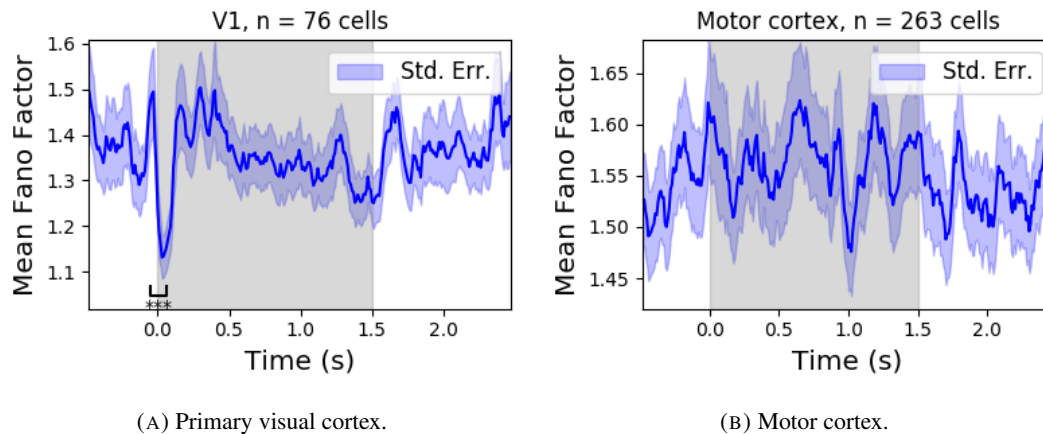


FIGURE 3.8: (A) The mean Fano factor of the spike counts of the cells in the primary visual cortex. Means were taken across cells first, then across trials. There was a significant decrease in the Fano factors immediately after stimulus onset. (B) The mean Fano factor of the spike counts of the cells in the motor cortex. No significant change in measurements at any point.

1917 which we had data. Specifically, the ν parameter reduced from around 1, to between 1 and 0.
 1918 This represents a change from no association between the neurons, to a positive association.
 1919 It is possible that this positive association may be responsible for the reduction in the Fano
 1920 factor.

1921 3.5 Discussion

1922 Our aim in this research was to develop a new statistical method for analysing the activity
 1923 of a neuronal ensemble at very short timescales. We wanted our method to use information
 1924 taken from the whole ensemble, but we also wanted the method to be quick and easy to
 1925 implement. It is likely that analysis methods with these characteristics will become valuable
 1926 as electrophysiological datasets include readings from more cells over longer time periods. In
 1927 this case, we used the number of active, or spiking, neurons in a very short time bin ($< 10\text{ms}$)
 1928 as a measure of ensemble activity.

1929 First of all, we showed that there were changes in response that we could model at these
 1930 very short time scales in some of the brain regions from which we had recordings. We ob-
 1931 served changes in the average number of active neurons, and the variance of the number of
 1932 active neurons in three different brain regions in response to visual stimuli. Since we know
 1933 that correlated behaviour is associated with sensory perception (deCharms and Merzenich,
 1934 1996), we might hope to measure the pairwise correlations within the neuronal population
 1935 in order to further investigate these responses. But, using such short time bins can produce
 1936 artificially small spike count correlation measurements (cohen). Overcoming this limitation

was one of our objectives for our new method. In order to do this, we abandoned the idea of measuring the correlations directly and embraced the concept of *association*. In order to quantify the association between neurons, we used the Conway-Maxwell-binomial distribution to model the number of active (spiking) neurons in an ensemble as a sum of possibly associated Bernoulli random variables.

We showed that the Conway-Maxwell-binomial distribution performed better than the more common options of the binomial and beta-binomial distributions. Furthermore, we showed that the positively associated behaviour between neurons in the primary visual cortex could be captured by fitting a Conway-Maxwell-binomial distribution, but was not captured by the more standard approach of measuring the spike count correlation. The associated behaviour could not be measured using spike count correlations, because of the very short bins required to capture short timescale behaviour.

We replicated a famous result from Churchland et al (2010) relating to the quenching of neural variability in cortical areas at stimulus onset, and in doing so, we established a correspondence between the association quantifying parameter of the Conway-Maxwell-binomial (COMb) distribution and the neural variability as measured by the Fano factor. We found a reduction in the ν parameter of the COMB distribution at stimulus onset, indicating a change from no association to positive association between neurons in V1. We found a corresponding reduction in the Fano factor of the individual cells in V1. The positive association between neurons induced by the stimulus would constrain the neurons to fire at the same time. The stimulus also induced a larger number of neurons to spike. These two actions combined could cause an increase in the firing rate of individual cells that is greater in magnitude than the increase in firing rate variability. If this is indeed the case, then the association as captured by the COMB distribution could be regarded as one of the ‘natural parameters’ of the ensemble response for short timescales. That is, a quantity that directly measures some aspect of the behaviour of the ensemble. In this case, it the correlated behaviour of the individual neurons is captured.

This work could be just a first step in creating analysis methods based on the Conway-Maxwell-binomial distribution, or similar statistical models. One way to extend the method would be to pair it up with the ‘Population Tracking model’ (O’Donnell et al., 2017). This model attempts to characterise the interaction between an ensemble and each member of the ensemble by quantifying the probability of spiking for a given a cell, given the number of active cells in the whole population. Combining this model with the COMB distribution would give us a model that could accurately fit the number of active neurons at any moment,

1971 and that gives a probability of firing for each cell, and therefore probabilities for full spiking
1972 patterns, without adding a huge number of parameters to fit.

1973 A more complex way to extend the model would be to fit a Conway-Maxwell-binomial
1974 distribution to data recorded from multiple brain regions simultaneously, with a different fit
1975 for each region, then to analyse the temporal relationship between the fitted parameters of
1976 each region. If we analysed the time series of the COMB distribution parameters from the
1977 different regions, looking at cross-correlations between regions, this may give some results
1978 relating to the timescales in which information is processed in different brain regions.

1979 **Chapter 4**

1980 **Studies with practical limitations &** 1981 **negative results**

UNIVERSITY OF BRISTOL

Abstract

Engineering

Department of Computer Science

Doctor of Philosophy

Investigating, implementing, and creating methods for analysing large neuronal ensembles

by Thomas J. DELANEY

Here I will present some details on research topics that I started, but that unfortunately did not lead anywhere useful. There are two pieces of research, based on two papers. Each paper is related to the overall theme of my PhD of analysing and modelling behaviours of populations of neurons. The first part is based on a model of parallel spike trains including higher order interactions by Shimazaki et al (2012). The second part is based on a multiscale model for making inferences on hierarchical data.

1996 **4.1 Dynamic state space model of pairwise and higher order neu-** 1997 **ronal correlations**

1998 In their paper Shimazaki et al (2012) aimed to model spike trains from populations of neurons
1999 in parallel, with pairwise and higher order dynamic interactions between the trains. They
2000 modelled the spike trains as multi-variate binary processes using a log-linear model, and they
2001 extracted spike interaction parameters using a Bayesian filter/EM-algorithm. They developed
2002 a goodness-of-fit measure for the model to test if including these higher order correlations
2003 is necessary for an accurate model. Their measure was based on the Bayes factor but they
2004 also assessed the suitability of higher order models using the AIC and BIC. So the increase
2005 in the number of parameters associated with fitting higher order interactions was taken into
2006 account. They tested the performance of the model on synthetic data with known higher
2007 order correlations. They used the model to look for higher order correlations in data from
2008 awake behaving animals. They use the model to demonstrate dynamic appearance of higher
2009 order correlations in the monkey motor cortexshimazaki.

2010 We used the available Python repository to implement the model, and we successfully
2011 worked through the tutorial provided. But we found that the model did not scale well to
2012 larger populations. We attempted to fit the model to a population of 10 neurons and found we
2013 didn't manage to finish the process. Since, our goal was to find a model to scale to hundreds
2014 or thousands of neurons, we decided that this model was no longer worth pursuing.

2015 **4.2 A multiscale model for hierarchical data applied to** 2016 **neuronal data**

2017 In their paper Kolacayk et al (2001) developed a framework for a modelling hierarchically
2018 aggregated data, and making inferences based on a model arising from this framework. They
2019 assumed that a hierarchical aggregation existed on the data in question, where each element at
2020 each level of the hierarchy had some associated measurements, an associated mean process,
2021 which was the expected value of these measurements. They also assumed that the measure-
2022 ments of each parent were equal to the sum of the measurements from all of its children.
2023 They showed that these assumptions gave rise to a relationship between parent and child
2024 measurements across all levels of the hierarchy, where the product of the likelihood of the
2025 parameters of the lowest level of the hierarchy can be expressed as products of conditional
2026 likelihoods of the elements of higher levels of the hierarchykolacayk.

They gave examples of these expressions for measurements sampled from Gaussian distributions, and Poisson distributions, and showed the definitions of the hierarchical parameters which reparametrise the distribution of these data taking the hierarchy into account. They go on to suggest prior distributions for this multiscale model, and integrate these priors to give posterior distributions for the measurements from each element at each level in the hierarchy, and expressions for the MAP estimated parameters of each the associated processes**kolacayk**.

We implemented their model in Python by creating some synthetic data from Poisson distributions, and defining a hierarchy by agglomerating these data. We calculated the MAP estimates using our knowledge of the hierarchy, and using the expressions given in the paper. We found that the MAP estimates were far less accurate than would be achieved by simply ignoring the hierarchy during estimation, and using a maximum likelihood approach. After that, we decided to move on.

Bibliography

- Allen, William E. et al. (2019). “Thirst regulates motivated behavior through modulation of brainwide neural population dynamics”. In: *Science* 364.6437. ISSN: 0036-8075. DOI: [10.1126/science.aav3932](https://doi.org/10.1126/science.aav3932). eprint: <https://science.sciencemag.org/content/364/6437/eaav3932.full.pdf>. URL: <https://science.sciencemag.org/content/364/6437/eaav3932>.
- Baadel, S., F. Thabtah, and J. Lu (2016). “Overlapping clustering: A review”. In: *2016 SAI Computing Conference (SAI)*, pp. 233–237. DOI: [10.1109/SAI.2016.7555988](https://doi.org/10.1109/SAI.2016.7555988).
- Baldassano, Christopher et al. (2017). “Discovering Event Structure in Continuous Narrative Perception and Memory”. In: *Neuron* 95.3, 709–721.e5. ISSN: 0896-6273. DOI: <https://doi.org/10.1016/j.neuron.2017.06.041>. URL: <http://www.sciencedirect.com/science/article/pii/S0896627317305937>.
- Bartol, Thomas M. et al. (2015). “Computational reconstitution of spine calcium transients from individual proteins”. In: *Frontiers in Synaptic Neuroscience* 7, p. 17. ISSN: 1663-3563. DOI: [10.3389/fnsyn.2015.00017](https://doi.org/10.3389/fnsyn.2015.00017). URL: <https://www.frontiersin.org/article/10.3389/fnsyn.2015.00017>.
- Berens, Philipp et al. (May 2018). “Community-based benchmarking improves spike rate inference from two-photon calcium imaging data”. In: *PLOS Computational Biology* 14.5, pp. 1–13. DOI: [10.1371/journal.pcbi.1006157](https://doi.org/10.1371/journal.pcbi.1006157). URL: <https://doi.org/10.1371/journal.pcbi.1006157>.
- Bezanson, Jeff et al. (Sept. 2012). “Julia: A Fast Dynamic Language for Technical Computing”. In: *MIT*.
- Chen, Tsai-Wen et al. (July 2013). “Ultrasensitive fluorescent proteins for imaging neuronal activity”. In: *Nature* 499, 295–300. DOI: [10.1038/nature12354](https://doi.org/10.1038/nature12354). URL: <https://doi.org/10.1038/nature12354>.
- Churchland, Mark M. et al. (2010). “Stimulus onset quenches neural variability: a widespread cortical phenomenon”. eng. In: *Nature neuroscience* 13.3. 20173745[pmid], pp. 369–378. ISSN: 1546-1726. DOI: [10.1038/nn.2501](https://doi.org/10.1038/nn.2501). URL: <https://pubmed.ncbi.nlm.nih.gov/20173745>.

- 2069 Cohen, Marlene R. and Adam Kohn (2011). “Measuring and interpreting neuronal correla-
2070 tions”. In: *Nature Neuroscience* 14.7, pp. 811–819. ISSN: 1546-1726. DOI: [10.1038/
2071 nn.2842](https://doi.org/10.1038/nn.2842). URL: <https://doi.org/10.1038/nn.2842>.
- 2072 Cohen, Marlene R. and John H. R. Maunsell (2009). “Attention improves performance pri-
2073 marily by reducing interneuronal correlations”. eng. In: *Nature neuroscience* 12.12. 19915566[pmid],
2074 pp. 1594–1600. ISSN: 1546-1726. DOI: [10.1038 / nn . 2439](https://pubmed.ncbi.nlm.nih.gov/19915566). URL: [https : / /
2075 pubmed.ncbi.nlm.nih.gov/19915566](https://pubmed.ncbi.nlm.nih.gov/19915566).
- 2076 deCharms, R. Christopher and Michael M. Merzenich (1996). “Primary cortical represen-
2077 tation of sounds by the coordination of action-potential timing”. In: *Nature* 381.6583,
2078 pp. 610–613. ISSN: 1476-4687. DOI: [10.1038/381610a0](https://doi.org/10.1038/381610a0). URL: [https://doi.
2079 org/10.1038/381610a0](https://doi.org/10.1038/381610a0).
- 2080 Deneux, Thomas et al. (July 2016). “Accurate spike estimation from noisy calcium signals
2081 for ultrafast three-dimensional imaging of large neuronal populations in vivo”. In: *Nature*
2082 *Communications* 7.1. DOI: [10.1038/ncomms12190](https://doi.org/10.1038/ncomms12190). URL: [https://doi.org/
2083 10.1038/ncomms12190](https://doi.org/10.1038/ncomms12190).
- 2084 Faas, G. C. et al. (Mar. 2011). “Calmodulin as a direct detector of Ca²⁺ signals”. In: *Nature*
2085 *neuroscience* 14.3, pp. 301–304. DOI: [10.1038 / nn . 2746](https://doi.org/10.1038/nn.2746). URL: [https : / / dx .
2086 doi.org/10.1038/nn.2746](https://doi.org/10.1038/nn.2746).
- 2087 Fiala, John C. and Kristen M. Harris (1999). *Dendrite Structure*.
- 2088 Flach, Boris (Sept. 2013). “A Class of Random Fields on Complete Graphs with Tractable
2089 Partition Function”. In: *IEEE transactions on pattern analysis and machine intelligence*
2090 35, pp. 2304–6. DOI: [10.1109/TPAMI.2013.99](https://doi.org/10.1109/TPAMI.2013.99).
- 2091 Fosdick, Bailey et al. (Aug. 2016). “Configuring Random Graph Models with Fixed Degree
2092 Sequences”. In: *SIAM Review* 60. DOI: [10.1137/16M1087175](https://doi.org/10.1137/16M1087175).
- 2093 Friedrich, Johannes and Liam Paninski (2016). “Fast Active Set Methods for Online Spike
2094 Inference from Calcium Imaging”. In: *Advances in Neural Information Processing Sys-*
2095 *tems* 29. Ed. by D. D. Lee et al. Curran Associates, Inc., pp. 1984–1992. URL: [http :
2096 //papers.nips.cc/paper/6505-fast-active-set-methods-for-
2097 online-spike-inference-from-calcium-imaging.pdf](http://papers.nips.cc/paper/6505-fast-active-set-methods-for-online-spike-inference-from-calcium-imaging.pdf).
- 2098 Ganmor, Elad, Ronen Segev, and Elad Schneidman (2011). “Sparse low-order interaction
2099 network underlies a highly correlated and learnable neural population code”. In: *Proceed-*
2100 *ings of the National Academy of Sciences* 108.23, pp. 9679–9684. ISSN: 0027-8424. DOI:
2101 [10.1073/pnas.1019641108](https://doi.org/10.1073/pnas.1019641108). eprint: <https://www.pnas.org/content/>

- 2102 108/23/9679.full.pdf. URL: [https://www.pnas.org/content/108/](https://www.pnas.org/content/108/23/9679)
2103 [23/9679](https://www.pnas.org/content/108/23/9679).
- 2104 Girard, P., J. M. Hupé, and J. Bullier (2001). “Feedforward and Feedback Connections Be-
2105 tween Areas V1 and V2 of the Monkey Have Similar Rapid Conduction Velocities”. In:
2106 *Journal of Neurophysiology* 85.3. PMID: 11248002, pp. 1328–1331. DOI: [10.1152/](https://doi.org/10.1152/jn.2001.85.3.1328)
2107 [jn.2001.85.3.1328](https://doi.org/10.1152/jn.2001.85.3.1328). eprint: [https://doi.org/10.1152/jn.2001.85.](https://doi.org/10.1152/jn.2001.85.3.1328)
2108 [3.1328](https://doi.org/10.1152/jn.2001.85.3.1328). URL: <https://doi.org/10.1152/jn.2001.85.3.1328>.
- 2109 Greenberg, David et al. (Nov. 2018). “Accurate action potential inference from a calcium
2110 sensor protein through biophysical modeling.” in: DOI: [10.1101/479055](https://doi.org/10.1101/479055).
- 2111 Gründemann, Jan et al. (2019). “Amygdala ensembles encode behavioral states”. In: *Science*
2112 364.6437. ISSN: 0036-8075. DOI: [10.1126/science.aav8736](https://doi.org/10.1126/science.aav8736). eprint: [https:](https://science.sciencemag.org/content/364/6437/eaav8736.full.pdf)
2113 [//science.sciencemag.org/content/364/6437/eaav8736.full.](https://science.sciencemag.org/content/364/6437/eaav8736.full.pdf)
2114 [pdf](https://science.sciencemag.org/content/364/6437/eaav8736.full.pdf). URL: [https://science.sciencemag.org/content/364/6437/](https://science.sciencemag.org/content/364/6437/eaav8736)
2115 [eaav8736](https://science.sciencemag.org/content/364/6437/eaav8736).
- 2116 Humphries, Mark et al. (Jan. 2019). “Spectral rejection for testing hypotheses of structure in
2117 networks”. In:
- 2118 Humphries, Mark D. (2011). “Spike-Train Communities: Finding Groups of Similar Spike
2119 Trains”. In: *Journal of Neuroscience* 31.6, pp. 2321–2336. ISSN: 0270-6474. DOI: [10.](https://doi.org/10.1523/JNEUROSCI.2853-10.2011)
2120 [1523/JNEUROSCI.2853-10.2011](https://doi.org/10.1523/JNEUROSCI.2853-10.2011). eprint: [https://www.jneurosci.org/](https://www.jneurosci.org/content/31/6/2321.full.pdf)
2121 [content/31/6/2321.full.pdf](https://www.jneurosci.org/content/31/6/2321.full.pdf). URL: [https://www.jneurosci.org/](https://www.jneurosci.org/content/31/6/2321)
2122 [content/31/6/2321](https://www.jneurosci.org/content/31/6/2321).
- 2123 Jun, James J. et al. (2017). “Fully integrated silicon probes for high-density recording of
2124 neural activity”. In: *Nature* 551.7679, pp. 232–236. ISSN: 1476-4687. DOI: [10.1038/](https://doi.org/10.1038/nature24636)
2125 [nature24636](https://doi.org/10.1038/nature24636). URL: <https://doi.org/10.1038/nature24636>.
- 2126 Kilhoffer, Marie-Claude et al. (Sept. 1992). “Use of Engineered Proteins With Internal Tryptophan
2127 Reporter Groups and Perturbation Techniques to Probe the Mechanism of Ligand-
2128 Protein Interactions: Investigation of the Mechanism of Calcium Binding to Calmod-
2129 ulin”. In: *Biochemistry* 31.34, pp. 8098–8106. DOI: [10.1021/bi00149a046](https://doi.org/10.1021/bi00149a046). URL:
2130 <https://doi.org/10.1021/bi00149a046>.
- 2131 Koch, Christoff (1999). *Biophysics of Computation: Information Processing in Single Neu-*
2132 *rons*. Oxford University Press. ISBN: ISBN 0-19-510491-9.
- 2133 Lee, Suk-HO et al. (July 2000). “Differences in Ca²⁺ buffering properties between excitatory
2134 and inhibitory hippocampal neurons from the rat”. In: *The Journal of Physiology* 525.
2135 DOI: [10.1111/j.1469-7793.2000.t01-3-00405.x](https://doi.org/10.1111/j.1469-7793.2000.t01-3-00405.x).

- 2136 Litwin-Kumar, Ashok, Maurice Chacron, and Brent Doiron (Sept. 2012). “The Spatial Struc-
2137 ture of Stimuli Shapes the Timescale of Correlations in Population Spiking Activity”.
2138 In: *PLoS computational biology* 8, e1002667. DOI: [10.1371/journal.pcbi.](https://doi.org/10.1371/journal.pcbi.1002667)
2139 [1002667](https://doi.org/10.1371/journal.pcbi.1002667).
- 2140 Maravall, M et al. (May 2000). “Estimating intracellular calcium concentrations and buffer-
2141 ing without wavelength ratioing”. In: *Biophysical Journal* 78.5, pp. 2655–2667. DOI:
2142 [10.1016/S0006-3495\(00\)76809-3](https://doi.org/10.1016/S0006-3495(00)76809-3). URL: [https://doi.org/10.1016/](https://doi.org/10.1016/S0006-3495(00)76809-3)
2143 [s0006-3495\(00\)76809-3](https://doi.org/10.1016/S0006-3495(00)76809-3).
- 2144 Maugis, Pa (Jan. 2014). “Event Conditional Correlation: Or How Non-Linear Linear Depen-
2145 dence Can Be”. In:
- 2146 Meilă, Marina (2007). “Comparing clusterings—an information based distance”. In: *Journal*
2147 *of Multivariate Analysis* 98.5, pp. 873 –895. ISSN: 0047-259X. DOI: [https://doi.](https://doi.org/10.1016/j.jmva.2006.11.013)
2148 [org/10.1016/j.jmva.2006.11.013](https://doi.org/10.1016/j.jmva.2006.11.013). URL: [http://www.sciencedirect.](http://www.sciencedirect.com/science/article/pii/S0047259X06002016)
2149 [com/science/article/pii/S0047259X06002016](http://www.sciencedirect.com/science/article/pii/S0047259X06002016).
- 2150 Murray, John D. et al. (2014). “A hierarchy of intrinsic timescales across primate cortex”.
2151 In: *Nature Neuroscience* 17.12, pp. 1661–1663. ISSN: 1546-1726. DOI: [10.1038/nn.](https://doi.org/10.1038/nn.3862)
2152 [3862](https://doi.org/10.1038/nn.3862). URL: <https://doi.org/10.1038/nn.3862>.
- 2153 Neher, E. and G. J. Augustine (1992). “Calcium gradients and buffers in bovine chromaffin
2154 cells”. eng. In: *The Journal of physiology* 450. 1331424[pmid], pp. 273–301. ISSN: 0022-
2155 3751. DOI: [10.1113/jphysiol.1992.sp019127](https://doi.org/10.1113/jphysiol.1992.sp019127). URL: [https://pubmed.](https://pubmed.ncbi.nlm.nih.gov/1331424)
2156 [ncbi.nlm.nih.gov/1331424](https://pubmed.ncbi.nlm.nih.gov/1331424).
- 2157 O’Donnell, Cian et al. (Jan. 2017). “The population tracking model: a simple, scalable statis-
2158 tical model for neural population data”. English. In: *Neural Computation* 29.1, pp. 50–
2159 93. ISSN: 0899-7667. DOI: [10.1162/NECO_a_00910](https://doi.org/10.1162/NECO_a_00910).
- 2160 Patterson, Carlyn A. et al. (2014). “Similar adaptation effects in primary visual cortex and
2161 area MT of the macaque monkey under matched stimulus conditions”. In: *Journal of Neu-*
2162 *rophysiology* 111.6. PMID: 24371295, pp. 1203–1213. DOI: [10.1152/jn.00030.](https://doi.org/10.1152/jn.00030.2013)
2163 [2013](https://doi.org/10.1152/jn.00030.2013). eprint: <https://doi.org/10.1152/jn.00030.2013>. URL: [https:](https://doi.org/10.1152/jn.00030.2013)
2164 [//doi.org/10.1152/jn.00030.2013](https://doi.org/10.1152/jn.00030.2013).
- 2165 Pnevmatikakis, E.A. et al. (Jan. 2016). “Simultaneous Denoising, Deconvolution, and Demix-
2166 ing of Calcium Imaging Data”. In: *Neuron* 89.2, pp. 285–299. DOI: [10.1016/j.](https://doi.org/10.1016/j.neuron.2015.11.037)
2167 [neuron.2015.11.037](https://doi.org/10.1016/j.neuron.2015.11.037). URL: [https://doi.org/10.1016/j.neuron.](https://doi.org/10.1016/j.neuron.2015.11.037)
2168 [2015.11.037](https://doi.org/10.1016/j.neuron.2015.11.037).

- 2169 Pnevmatikakis, Eftychios et al. (Nov. 2013). “Bayesian spike inference from calcium imaging
2170 data”. In: *Conference Record - Asilomar Conference on Signals, Systems and Computers*.
2171 DOI: [10.1109/ACSSC.2013.6810293](https://doi.org/10.1109/ACSSC.2013.6810293).
- 2172 Pnevmatikakis, Eftychios et al. (Sept. 2014). “A structured matrix factorization framework
2173 for large scale calcium imaging data analysis”. In:
2174 Schneidman, Elad et al. (2006). “Weak pairwise correlations imply strongly correlated net-
2175 work states in a neural population”. eng. In: *Nature* 440.7087. 16625187[pmid], pp. 1007–
2176 1012. ISSN: 1476-4687. DOI: [10.1038/nature04701](https://doi.org/10.1038/nature04701). URL: [https://pubmed.
2177 ncbi.nlm.nih.gov/16625187](https://pubmed.ncbi.nlm.nih.gov/16625187).
- 2178 Shannon, C. E. (1948). “A Mathematical Theory of Communication”. In: *Bell System Techni-
2179 cal Journal* 27.3, pp. 379–423. DOI: [10.1002/j.1538-7305.1948.tb01338.x](https://doi.org/10.1002/j.1538-7305.1948.tb01338.x).
2180 eprint: [https://onlinelibrary.wiley.com/doi/pdf/10.1002/j.
2181 1538-7305.1948.tb01338.x](https://onlinelibrary.wiley.com/doi/pdf/10.1002/j.1538-7305.1948.tb01338.x). URL: [https://onlinelibrary.wiley.
2182 com/doi/abs/10.1002/j.1538-7305.1948.tb01338.x](https://onlinelibrary.wiley.com/doi/abs/10.1002/j.1538-7305.1948.tb01338.x).
- 2183 Steinmetz, Nick, Matteo Carandini, and Kenneth D. Harris (2019). “*Single Phase3*” and
2184 “*Dual Phase3*” *Neuropixels Datasets*. DOI: [10.6084/m9.figshare.7666892.
2185 v2](https://doi.org/10.6084/m9.figshare.7666892.v2). URL: [https://figshare.com/articles/dataset/_Single_Phase3_
2186 Neuropixels_Dataset/7666892/2](https://figshare.com/articles/dataset/_Single_Phase3_Neuropixels_Dataset/7666892/2).
- 2187 Stringer, Carsen et al. (2019). “Spontaneous behaviors drive multidimensional, brainwide ac-
2188 tivity”. In: *Science* 364.6437. ISSN: 0036-8075. DOI: [10.1126/science.aav7893](https://doi.org/10.1126/science.aav7893).
2189 eprint: [https://science.sciencemag.org/content/364/6437/eaav7893.
2190 full.pdf](https://science.sciencemag.org/content/364/6437/eaav7893.full.pdf). URL: [https://science.sciencemag.org/content/364/
2191 6437/eaav7893](https://science.sciencemag.org/content/364/6437/eaav7893).
- 2192 Tada, Mayumi et al. (2014). “A highly sensitive fluorescent indicator dye for calcium imag-
2193 ing of neural activity in vitro and in vivo”. In: *European Journal of Neuroscience* 39.11,
2194 pp. 1720–1728. DOI: [10.1111/ejn.12476](https://doi.org/10.1111/ejn.12476). eprint: [https://onlinelibrary.
2195 wiley.com/doi/pdf/10.1111/ejn.12476](https://onlinelibrary.wiley.com/doi/pdf/10.1111/ejn.12476). URL: [https://onlinelibrary.
2196 wiley.com/doi/abs/10.1111/ejn.12476](https://onlinelibrary.wiley.com/doi/abs/10.1111/ejn.12476).
- 2197 Tian, Lin et al. (2009). “Imaging neural activity in worms, flies and mice with improved
2198 GCaMP calcium indicators”. eng. In: *Nature methods* 6.12. 19898485[pmid], pp. 875–
2199 881. ISSN: 1548-7105. DOI: [10.1038/nmeth.1398](https://doi.org/10.1038/nmeth.1398). URL: [https://pubmed.
2200 ncbi.nlm.nih.gov/19898485](https://pubmed.ncbi.nlm.nih.gov/19898485).
- 2201 Tkačik, Gašper et al. (2014). “Searching for collective behavior in a large network of sen-
2202 sory neurons”. eng. In: *PLoS computational biology* 10.1. 24391485[pmid], e1003408–

- 2203 e1003408. ISSN: 1553-7358. DOI: 10.1371/journal.pcbi.1003408. URL:
2204 <https://pubmed.ncbi.nlm.nih.gov/24391485>.
- 2205 Treves, Alessandro and Stefano Panzeri (1995). "The Upward Bias in Measures of Informa-
2206 tion Derived from Limited Data Samples". In: *Neural Computation* 7.2, pp. 399–407.
2207 DOI: 10.1162/neco.1995.7.2.399. eprint: [https://doi.org/10.1162/](https://doi.org/10.1162/neco.1995.7.2.399)
2208 [neco.1995.7.2.399](https://doi.org/10.1162/neco.1995.7.2.399). URL: [https://doi.org/10.1162/](https://doi.org/10.1162/neco.1995.7.2.399)
2209 [neco.1995.7.2.399](https://doi.org/10.1162/neco.1995.7.2.399).
- 2210 Vinh, Nguyen Xuan, Julien Epps, and James Bailey (Dec. 2010). "Information Theoretic
2211 Measures for Clusterings Comparison: Variants, Properties, Normalization and Correc-
2212 tion for Chance". In: *J. Mach. Learn. Res.* 11, 2837–2854. ISSN: 1532-4435.
- 2213 Vogelstein, Joshua T. et al. (Oct. 2010). "Fast nonnegative deconvolution for spike train infer-
2214 ence from population calcium imaging". In: *Journal of neurophysiology* 104.6, 295–300.
2215 DOI: 10.1152/jn.01073.2009. URL: [https://dx.doi.org/10.1152/](https://dx.doi.org/10.1152/jn.01073.2009)
2216 [2Fjn.01073.2009](https://dx.doi.org/10.1152/jn.01073.2009).
- 2217 Wierzynski, "Casimir M. et al. ("2009"). ""State-Dependent Spike-Timing Relationships be-
2218 tween Hippocampal and Prefrontal Circuits during Sleep"". In: "Neuron" "61"."4", "587
2219 –596". ISSN: "0896-6273". DOI: "[https://doi.org/10.1016/j.neuron.](https://doi.org/10.1016/j.neuron.2009.01.011)
2220 [2009.01.011](https://doi.org/10.1016/j.neuron.2009.01.011)". URL: "[http://www.sciencedirect.com/science/](http://www.sciencedirect.com/science/article/pii/S0896627309000786)
2221 [article/pii/S0896627309000786](http://www.sciencedirect.com/science/article/pii/S0896627309000786)".
- 2222 Zou, Hui and Trevor Hastie (2005). "Regularization and variable selection via the Elastic
2223 Net". In: *Journal of the Royal Statistical Society, Series B* 67, pp. 301–320.